Functional Magnetic Resonance Imaging of Cerebral Blood Volume

Bojana Stefanovic, B.A.Sc.

Department of Biomedical Engineering

McGill University, Montreal, Canada

November 1, 2004

A thesis submitted to McGill University in partial fulfillment of the requirements for the degree of Doctor of Philosophy

©Bojana Stefanovic, 2004

Library and Archives Canada

Published Heritage Branch

395 Wellington Street
Ottawa ON K1A 0N4
Canada

Bibliothèque et Archives Canada

Direction du Patrimoine de l'édition

395, rue Wellington
Ottawa ON K1A 0N4
Canada

Your file Votre référence
ISBN: 0-494-12948-4
Our file Notre référence
ISBN: 0-494-12948-4

NOTICE:
The author has granted a non-exclusive license allowing Library and Archives Canada to reproduce, publish, archive, preserve, conserve, communicate to the public by telecommunication or on the Internet, loan, distribute and sell theses worldwide, for commercial or non-commercial purposes, in microform, paper, electronic and/or any other formats.

The author retains copyright ownership and moral rights in this thesis. Neither the thesis nor substantial extracts from it may be printed or otherwise reproduced without the author's permission.

AVIS:
L'auteur a accordé une licence non exclusive permettant à la Bibliothèque et Archives Canada de reproduire, publier, archiver, sauvegarder, conserver, transmettre au public par télécommunication ou par l'Internet, prêter, distribuer et vendre des thèses partout dans le monde, à des fins commerciales ou autres, sur support microforme, papier, électronique et/ou autres formats.

L'auteur conserve la propriété du droit d'auteur et des droits moraux qui protège cette thèse. Ni la thèse ni des extraits substantiels de celle-ci ne doivent être imprimés ou autrement reproduits sans son autorisation.

In compliance with the Canadian Privacy Act some supporting forms may have been removed from this thesis.

While these forms may be included in the document page count, their removal does not represent any loss of content from the thesis.

Conformément à la loi canadienne sur la protection de la vie privée, quelques formulaires secondaires ont été enlevés de cette thèse.

Bien que ces formulaires aient inclus dans la pagination, il n'y aura aucun contenu manquant.

Canada

Contents

List of Figures

List of Tables

Acknowledgments

For his unwearying guidance, encouragement and faith that not only made this project possible but also transformed it into a delightful and stimulating endeavor, I thank my supervisor, Dr. G. Bruce Pike.

I would like to express my gratitude to many students, staff and faculty at the BIC and elsewhere who have helped me throughout this project: Irina Kezele, Alexandre Bastos, Jennifer Campbell, Leili Torab, Michael Ferreira, Jeff Atkinson, Louis Collins, Christian Sirard, Ives Levesque, Simon Francis, Aki Caramanos, Andrew Janke, Noor Kabani, Valentina Petre, Carmela Tartaglia, Mark Griffin, Peter Petric, Najma Khalili, Marguerite Wieckowska, Karma Advani and Charmaine Chia. I would especially like to thank Jan Warnking, John Sled and Rick Hoge for their invaluable input, shared inspiration and mentorship. I am indebted to Andre Cormier for resolving countless last-minute hurdles and technical difficulties, building an impeccable wooden construction for blood circulation gear (that will surely outlive the scanner!), imbuing the daily MRI scanning routine with incredible efficiency, and, most of all, making our work at the scanner a sheer pleasure.

There would be no data and hence no findings in this work were it not for numerous volunteers who have participated in these studies (some on many an occasion), often requiring herculean efforts just to maintain alertness. For their indispensable help with administrative and logistical matters, I am very grateful to Jennifer Chew, Helene Day and Pina Sorrini. I also thank Jean-Francois Malouin and Peter Neelin for their help with network support issues, the respiratory therapy staff for assistance with setting up and running the physiological monitoring system, as well as the staff at the MNI blood laboratory and the

Royal Victoria Hospital blood gas laboratory for help with blood collection and specimen analysis. I thank Dr. Ralf Loeffler of Siemens Medical, Inc. for shedding light on many idiosyncrasies of the IDEA programming environment. Finally, financial support provided by the Natural Sciences and Engineering Research Council of Canada as well as the Canadian Institutes of Health Research is gratefully acknowledged.

Contributions of Authors

I am the first author of all four manuscripts included in this thesis and have performed over 90% of the work described. The tasks included the introduction of the novel theoretical concepts, the development, implementation and validation of the new fMRI sequence, design of the experimental protocols, data collection and analysis as well as the writing of all papers.

The following list summarizes the contribution of the co-authors:

1. **John G. Sled, Ph.D.** Help with sequence development and data analysis of the manuscript contained in Chapter 3.

2. **Jan M. Warnking, Ph.D.** Work on the development of experimental protocol, sequence development and data analysis of the paper included in Chapter 6.

3. **G. Bruce Pike, Ph.D.** Overall supervision of this Ph.D. project.

Other Publications

The following are additional peer-reviewed conference abstracts which arose from the work described in this thesis:

1. Stefanovic B and Pike GB. Quantitative Dynamic Measurement of Cerebral Blood Volume Changes via fMRI. Proceedings of the 10th International Society for Magnetic Resonance in Medicine (ISMRM) Scientific Meeting and Exhibition, Honolulu, Hawai.i, May 18-24, 2002.

2. Stefanovic B, Sled JG and Pike GB. Refocusing Rate Independence of T2 in Grey and White Matter of the Occipital Lobe. Proceedings of the 10th International Society for Magnetic Resonance in Medicine (ISMRM) Scientific Meeting and Exhibition, Honolulu, Hawai'i, May 18-24, 2002.

3. Stefanovic B and Pike GB. fMRI-based Quantification of Cerebral Blood Volume Changes. NeuroImage 19(2):311 S1, 2003.

4. Stefanovic B, Warnking JM and Pike GB. Simultaneous fMRI-based Measurements of Cerebral Blood Volume, Flow and BOLD. NeuroImage 19(2):312 S1, 2003.

5. Stefanovic B, Warnking JM and Pike GB. Neuronal Inhibition Induces Downregulation of Flow and Metabolism. Proceedings of the 12th International Society for Magnetic Resonance in Medicine (ISMRM) Scientific Meeting and Exhibition, Kyoto, Japan, May 15-21, 2004.

6. Stefanovic B and Pike GB. Quantifying the Intravascular SE BOLD Effect at 1.5T. Proceedings of the 12th International Society for Magnetic Resonance in Medicine (ISMRM) Scientific Meeting and Exhibition, Kyoto, Japan, May 15-21, 2004.

7. Stefanovic B, Warnking JM and Pike GB. Perfusion and Oxygen Consumption Changes with Neuronal Inhibition. NeuroImage 22: TU 155 S1, 2004.

8. Stefanovic B and Pike GB. Quantifying the Intravascular SE BOLD Effect at 1.5 T. NeuroImage 22:3WE 10 S1, 2004.

9. Stefanovic B and Pike GB. Spin-spin Relaxometry of Blood at 1.5 T. NeuroImage 22: WE 309 S1, 2004.

List of Abbreviations

ADP :	adenosine diphosphate, a lower-energy form of ATP
AMP :	adenosine monophosphate
AMPA :	amino-3-hydroxy-5-methyl-4-isoxazole propionate
ATP :	adenosine triphosphate, the energy carrier of living organisms
ASL :	arterial spin labeling
BMS :	bulk magnetic susceptibility
BOLD :	blood oxygenation level dependent
ceMRI:	contrast enhanced MRI
CBF :	cerebral blood flow
CBV :	cerebral blood volume
CBV_v:	venous cerebral blood volume
CMR_{glu}:	cerebral metabolic rate of glucose
CMR_{O_2}:	cerebral metabolic rate of oxygen
CSF :	cerebrospinal fluid
CPMG :	Carr-Purcell-Meiboom-Gill
CPP :	cerebral perfusion pressure
dHb :	deoxyhemoglobin
D :	diffusion coefficient
DCT :	dynamic computed tomography
DOT :	diffuse optical tomography
DSC :	dynamic susceptibility contrast
EPI :	echo planar imaging
EV :	extravascular
$FADH_2$:	the reduced form of flavin adenine dinucleotide
FAIR :	flow alternating inversion recovery
fMRI :	functional magnetic resonance imaging
FWHM :	full width at half maximum
Gd-DTPA:	gadolinium diethylaminetriaminopentaacetic acid
GM :	grey matter

Hb/dHb/oHb :	hemoglobin / deoxyhemoglobin / oxyhemoglobin
Hct :	hematocrit
IV :	intravascular
NAD^+ :	nicotinamide adenine dinucleotide
NADH :	the reduced form of NAD^+
NIRS :	near infrared spectroscopy
NO :	nitric oxide
nNOS :	neuronal nitric oxide synthase
NMDA :	N-methyl-D-aspartate
M1 :	primary motor cortex
MION:	monocrystalline iron oxide nanocolloid
MNI :	Montreal Neurological Institute
MR/MRI :	magnetic resonance / magnetic resonance imaging
MVC :	maximum voluntary contraction
NMR :	nuclear magnetic resonance
NME :	normalized mean squared error
OEF :	oxygen extraction fraction
PASL:	pulsed arterial spin labeling
PICORE :	proximal inversion with a control for off-resonance effects
PET :	positron emission tomography
R_2^*:	transverse relaxation rate constant ($1/T_2^*$)
RBC :	red blood cell
RF :	radio frequency
ROI :	region of interest
SE :	spin echo
SNR :	signal to noise ratio
SPECT :	single photon emission computed tomography
SSR :	sum of squared residuals
T :	Tesla
T_1 :	spin-lattice relaxation time constant
T_2:	intrinsic spin-spin relaxation time constant
T_2^*:	transverse relaxation time constant ($1/R_2^*$)
TE :	echo time
TI :	inversion time
TMS :	transcranial magnetic stimulation
TR :	repetition time
VC :	visual cortex
VERVE:	venous refocusing for volume estimation
Y :	blood oxygen saturation
WM:	white matter
$\%\Delta$:	percent signal change

Abstract

This dissertation describes a novel method for quantifying venous cerebral blood volume (CBV_v) changes accompanying normal functional activation and employs quantitative functional magnetic resonance imaging (fMRI) methods to study the hemodynamic and metabolic changes accompanying neuronal inhibition. An in vivo occipital lobe relaxometry study was performed first to investigate the dependence of the spin-spin relaxation time constant of tissue, $T_{2_{tissue}}$, on the refocusing interval over the range of interest and thus test the basis of the proposed CBV_v method. The small decrease of the apparent $T_{2_{tissue}}$ with refocusing interval elongation is consistent with blood being the only significant source of refocusing interval dependence of apparent T_2 in grey and white matter of the occipital lobe. In ensuing in vitro blood relaxometry studies, ensemble fitting of the entire set of $T_{2_{blood}}$ estimates, obtained over an extensive range of blood oxygenation levels and refocusing intervals, was performed using both the fast chemical exchange model and the model of diffusion in weak magnetic field inhomogeneities. The results support the application of a diffusion model in describing the deoxyhemoglobin-induced enhancement in blood transverse relaxation rate at 1.5 T. Given the uniqueness of $T_{2_{blood}}$ dependence on the refocusing rates over the range of interest, the novel CBV_v method - venous refocusing for volume estimation (VERVE) - successfully isolates the blood signal by refocusing rate variation. A model of functional brain activation was developed and in vitro blood relaxometry data used to assess the effect of the intravascular spin-echo blood oxygenation level dependent (BOLD) contrast on the activation-induced VERVE signal change, allowing robust estimation of venous CBV changes. The method was demonstrated in a visual

stimulation study of healthy young adults, where an average venous blood volume in the visual cortex increase was estimated at 16±2%. This method provides efficient and continuous monitoring of venous cerebral blood volume, thereby enabling further exploration of the mechanism underlying BOLD fMRI response to physiological, patho-physiological and pharmacological perturbations. Finally, oxygen consumption (CMR_{O_2}) and cerebral blood flow (CBF) changes following neuronal deactivation were examined. The percent changes in CMR_{O_2} and CBF were linearly related, with a slope of 0.44±0.04. The coupling ratio thus established for both positive and negative CMR_{O_2} and CBF changes is in close agreement with the ones observed by earlier studies investigating M1 perfusion and oxygen consumption increases. These findings characterize the hemodynamic and metabolic downregulation accompanying focal neuronal deactivation and thereby establish the sustained negative BOLD response as a marker of net decreases in neuronal activity.

Résumé

Cette dissertation décrit une nouvelle méthode pour mesurer les changements du volume sanguin cérébral veineux (VSC_v) accompagnant l'activation fonctionnelle normale. Elle utilise des méthodes quantitatives d'imagerie fonctionnelle par résonance magnétique (IfR-M) pour étudier les changements hémodynamiques et métaboliques accompagnant l'inhibition neuronale. D'abord, pour valider la base de la méthode VSC_v proposée, une étude relaxométrique du lobe occipital a été réalisée in vivo pour étudier la dépendance du temps de relaxation transversale tissulaire, $T_{2_{tissu}}$, de l'intervalle de refocalisation dans une séquence Carr-Purcell-Meiboom-Gill. La faible diminution du $T_{2_{tissu}}$ apparente avec l'augmentation de l'intervalle de refocalisation est compatible avec le sang comme étant la seule source significative de dépendance de T_2 sur l'intervalle de la refocalisation apparent dans la matière grise et blanche du lobe occipital. Dans des études relaxométriques suivantes de sang in vitro, l'ajustage simultanné de l'ensemble d'estimations de $T_{2_{sang}}$, obtenu sur une large gamme des valeurs du niveau intravasculaire d'oxygénation et de l'intervalle de refocalisation, a été effectué en utilisant différents modèles: le modèle chimique d'échange rapide et le modèle de la diffusion dans des faibles hétérogénéitées de champ magnétique. Les résultats soutiennent l'application d'un modèle de diffusion pour décrire, à 1.5 T, l'augmentation du taux de relaxation transversale due à la désoxihémoglobine. Etant donné l'unicité de la dépendance de $T_{2_{sang}}$ du taux de refocalisation dans la gamme d'intérêt, la nouvelle méthode de mesure du VSC_v - refocalisation veineux pour l'estimation du volume (VERVE) - isole le signal du sang par variation du taux de refocalisation. Un modèle d'activation fonctionnelle du cerveau a été développé et les données de relaxométrie du sang in vitro employées

pour déterminer l'effèt du niveau intravasculaire d'oxygénation sur le changement du signal VERVE induit par activation, permettant l'évaluation robuste des changements du VSC veineux. La méthode a été appliquée dans une étude de stimulation visuelle de sujets sains. En moyenne, un changement du volume sanguin cérébral veineux de 16±2% a été estimé. Cette méthode permet donc le contrôle continu et efficace du volume cérébral veineux de sang, pour explorer d'avantage le mécanisme fondamental de la réponse BOLD aux perturbations physiologiques, physiopathologiques et pharmacologiques. En conclusion, la consommation de l'oxygène (CMR_{O_2}) et les changements du débit sanguin cérébral (DSC) suivant la désactivation neuronale ont été examinés. Une relation linéaire entre les changements relatifs de CMR_{O_2} et de DSC a été trouvée, avec une pente de 0.44±0.04. Le rapport de couplage établi ainsi dans les régions d'activation et de désactivation neuronales est en accord étroit avec ceux observés par des études précédantes étudiant l'augmentation de la perfusion et la consommation de l'oxygène. Ces résultats caractérisent la baisse des paramètres hémodynamiques et métaboliques accompagnant la désactivation neuronale focale et établissent de ce fait la réponse BOLD négative soutenue comme marqueur d'une diminution de l'activité neuronale.

Original Contributions

The original contributions to this thesis are:

1. Observation of the preserved contrast between grey and white matter T_2 in the occipital lobe of healthy, young adults at 1.5 T.

2. Finding that a small shortening of the apparent T_2 in the occipital lobe with refocusing interval elongation is consistent with blood being the only significant source of refocusing interval dependence of apparent T_2 in grey and white matter of the occipital lobe at 1.5 T.

3. Design of an MR-compatible system allowing the rotation of a set of blood samples about their long axes, to prevent the settling of erythrocytes and enable use of human blood in in vitro MR blood relaxometry experiments.

4. Finding that the model of diffusion in weak magnetic field inhomogeneities is preferred over the fast chemical exchange model in describing the deoxyhemoglobin-induced blood transverse relaxation rate enhancement at 1.5 T.

5. Development of a novel functional magnetic resonance imaging method for quantification of changes in venous cerebral blood volume accompanying functional activation.

6. Development of a functional activation model describing the effect of the intravascular spin-echo BOLD effect on the activation-induced signal changes measured via the novel method for CBV_v monitoring.

7. Discovery of a linear 0.44±0.04 coupling ratio between ΔCMR_{O_2} and Δ CBF changes following both up- and down- regulation of neuronal activity.

8. Demonstration of the applicability of negative BOLD fMRI response as a marker of net decreases in focal neuronal activity.

Chapter 1

Introduction

Brain function exhibits both spatial specialization and complex interactions between distributed areas. Neuronal activity is predicated on continuous adjustments in focal hemodynamic parameters, to meet the local energetic demands. The increase in aerobic metabolism that follows a surge of neuronal activity results in an enhanced blood flow to the activated area, to supply nutrients and remove metabolic wastes. Like brain functioning, the cerebral vascular tree exhibits both hierarchy and spatial specialization: maps of hemodynamic changes thus closely follow those of neuronal activity. A sustained disruption in the local blood supply (due to stroke, for example) leads to a cessation of adenosine triphosphate (ATP) production, a breakdown of normal ion concentration gradients across the neuronal membrane and, eventually, permanent neurological damage. Therefore, maps of hemodynamic and metabolic rates constitute critical measures of both normal functional physiology and pathophysiology.

Functional MRI (fMRI), based on the blood oxygenation level dependent (BOLD) effect [200, 262], exploits the link between neuronal activity and metabolism to identify brain regions activated by tasks, stimuli, or pathological events (*e.g.* epileptic spiking). While BOLD fMRI has become the predominant tool for examining brain function, our understanding of the physiology underlying BOLD fMRI signal remains incomplete. Much work has been dedicated to the investigation of neuronal correlates of the BOLD

response under normal physiological conditions, at the core of establishing the validity of BOLD response as a marker of neuronal activation [11, 146, 190, 221, 327]. To facilitate quantitative interpretation of BOLD signal changes, in turn, a number of research groups [49, 77, 155, 158, 163, 191] have proposed models of the BOLD response dependence on key metabolic and hemodynamic parameters: the cerebral metabolic rate of oxygen consumption (CMR_{O_2}), cerebral blood flow (CBF) and cerebral blood volume (CBV). While CMR_{O_2} and CBF are customarily measured, no attempts have typically been made in these studies to quantify CBV directly: instead, a power law relationship between steady-state CBV and CBF is assumed based on the findings of PET experiments employing hypercapnic challenge in rhesus monkeys [135]. However, much is still unclear about the robustness and range of applicability of this relationship as well as the BOLD signal mechanism in general. ***The broad goals of this research were to develop a noninvasive MR technique for direct measurement of blood volume and explore the range of applicability of BOLD fMRI response as a marker of neuronal activity.*** Overall, the studies comprising this thesis were aimed at clarifying the origin and behavior of the BOLD fMRI signal and providing tools for noninvasive measurement of critical physiological parameters in both healthy and diseased brain.

The MR method developed allows continuous monitoring of the changes in the volume of deoxygenated blood and thus aids the investigation of healthy hemodynamic and BOLD mechanisms. Moreover, the technique has important clinical applications in the diagnosis and treatment of stroke, where both blood volume and flow are important indicators of the extent of penumbra and ischemic core. Furthermore, in view of the potential variability in the effect of stroke on the BOLD signal, the fMRI methods described enable correct interpretation of BOLD response changes in the course of the functional recovery following stroke. The study of sustained BOLD signal decreases critically extends the applicability of BOLD fMRI to investigations of neuronal deactivation and provides important evidence for the consistency of the coupling between metabolic and hemodynamic parameters in regions of increased and decreased neuronal activity.

The present thesis is based on four manuscripts. Following this introduction, necessary physiological and physical background regarding neuronal activation, BOLD fMRI, and existing in vivo CBV measurement techniques are presented in Chapter 2. Manuscripts describing our MR relaxometry studies in tissue and blood comprise Chapters 3 and 4 and are entitled "Quantitative T_2 in the occipital lobe: the role of the CPMG refocusing rate" and "Human Whole Blood Relaxometry at 1.5 T: Assessment of Diffusion and Exchange Models", respectively. The first of these papers was published in *Journal of Magnetic Resonance Imaging*; the second, in *Magnetic Resonance in Medicine*. These studies provide the basis for the blood signal isolation employed in our novel sequence for non-invasive venous cerebral blood volume quantification. The details of its implementation are the focus of "Venous Refocusing for Volume Estimation: VERVE fMRI" (in press with *Magnetic Resonance in Medicine*), the manuscript contained in Chapter 5. The next chapter includes the fourth paper, "Hemodynamic and Metabolic Responses to Neuronal Inhibition" (published in *Neuroimage*), which describes hemodynamic and metabolic changes accompanying sustained BOLD decreases in the context of neuronal inhibition. The final chapter summarizes all findings and considers the outstanding issues in CBV quantification and BOLD response interpretation.

Chapter 2

Background

2.1 Neuronal activation physiology

2.1.1 Neuronal Structure and Activity

The nervous system is composed of nerve cells, or neurons, anatomically the most diverse cells of the human body. The prototypical neuron is made up of a cell body (soma), a tree of receptive outgrowths, or dendrites, and an axon - a long process (possibly with many collaterals) from the soma to the target cell (*c.f.* Figure 2.1). At rest, the intracellular space has an excess negative charge relative to the extracellular one, producing a resting neuronal membrane potential of about -40 to -75 mV [354]. (The actual charge thus separated is very small relative to the total amount of charges in the intra- and extracellular fluids: the *bulk* of each of these fluids is electrically neutral [354].) This magnitude is dictated by the ionic concentration gradients and membrane permeability of the various physiological ions, preponderantly sodium and potassium ions. Sodium concentration is higher on the outside; potassium, on the inside ($[Na^+]_{out} \sim 150$ mM; $[Na^+]_{in} \sim 15$ mM; $[K^+]_{out} \sim 5$ mM; $[K^+]_{in} \sim 150$ mM; [354]). However, the membrane has a much higher permeability to potassium (with 50-75 times as many open potassium as sodium ion channels at rest [354]), so that the development of the resting membrane potential is predicated on the passive outward

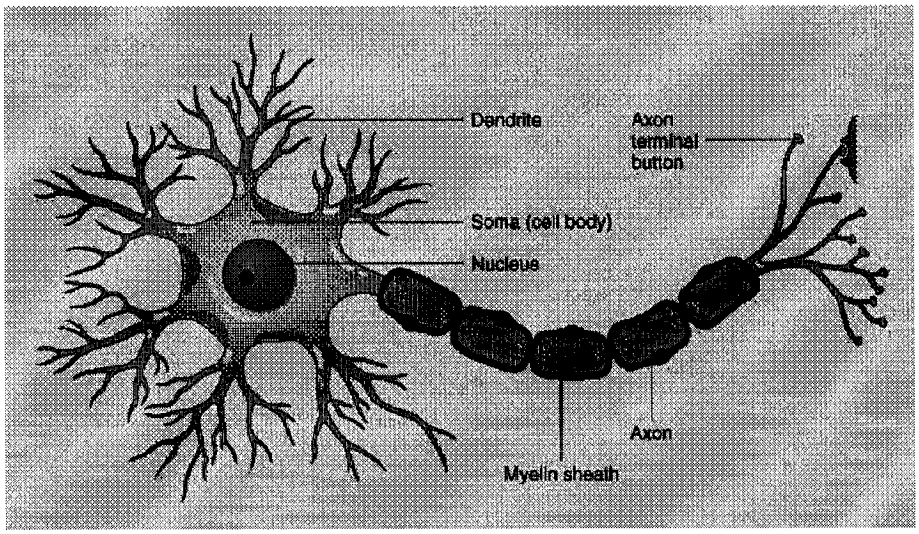

Figure 2.1: Anatomy of a model neuron [7].

diffusion of potassium ions. At the same time, passive diffusion of sodium and potassium ions down their electrochemical gradients is exactly offset by the active transport of these ions by the electrogenic Na,K-ATPase pump: 3 Na^+ are expelled for each $2K^+$ brought in, at a cost of one adenosine triphosphate (ATP) molecule. While this pump makes a small contribution to the resting potential, its activity critically maintains the concentration gradients which give rise to the ion diffusion and hence resting potential generation. (In the neurons containing the non-electrogenic active transport systems for expulsion of chloride ions, the resting membrane potential is further decreased by the net diffusion of chloride ions into the cells [354].)

At the heart of neuronal activity, and hence brain function, lies the generation and integration of electrical and chemical signals. Electrical signals arise via transient changes in the membrane potential. Neuronal firing (or action potential generation) requires a decrease in the amount of charge separation by at least $\sim$15 mV [354]. In most instances, this depolarization arises from temporal and spatial summation of the graded potentials generated by the total synaptic input to the neuron.

The signal transmission between neurons occurs at specialized junctions called synapses, shown in Figure 2.2. Typically, the synapse is chemical and occurs between the presynaptic nerve terminal and the dendrite or soma of the postsynaptic neuron.[1] The axonal terminal of the presynaptic neuron contains synaptic vesicles, filled with neurotransmitter molecules and docked at the active zones of the presynaptic membrane. Action potential induced membrane depolarization triggers opening of voltage-gated calcium channels in the membrane of the presynaptic neuron, which leads to a rapid influx of calcium ions and subsequent fusion of the vesicles with the membrane. Following exocytosis, the neurotransmitter molecules diffuse across the narrow (10- to 20-nm [354]) space separating the two neurons, a fraction of them binding to their receptors on the dense postsynaptic plasma membrane. (Most chemical synapses exhibit this asymmetrical structure and are hence uni-directional.) The neurotransmitter clearance typically occurs via passive diffusion into the neighboring fluids, enzymatic destruction, and/or active transport into the presynaptic terminal or nearby glia [139]. This active transport, as well as the subsequent regeneration of the neurotransmitter precursor (*e.g.* the conversion of glutamate to glutamine in the astrocytes [95]) and final neuronal repackaging of the neurotransmitter into the vesicles are all energy requiring processes.

The neurotransmitter binding induces (directly or indirectly, via a second messenger chemical system, typically involving a G-protein) opening of chemically-gated ion channels in the postsynaptic plasma membrane, thus changing the local postsynaptic transmembrane potential. A graded potential is thereby generated about 1 ms following the action potential in the presynaptic neuron [65]. It may be excitatory (if the postsynaptic membrane gets depolarized; typically resulting from an increase in sodium and potassium conductances) or inhibitory (if the postsynaptic membrane gets hyperpolarized or stabilized at the resting level, usually caused by increased permeability to potassium and chloride ions [65]). In the former case, the likelihood of the postsynaptic neuronal firing is increased; in the latter, decreased. In either case, the graded potential propagates passively and hence

[1] Like neuronal anatomy, the structure and organization of synapse exhibit considerable variation across the central nervous system: only the most representative scenario will be considered here.

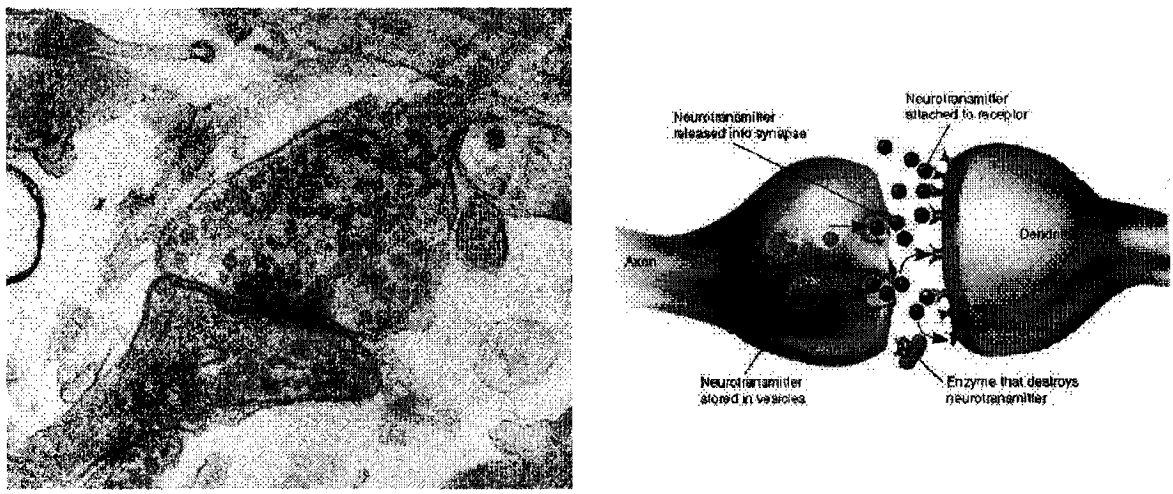

(a) (b)

Figure 2.2: An electron micrograph [292] (a) and a diagram [176] (b) of a chemical synapse between two neurons.

decrementally, due to transmembrane ion leakage, dying out within ~15 ms [139] while spreading 1-2 mm from the initiation site [354]. While the stimulus-dependent amplitude of a single postsynaptic potential is typically a tenth of the depolarization required for an action potential generation [65], all excitatory and inhibitory postsynaptic potentials undergo spatial and temporal (though possibly non-linear) integration. In general, hundreds of the thousands of synapses of a typical neuron (*c.f.* Figure 2.3) activate with sufficient temporal coincidence to enable addition [354]. Moreover, the threshold for action potential generation varies across the plasma membrane and is typically lowest at the sodium-channels rich initial segment of the axon (or axon hillock), producing a spatially heterogeneous weighting of the synaptic effectiveness based on the synapse's proximity to the axon hillock.

Upon sufficient depolarization of the plasma membrane at the axon hillock, voltage-gated sodium channels of the plasma membrane rapidly open, leading to a rapid influx of sodium ions into the cell and further depolarization. The electrical gradient, which opposes potassium efflux and promotes sodium influx, thus decreases, so that potassium efflux rises while sodium influx wanes. Nevertheless, the depolarization-triggered opening of neigh-

Figure 2.3: Micrograph of neuronal soma with numerous synapses [176].

boring voltage-gated sodium channels eventually produces a net inward movement of positive charges (sodium influx surpassing potassium efflux), triggering a stimulus-independent positive feedback cycle (between opening of voltage-gated sodium channels, sodium influx, and membrane depolarization), and generating a local action potential [354]. The depolarization phase may be followed by an overshoot (whereby the membrane potential rises above 0). The opening of the voltage-gated sodium channels, however, is followed by slower opening of voltage-gated potassium channels. Moreover, sodium channels inactivate (close) rapidly, with the delayed closing of the additional potassium channels causing membrane afterhyperpolarization. While the actual amount of charge transported across the membrane in the course of the action potential (lasting about 1 ms [354]) is minuscule relative to the total number of cellular ions (intracellular $[Na^+]$ increases by $\sim$0.04% with each action potential [65]), the long-term preservation of the ionic gradients and hence the excitability of the neuron is ensured by the continued operation of the Na,K-ATPase pump. Similarly, to maintain the transmembrane calcium concentration gradient of the terminal button in the long term, calcium ions are pumped out of the cell via two ATP-requiring transport systems [27].

The local current, produced by an action potential, depolarizes the neighboring membrane to the threshold level and thereby regenerates the action potential in the next segment of the axon, allowing for non-decremental action potential propagation, with speeds varying from 0.5 m/s in unmyelinated fibers of small diameter to 100 m/s in myelinated axons of large diameter (the insulating nature of myelin decreasing charge leakage and the resistance being inversely proportional to the cross-sectional area of the fiber) [354]. Due to the inactivation of voltage-gated sodium channels at the peak of the action potential, an interval of no excitability ensues (a.k.a. absolute refractory period); followed by a relative refractory period characterized by limited excitability due to increased action potential threshold resulting from partial inactivation of the sodium channels and increased activation of the potassium channels. The action potential frequency of a typical neuron does not exceed $\sim$100 Hz, though some neurons exhibit much higher firing rates under transient conditions [354]. Furthermore, due to the forementioned long duration of excitatory postsynaptic potentials (relative to the action potentials), action potentials typically occur in bursts rather than as isolated events [354].

2.1.2 Metabolic Response to Neuronal Activation

Glucose Metabolism

While the brain accounts for only $\sim$2% of total body weight, it receives $\sim$11% of cardiac output and consumes $\sim$20% of all oxygen and 25% of total glucose expended by the resting body [332], figures testifying to the very high energetic demands of biophysical and biochemical processes comprising neuronal activity. Cerebral metabolic rates are affected by the overall body state (*e.g.* normal healthy feeding *v.s.* diabetes, fat-feeding or starvation), and vary across the different brain regions (*e.g.* grey matter *v.s.* white matter). (Apart from being, by far, the most preferred substrate of brain metabolism, glucose is also a precursor of neurotransmitters such as glutamate, GABA and acetylcholine; it may be incorporated into various lipids and proteins or stored for later use as glycogen [92].)

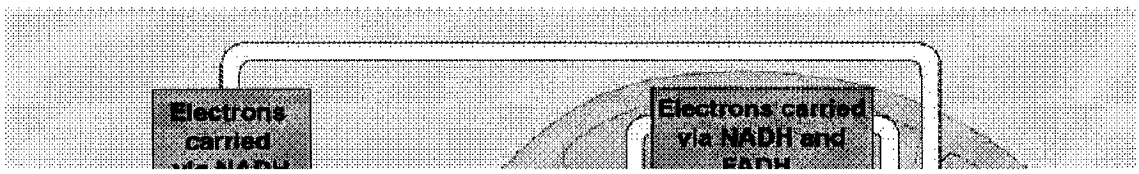

Figure 2.4: Diagram of cellular respiration [7].

Under normal steady-state conditions, almost all of the brain's global energetic demands (in the form of ATP, the primary energy currency of the body, with 7-12 kcal of free energy released upon breaking of its high-energy phosphate bond [325]) are supplied by oxidative metabolism of glucose ($C_6H_{12}O_6$), the O_2 to glucose ratio being $\sim$5.5 mol/mol [332]. This figure is slightly less than the 6.0 mol/mol stoichiometric ratio of $O_2/C_6H_{12}O_6$ predicted by complete oxidation of glucose, possibly resulting from accumulation of a number of intermediates (*e.g.* lactate) [227]. The complete oxidation of glucose to carbon dioxide and water entails several stages, summarized below and illustrated in Figure 2.4. (A thorough discussion of the entire process may be found in Ref. [322].) The first stage is glycolysis, an anaerobic breakdown of glucose to pyruvate involving a series of enzyme catalyzed

reactions taking place in the cytosol. The overall reaction is given by:

$$C_6H_{12}O_6 + 2NAD^+ + 2ADP + 2P_i \rightarrow 2CH_3(C=O)COO^- + 2NADH + 2H^+ + 2ATP + 2H_20, \quad (2.1)$$

where $CH_3(C=O)COO^-$ is pyruvate and P_i is the inorganic phosphate group. Pyruvate may then be reduced to lactate by lactate dehydrogenase, while oxidizing NADH:

$$CH_3(C=O)COO^- + NADH + H^+ \rightarrow CH_3 - CHOH - COO^- + NAD^+. \quad (2.2)$$

The last reaction is reversible and usually happens under anaerobic conditions, but in the brain may occur even in the presence of O_2. Overall, the anaerobic breakdown of one molecule of glucose provides 2 molecules of ATP in addition to either 2 molecules of pyruvate and 2 molecules of NADH or just 2 molecules of lactate. The rate of glycolysis is controlled, to maintain steady ATP levels, through regulation of two glycolytic enzymes.

The slower, but energetically much more prolific stages, of tricarboxylic acid cycle and oxidative phophorylation, take place in the mitochondrion and require the presence of oxygen. After transport into the mitochondrion, pyruvate is oxidized to acetyl-CoA and CO_2 by the pyruvate dehydrogenase complex. Next, acetyl-CoA enters the citric acid cycle, each turn producing 3NADH, one $FADH_2$ and one ATP molecule while releasing two molecules of carbon dioxide. (The cycle rate is tightly controlled, via regulation of the pyruvate dehydrogenase complex and 3 enzymes of the citric acid cycle, inhibited by both ATP and NADH.)

In the electron transport chain, NADH and $FADH_2$ molecules donate two electrons to an atom of oxygen (from O_2), which combines with hydrogen protons in the mitochondrial matrix, thus forming water and providing energy for the production of 3 and 2ATP molecules, respectively. (The two NADH produced in glycolysis of one molecule of glucose are transferred from the cytosol into the mitochondrial matrix via the glycerol-3-phosphate shuttle, yielding energy for the synthesis of 2 ATP molecules from a pair of

electrons passed to oxygen.) The rate of this oxidative phosphorylation is limited by the availability of ADP.

The net reaction of the aerobic catabolism of glucose in the brain is thus given by:

$$C_6H_{12}O_6 + 6O_2 + 36ADP + 36P_i \rightarrow 6CO_2 + 6H_2O + 36ATP. \quad (2.3)$$

The energy efficiency of the entire process is ~44-66% under physiological conditions [112]. As mentioned above, the individual stages of glucose catabolism are tightly regulated, being driven by an increase in the local ADP (over ATP) concentration. Thereby, a shortage of energy supply leads to upregulation of glucose metabolism.

Most importantly, from the standpoint of functional neuroimaging that is sensitive to metabolic and hemodynamic parameters, glucose consumption is also tightly correlated to *local* functional activity [188, 278, 310, 330]. The rate of glucose consumption has been shown to follow the upregulation in focal neuronal activity in a graded fashion [182], diminish with decreases in local activity [188], and rise with its increases [278, 330].

As suggested earlier, the actual rate of glucose consumption varies across the brain [333]: glucose consumption is much (3-4 times [50]) higher in grey than in white matter, likely a reflection of higher synaptic density of GM [138]. Within the cortex, CMR_{glu} peaks in layer IV [188], known to contain the highest concentration of synapses, yet a low density of soma [50]. In the spinal cord of rodents, CMR_{glu} was found to follow the stimulation intensity in the region rich in axon terminals while remaining at its baseline level in the perikarya of the same pathway [182]. (The paucity of voltage-gated sodium channels may result in the predominance of the energetically inexpensive electrotonic conduction over action potential propagation through soma membrane [332].)

In an influential yet controversial (*c.f.* [59]) theory, Magistretti *et al.* suggested that astrocytes play a key role in the coupling between functional activity and metabolism [230, 231, 275, 276, 349]. In the astrocyte-neuron lactate shuttle hypothesis, glutamate is cleared from the synaptic cleft by an active uptake into astrocytes [23] mediated by Na^+-dependent transporters. The accompanying influx of sodium, in turn, stimulates glucose

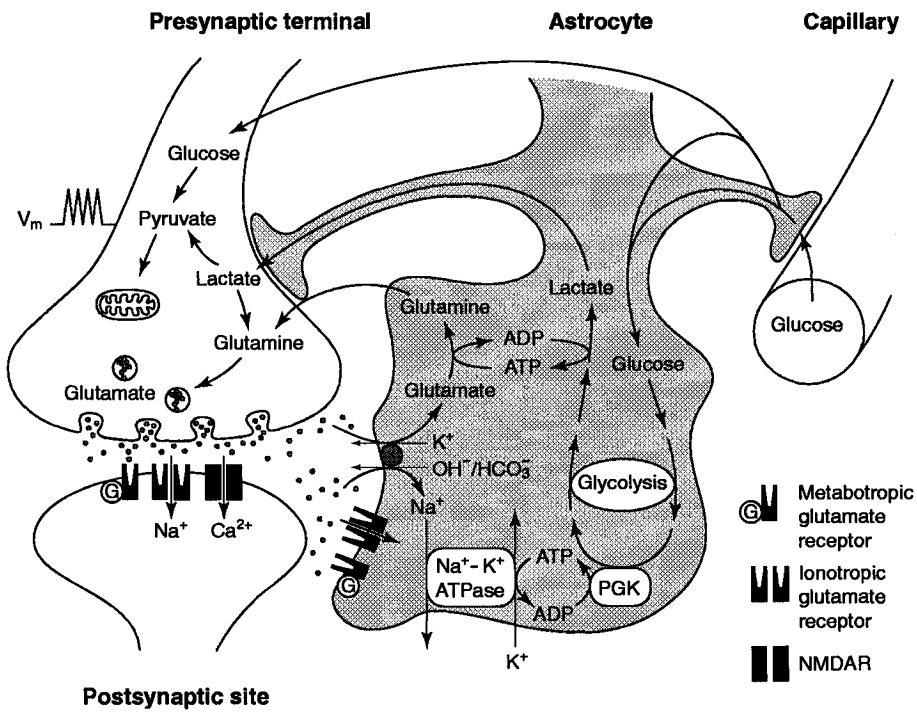

Figure 2.5: Schematic of the proposed coupling between glutamate release and glycolysis in astrocytes [229].

uptake from the bloodstream by the astrocytes, the finger-like astrocytic endfeet having privileged anatomical contacts with individual endothelial cells of the capillary walls [181]. The extracted glucose undergoes glycolysis in the astrocytes, with the ATP produced used to drive the astrocytic Na,K ATP-ase pump (thereby restoring the ionic gradients across the astrocytic membrane) and provide energy for the enzymatic conversion of glutamate to its precursor, glutamine. Both the end product of astrocytic glycolysis, lactate, and glutamine are then transferred to neurons: lactate entering the tricarboxylic acid cycle; glutamine being converted to glutamate, to support ongoing signaling (*c.f.* Figure 2.5) [229]. This theory thus predicts a 1:1 stoichiometry between glutamate cycling and glycolytic glucose utilization, a prediction that remains to be validated in the healthy human brain.

[^{13}C] MRS studies in anaesthetized rat cerebral cortex reported a 1:1 stoichiometry between glutamate-glutamine cycling and aerobic metabolism of glucose in neurons, suggesting that glutamatergic activity dominates the metabolic costs of functional activity [318–

320]. Given this association between metabolic demands and synaptic activity, it has been postulated that an increased local CMR_{glu} reflects an upregulation in the activity of the afferent inputs to the region rather than its output [331]. Nevertheless, the finding of 1:1 stoichiometry just described has been challenged both in 9.4 T [^{13}C] MRS studies of deep pentobarbital anesthesia in the rodent brain [61], as well as in 4 T [^{13}C] MRS studies of the healthy human brain [137]. The latter study found the cycling between neuronal glutamate and glial glutamine to account for only $\sim 41 \pm 14\%$ of total oxidative glucose consumption [137]. Finally, a very recent study employing two-photon fluorescence imaging and confocal microscopy in rat hippocampal slices reported an initial upregulation in the postsynaptic dendritic oxidative phosphorylation followed by a delayed (10 s after stimulus onset) rise in the astrocytic glycolysis, the production of NADH by the latter surpassing NADH consumption by the former by an average 57% after a 20-s stimulus (and even more so with longer stimuli) [183].

On the other hand, detailed biochemical and biophysical data have been used in combination with a theoretical model to estimate the energy budget of specific processes comprising functional activity [13]. Reversing the postsynaptic effects of the neurotransmitter (specifically, glutamate) has thus been predicted to require 74% of all energy spent on signaling [13]. A very limited relative cost of resting potential maintenance and glutamate recycling was suggested [13]. While the analysis was based on anatomic and physiologic data from the GM of the rodent brain, these primate brain predictions take into account a 10-fold decrease in the density of neurons despite the preserved density of synapses [1] in human with respect to rodent brain.

Notwithstanding the above arguments, neuronal signaling is considerably faster than the metabolic processes just described. It is, at the moment, not clear how this discrepancy in the temporal scales might be resolved to allow tight coupling. Buffering by the extracellular space has, however, been suggested [229]. Overall, the relationship between functional activity and metabolism is still an area of active research.

Glucose is delivered to the brain by the blood, with ~30% [265] of glucose in the capillaries being extracted by the tissue via facilitated diffusion, likely using a high-affinity, but low capacity transporter system [123, 293]. Only ~50% of the extracted glucose is actually catabolized by neurons and glia (the rest being cleared, with CO_2 by venous outflow) [124]. In other words, an excess of glucose is delivered to the "resting" brain, so that CMR_{glu} could in principle double without any flow increases. (Typically, below 50% focal CMR_{glu} increases following normal functional activation in healthy adults have been measured via ^{18}F-Fluorodeoxyglucose PET, with larger or equal CBF increases quantified via $[^{15}O]H_2O$ PET [107, 122].) Moreover, no effect of mild or moderate hypoglycemia has been observed on the CBF response to normal physiological stimulation [283]. Similarly, hyperglycemia produced no changes in the blood flow response to functional activation in anesthetized rats [373]. At the same time, CMR_{glu} increase was found unperturbed by inhibition of neuronal nitric oxide synthase, which abolished the blood flow increase following whisker stimulation in alpha-chloralose anaesthetized rats [64]. Nevertheless, recent concomitant measurements of plasma glucose and blood flow in combination with a reversible Michaelis-Menten model for prediction of brain glucose reported a sharp rise in CBF following a drop of brain glucose to zero in alpha-chloralose anesthetized rats [62]. It is thus surmised that under normal physiological conditions blood flow upregulation following functional activation is not subserving the increased demand for glucose [50], though the CBF increase under extreme hypoglycemic conditions likely occurs to enhance glucose delivery to the brain, accompanied by gradual utilization of brain glycogen stores [62, 63, 161].

Oxygen Consumption

Whether focal, transient surges in energetic requirements following functional activation are met by oxidative or non-oxidative glucose metabolism has been a subject of intense debate since the early PET studies reporting very small CMR_{O_2} rise following visual stimulation, much smaller than either CMR_{glu} or CBF increases [106, 107]. There is a very

limited (if any) oxygen buffer available to the tissue [212], so that any upregulation in glucose oxidation requires an increased extraction of O_2 from the bloodstream. (The nature and efficiency of oxygen extraction across the blood-brain barrier differ significantly from those of glucose [126] and are intricately connected to the properties of blood vessel walls and overall hemodynamics: they will be described in the section 2.1.3.) A disturbingly wide range of CMR_{O_2} increases (especially relative to concomitant CBF changes) following functional activation has been reported in various PET studies [107, 127, 166, 237, 295, 296, 312, 351, 352]. This large variability has been ascribed to a number of methodological confounds: a strong dependence of the estimates on the poorly described and likely spatially varying blood-tissue partition coefficient; bias due to a sizable partial volume effect resulting from a rather low spatial resolution of the method; temporal instability when using several PET scans employing different tracers (*e.g.* to determine the oxygen extraction function); a frequent failure to account for the remaining radioactivity of the vascular bed in the analysis [165, 167]. Accounting for such effects in one study produced estimates of $\sim$6% CMR_{O_2} (and 24% CBF) increase in healthy volunteers in response to visual stimulation [165]. This $\sim$1:4 CMR_{O_2} to CBF coupling ratio is still smaller, though comparable to the ones measured using functional magnetic resonance imaging and hypercapnic calibration (to be described in Chapter 6), where 1:2 to 1:3 coupling between ΔCMR_{O_2} and ΔCBF have been reported in visual and motor cortices following functional activation [12, 77, 155, 185, 191].

The findings of magnetic resonance spectroscopy studies have also varied. Consistent with a significant anaerobic glucose metabolism, an accumulation of lactate following functional activation has been reported [285, 307]. Nevertheless, lactate production could not fully account for the disproportionately large CMR_{glu} *v.s.* CMR_{O_2} upregulation following sensory stimulation in awake rats [227]. Moreover, the 1:1 stoichiometry between glutamate cycling and oxidative glucose metabolism reported in a range of [^{13}C] MRS studies of anaesthetized rodent brain [318] has been challenged [61]. A much lower ($\sim$0.4) stoichiometry between these two processes has recently been recorded in in vivo human

studies (consistent with ~90% of astrocytic ATP production occurring via glucose oxidation, but with the flux from neuronal Glutamate to glial Glutamine comprising only ~40% of glucose oxidation) [137].

Several hypothesis have been put forth to explain relative contributions of anaerobic *v.s.* aerobic glucose metabolism, taking into account the sharp contrast in energetic efficiency and duration of the two processes. It has thus been suggested that glycolysis does increase more than oxidative glucose catabolism during the initial response to functional activation, the accumulated intermediary products being subsequently aerobically metabolized [227]. Alternatively, it has been proposed that the relative contribution of glycolytic *v.s.* oxidative breakdown of glucose actually varies with the complexity of the stimulus, Krebs cycle ramping up only for more complex stimuli that require a greater level of postsynaptic activity [125]. In any event, the temporal evolution of the upregulation of the two processes will likely not be resolved by the aforementioned techniques, due to their intrinsic limits on spatial and temporal resolution.

The frequently quoted reason (among the subscribers to aerobic metabolism of glucose as a means of supplying energy for heightened focal functional activity) for a disproportionately large activation-induced increase in flow, relative to that in oxygen consumption is that the efficiency of oxygen extraction from the capillary network (*i.e.* oxygen extraction fraction (OEF)) decreases with increases in flow [48]. The CMR_{O_2}, given by the product of arterial oxygen saturation, blood flow and OEF, thus decreases. This theory, known as the oxygen limitation model, assumes limited diffusibility of oxygen across the capillary wall (as observed in the microcirculation of the canine brain [184]) and constant surface area of the capillary network (blood flow increase thus being mediated by a rise in capillary blood velocity rather than capillary recruitment, as described in the next section). Given these assumptions, an increase in flow leads to a drop in the capillary transit time which in turn causes a decrease in the oxygen extraction function [48], so that a much larger (~6-fold) CBF increase is required to support a given rise in CMR_{O_2}. In other words, given low tissue P_{O_2} yet constant parenchymal geometry, the O_2 concentration gradient and hence

O_2 diffusion are increased through a rise in the capillary P_{O_2}, achieved by a drop in the O_2 extraction [50]. Nonetheless, some contribution to the increase in oxygen diffusion is likely afforded by a flow-dependent adjustment in capillary O_2 diffusivity [163], capillary dilatation (causing a reduction in the diffusion distance), and a decrease in small, but likely non-zero mitochondrial O_2 concentration (increasing the O_2 concentration gradient) [50]. The relative contributions of these mechanisms are still being researched.

2.1.3 Hemodynamic Response to Neuronal Activation

Cerebral Vasculature

The brain is supplied by blood and thus oxygen and glucose via a pair of internal carotid arteries and a pair of vertebral arteries. The internal carotids bifurcate, supraclinoidally into the anterior and middle cerebral arteries. The anterior cerebral artery supplies the medial surface of the cerebral cortex, frontal pole, and anterior portions of the corpus callosum; as well as the anterior limb of the internal capsule, the inferior portions of the head of the caudate and anterior globus pallidus via perforating branches. The middle cerebral artery, in turn, supplies the temporal lobe, anterolateral frontal lobe, and parietal lobe; its perforating branches supply the posterior limb of the internal capsule, part of the head and body of the caudate as well as globus pallidus. The vertebral arteries unite within the cranium to form the basilar artery, which bifurcates into posterior cerebral arteries that supply the occipital and inferior temporal lobes, with a branch supplying the choroid plexus. The arterial circle of Willis is formed in front by the anterior cerebral arteries, interconnected by the anterior communicating; and behind by the two posterior cerebral arteries, connected on either side with the internal carotid by the posterior communicating artery (with little mixing of blood occurring between the major arteries under normal conditions) [53, 306].

The drainage of blood and hence removal of such metabolic by-products as carbon dioxide and hydrogen ions from the tissue is achieved by the deep and superficial groups of veins. The deep cerebral veins drain the choroid plexus, periventricular regions, di-

encephalon, basal ganglia and deep white matter. They empty into the internal cerebral and the great cerebral veins. In turn, the superficial veins drain the cortex and subcortical white matter and empty into the superior sagittal or basal sinuses [53]. In toto, cerebral vasculature comprises only about $\sim$4% of brain volume [50].

The biophysical properties of the blood vessels change considerably in moving from arteries over to veins, a reflection of the progressive changes in the composition of the vascular wall. With the high concentration of elastin in their endothelial lining, large arteries (with diameter on the order of a few mm's and a $\sim$1-mm wall [306]) serve as "pressure storers" of the circulation (*c.f.* Figure 2.6): they stretch during ventricular systolic ejection and then contract in the following diastole, thereby propelling the blood. Small arteries and arterioles (with diameters as small as a few tenths of microns) are regarded as "resistance vessels" due to the abundance of circular smooth muscle fibers in their walls. The consequent contractile capacity ensures smooth, continuous flow through the capillary network and allows dynamic adjustments to match the local blood flow demands. The overall structure of the arterial network is fractal [288, 368]. The point where the arterioles branch into capillaries is frequently encircled by a smooth muscle fiber, the precapillary sphincter that may open or close the capillary entrance. Fine control of microvascular blood flow is also enabled by vascular pericytes, found on the abluminal surface of the capillary wall at or close to the capillary branching points [145]. The distribution of these control structures varies considerably across the cortex [145, 206]. Highly spatially specific hemodynamic regulation (on the scale of cortical columns, *i.e.* over 0.3-0.5 mm [71]), albeit in the horizontal cortical direction, has been observed in optical imaging studies [72, 220, 232] as well as by high-field fMRI [90]. A considerably lower hemodynamic specificity has been reported in the cerebellar cortex [207].

The capillaries are but a few microns in diameter (spaced, on average, by $\sim 24\mu$m [306]) and contain very little of either elastin or smooth muscle in their walls [306]. Significant dilation of the capillaries is precluded by the glial endfeet, which typically wrap around the capillary walls [139]. The endothelial lining of most cerebral capillaries (barring some

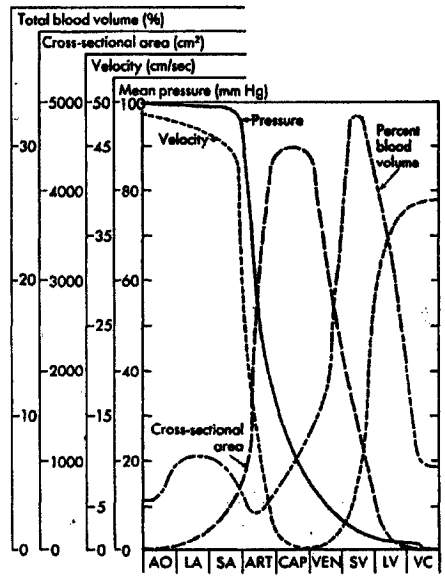

Figure 2.6: The hemodynamic parameters across the vascular tree [306]. AO: aorta; LA: large arteries; SA: small arteries; ART: arterioles; CAP: capillaries; VEN: venules; SV: small veins; LV: large veins; VC: venae cavae.

regions of the hypothalamus, pineal gland and area postrema [139]) is characterized by tight intracellular junctions, forming the so called "blood brain barrier." The capillary wall is thus permeable to water, carbon dioxide, oxygen and most lipid-soluble substances; only slightly permeable to small ions, and impermeable to plasma proteins and large, non-lipid soluble molecules [139]. Due to the very large surface-to-volume ratio of the capillary network, most of the exchange of substances between blood and tissue occurs across the capillary walls. In view of their short length (of $\sim$10-300μm [306]) and a high degree of tortuousity, the distribution of cerebral capillaries is usually modeled as random [306]. However, capillary density varies considerably across the brain, as reflected by the 2-3:1 ratio between grey and white matter capillary densities [287] and the higher concentration of capillaries in primary sensory areas, motor cortex and possibly speech-related regions [145].

Capillaries unite to form venules (of $\sim$20μm diameter [306]), which combine at roughly 90° angles to form larger venules [350]. The principal intracortical veins ($\sim$75 μm diame-

ter, ~400 μm apart) traverse the cortex and join at the cortical surface into pial veins [350]. The veins, a few mm in diameter, contain ~45-65% [273, 353] of the resting cerebral blood volume and have rather thin (~500μm [306]), elastin-poor walls, containing very little smooth muscle [329]. They are thus as much as 8-fold more distensible than arteries [139] and are known as "volume storers" of the circulation. (As much as 90% of any systemic fluid increase is taken up by the veins, their blood storing capacity being 12-18 times that of arteries [329].) Veins are innervated by sympathetic nerve fibers, whose basal stimulation produces a slight contraction of the smooth muscles in the venous walls, reducing the venous volume by about 20% [177].

Cerebral Blood Flow

Brain tissue survival depends on continual blood flow, to bring oxygen and nutrients (*e.g.* glucose, amino and fatty acids), remove the waste products of the metabolism (*e.g.* carbon dioxide and hydrogen ions), cool down the tissue and maintain its fluid content as well as transport hormones [139, 306]. Formally, cerebral blood flow (CBF) is defined as the rate of delivery of arterial blood to the capillary bed of a given mass (or volume) of parenchyma [50]. It is thus given by the ratio of cerebral blood volume (CBV) and the vascular transit time, a relationship known for over a century as the central volume principle [344].

The mean basal CBF in a healthy adult is ~60 ml/100g min (or about 0.01 s^{-1} assuming tissue density of 1 g/ml) [50], for a cumulative 750-900 ml/min or ~15% of total blood flow of the the body [139]. Predictably, cerebral blood flow exhibits pronounced heterogeneity, changing both with functional state (CBF being increasing during an epileptic seizure [147] but decreasing under anesthesia [204]) and across different areas. The regional blood flow varies as much as 18-fold between the different regions of a rat brain [100], likely resulting from regional differences in capillary density [102] as well as from transit times variation (with 0.3 to 0.6 s capillary transit time in GM, and 0.6-0.9 s in WM [297]). There is thus a four-fold larger CBF but only two-fold bigger CBV in grey, as compared to white matter [306] (blood volume fraction being ~6% in GM and ~3% in WM [353]). A

significantly lower (by 25-55% [102]) microvascular, compared to macrovascular, hematocrit (Hct) is caused by the preferential flow of erythrocytes through the central part of the vessels (a.k.a. axial streaming) and a greater plasmatic than erythrocytic velocity. This phenomenon is known as the Fahraeus effect [98, 286]. The cerebral-to-large-vessel Hct ratio decreases with vasodilatation [305] and varies both across subjects and with absolute Hct value [314]. Red blood cells' deformation during the passage through the capillary network likely explains the reported irregularities of the capillary flow [50, 356]. (Intermittent flow has traditionally been associated with transient increases in local metabolic demands, with smoother flow typical of resting conditions [177, 273].)

Due to the very high sensitivity of the brain to disruptions in its homeostasis, an elaborate system of CBF control operates on a global scale. Autoregulation maintains a constant blood flow despite arterial pressure fluctuations, over the mean arterial blood pressure range of 60 to 140 mmHg [139]. Autoregulation is likely achieved through a combination of mechanisms: myogenic activity, whereby the cerebrovascular resistance changes (via adjustments in arteriolar diameters through smooth muscle contractions in the vessel wall); and metabolic influence, whereby increased metabolism leads to the production of a range of vasodilatory substances such as adenosine, carbon dioxide, lactic acid, histamine, potassium and hydrogen ions [139]. Autoregulation is further modulated by the vasoconstricting effects of the renin-angiotensin system as well as autonomic nervous control: sympathetic and parasympathetic nerve fibers innervate large superficial and some penetrating arteries, their maximum stimulation inducing global CBF decreases and increases, respectively, on the order of $\sim$10% [196, 205, 247]. The vasoconstriction produced by the sympathetic activity becomes very significant during acute hypertension [147].

The regulation of transient increases in the focal blood flow, following functional activation, is still incompletely understood, though speculations about its existence had been made over a century ago [302]. In view of the earlier discussion of low resting oxygen buffer yet activation-induced oxygen consumption increases, it is tempting to assume that the tissue oxygen concentration is involved in the local flow regulation, at least when it

comes to normal focal functional activation (as discussed earlier, CBF serves a variety of functions, so that versatility in its overall control mechanisms is to be expected). While it was once postulated that oxygen depletion following heightened activity causes relaxation of the smooth muscle in the vessel wall (its contraction requiring energy from oxidative glucose metabolism) [139], it appears that oxygen is not directly involved in CBF regulation. Just like hyperglycemia, hyperoxia produces no effect on the stimulation-induced blood flow changes [373]. Moreover, partial pressure of oxygen in the tissue increases following activation (due to the disproportionately large CBF, relative to CMR_{O_2} increase, as described in subsection 2.1.2) [212].

Although the mechanism causing local arteriolar smooth muscle relaxation is still under investigation, a number of different agents have been implicated, most notably: H^+, CO_2, K^+, Ca^{++}, adenosine and nitric oxide [50]. A local increase in the concentration of hydrogen protons has been shown to cause dilatation of the brain arterioles, with alkalosis producing the opposite effect [50]. Localized acidosis may come about due to increases in CO_2 (following upregulation in aerobic glucose catabolism), as carbon dioxide readily diffuses across both neuronal membranes and capillary wall, forming bicarbonate and hydrogen ions in water. (Unlike oxygen, carbon dioxide is a somewhat counter-intuitive primary agent of local blood flow control since P_{CO_2}, and hence the accompanying vasodilatatory effects, passively *follow* the rate of local oxygen consumption [306].) At any rate, the temporal evolutions of pH and CBF changes during functional activation are not entirely concordant [207].

According to the cation hypothesis of local CBF regulation [203], the forementioned (*c.f.* section 2.1.1) activation-induced rise in extracellular potassium and drop in extracellular calcium ion concentrations lead to local flow increases (potassium inhibiting and calcium stimulating smooth muscle contraction [139]). Astrocytic release of potassium in response to potassium buildup in the synaptic cleft may further enhance the rapidity of the vasodilatory effect of this ion [271]. Nevertheless, large discrepancies in the temporal evolution of extracellular potassium concentration and CBF have been reported in the cere-

bellar cortex and thus only a secondary role in CBF control assigned to potassium [207]. Increased dephosphorylation of adenosine phosphates (ATP, ADP, and AMP) following neuronal activation [81, 371] as well as a transient drop in oxygen tension [303] increase the amount of extracellular adenosine, another vasodilatory agent [360], though this control pathway may be stimulus-dependent [207].

Perhaps the most prominent current theory emphasizes the role of nitric oxide (NO) in local CBF control as well as modulation of all forementioned potential mediators [84, 164, 363]. The glutamate released from the presynaptic terminal interacts with NMDA receptors on the postsynaptic membrane, increasing the concentration of calcium ions in the postsynaptic neuron and thereby enhancing the activity of neuronal nitric oxide synthase (nNOS) [73]. At the same time, the interaction of glutamate with AMPA and kainate receptors on the astrocytic membrane engenders the release of arginine into the synaptic cleft by the astrocyte. This arginine is then taken up by the postsynaptic neuron and converted to NO and L-citrulline by nNOS. Nitric oxide is then released from the postsynaptic neuron; it rapidly diffuses through the tissue and causes local arteriolar dilatation, hence commencing the hemodynamic response (*c.f.* Figure 2.7) [73]. The contribution of nitric oxide to CBF regulation has, however, been found to vary across different brain regions [64]. Overall, it is likely that a number of vasodilators are involved in the local CBF control, this set possibly varying both across brain regions and with the type of stimulation (*i.e.*, the stimulated afferent inputs) of a single area [132, 207].

In line with the preceding comments on the structure and properties of the cerebral vasculature, one or more of the forementioned vasodilatory substances act on the smooth muscle in the arteriolar wall, causing a drop in the arteriolar vascular resistance within 1-2 s [71] following functional activation. (In the simplest model of laminar flow in a cylindrical vessel, flow is inversely proportional to the resistance, which in turn varies with the fourth power of the vessel diameter [50].) Despite a large *relative* increase in the arteriolar volume, the contribution of this volume change to the total CBV increase is likely limited due to a rather small resting volume residing in the arterioles [50]. On

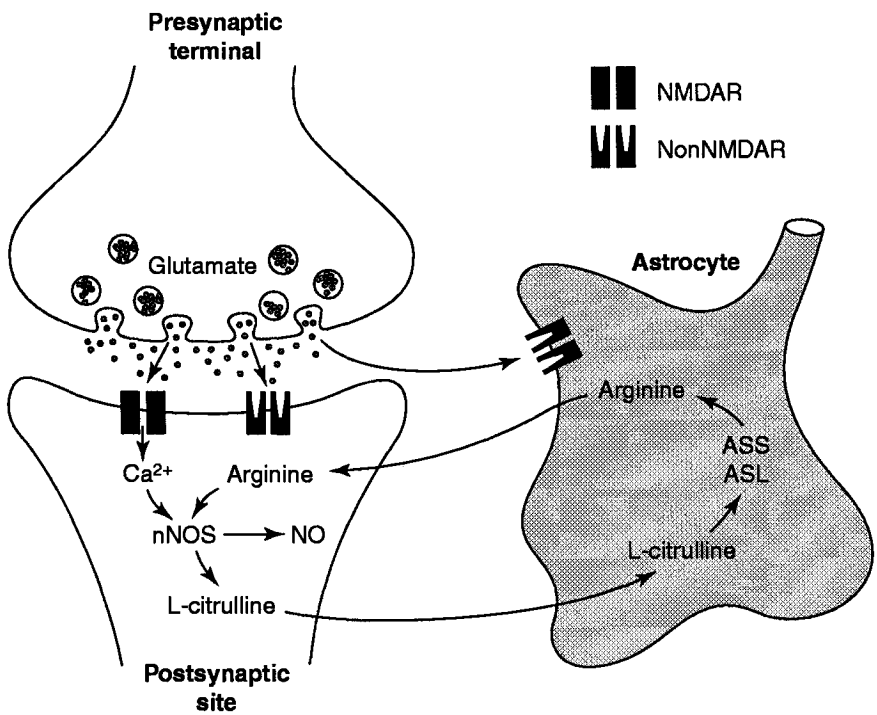

Figure 2.7: Diagram of the proposed coupling mechanism between glutamate release and nitric oxide production [73].

the level of capillaries, the focal rise in CBF is predominantly mediated by an increase in capillary blood velocity rather than capillary dilatation or recruitment [101] (though some dilatation of capillaries [86] and functional recruitment [3] may take place). Following considerable controversy [129], a very limited capillary recruitment (either opening of new capillaries or perfusion with RBCs of capillaries previously containing only plasma) is now believed to accompany blood flow increases under normal physiological conditions [22, 128, 195, 355, 356]. The ensuing rise in the pressure seen at the veins causes their passive dilatation and results in a significant increase in the total blood volume (in view of the aforementioned large resting volume contribution of the veins). The total blood volume increase is customarily assumed to be related to total blood flow increases through a simple power-law relationship ($CBV=0.8\ CBF^{0.38}$), obtained through hypecapnic perturbations in anesthetized rhesus monkeys [135] and recently reproduced in humans both under hypercapnic conditions and in response to visual stimulation [169, 171]. Consistent with this view of CBV changes being a result rather than the cause of the blood flow increase, is the observation of delayed CBV relative to CBF response in rodent somatosensory cortex following forepaw stimulation [235].

Over the normal operating range, absolute increase in CBF with functional activation is believed to be independent of the baseline blood flow or oxygen availability (*i.e.* the additive model of CBF changes is thought to apply) [50, 68, 153, 154, 321]. Therefore, vasodilators (*e.g.* carbon dioxide or acetazolomide) decrease [16, 45], while vasoconstrictors (*e.g.* caffeine) increase [250] activation-induced percent flow increases. (Such observations, of preserved absolute blood flow response despite baseline rises in CBF, do not support the oxygen limitation model. To explain this discrepancy, the maintenance of ratio of oxygen to carbon dioxide tension in the mitochondria has recently been suggested as the purpose of cerebral blood flow changes [51].) Despite the reported strong correlations between CBF and different measures of functional activity [52, 147, 168, 272] (CBF likely primarily reflecting the level of synaptic activity [207]), the actual relationship of flow and neuronal activity is probably nonlinear, as evidenced by recent studies of the roden-

t barrel cortex [80, 180]. An inverse sigmoid function has thus been used to model this relationship [180].

2.1.4 Summary of physiological correlates of neuronal activity

A neuron's ability to generate synaptic and action potentials depends on the existence of an electrochemical gradient across the cell membrane, arising from differences in the concentrations of various ions (most notably Na^+ and K^+) on the intra- and extracellular sides. In the long term, this ionic charge separation is maintained by an active transport mechanism (via the Na,K-ATPase pump), which requires turnover of ATP to transfer cations across the cell membrane [294]. The propagation of both postsynaptic potentials and action potentials is mediated by the opening of ion channels in the cell membrane. Therefore, both ion-pumping burden and ATP requirements of a cell are modulated by synaptic activity as well as the rate of neuronal firing. Increases in the functional activity thus result in heightened energy requirements and a greater demand for glucose and oxygen, the basic substrates of efficient ATP production in the brain. This surge in demand (manifested through increased CMR_{O_2} and CMR_{glu}) is met through increased tissue perfusion (CBF) [108, 113, 302] by dilation of the arterioles feeding a tissue domain. This induces an increase in the capillary blood velocity [306] and possibly some expansion of capillaries. Thereby, the venous blood pressure is elevated, resulting in the stress relaxation of smooth muscles in venous walls and thus a delayed passive swelling of veins and a rise in the total cerebral blood volume.

2.2 Blood oxygenation level dependent (BOLD) fMRI

2.2.1 Blood oxygen saturation

The supply of oxygen to tissues, via blood, is the principal function of red blood cells, which occupy 37-54% [325] of blood volume in an adult. (Most of the remaining blood volume is made up of plasma, an aqueous solution of proteins, glucose, amino acids, lipids,

gases and inorganic ions, with 90% of plasma composed of water [364].) Highly efficient transport of oxygen is achieved via a globular protein hemoglobin (Hb), Hb molecules comprising 90% of a dessicated red blood cell [364]. Hemoglobin consists of 4 protein sub-units (2 α and 2 β peptide chains), each surrounding a heme group. Each heme group, in turn, is composed of a porphyrin ring coordinated with a ferrous ion, Fe(II). There are 4 coordinate-covalent bonds between the central Fe(II) and the nitrogen atoms of the porphyrin ring as well as one coordinate-covalent bond between Fe(II) and a nitrogen atom of a histidine residue of a polypeptide chain. The sixth coordination site of the heme's iron ion is available for bonding with O_2.

In the deoxygenated state, the valence electron clouds surrounding the heme iron and the histidine residue of the polypeptide chain repel each other so that the porphyrin ring assumes a domed configuration and Fe(II) is pushed out of the plane of the porphyrin ring. Upon oxygen binding to the heme iron, the heme group undergoes a conformational change, the porphyrin ring adopting a planar configuration, with Fe(II) now pulled into this plane. Consequently, the histidine residue to which Fe(II) is bonded is also pulled into the plane of the porphyrin ring, which in turn causes a change in the tertiary structure of the subunit, in turn changing its interactions (*e.g.* salt bridges, hydrogen bonds, and hydrophobic interactions) with the adjacent subunits. In the end the quaternary structure of the entire hemoglobin molecule is altered so that the access and thus binding of an oxygen molecule to the second heme iron is facilitated. Such allosteric interactions between the subunits, leading to incremental strengthening of the oxygen binding, arise from the unique quaternary structure of hemoglobin. The resulting phenomenon, known as cooperative binding, is critical to the effectiveness of oxygen transport in the body. Hemoglobin thus exhibits a sigmoidal oxygen binding curve with respect to the local partial pressure of oxygen, as shown in Figure 2.8 [192].

The ratio of oxyhemoglobin concentration to the sum of deoxy- and oxyhemoglobin concentrations (*i.e.* O_2 combined with Hb as a fraction of O_2 capacity of Hb) is termed "blood oxygen saturation" or "blood oxygenation level," customarily symbolized by Y

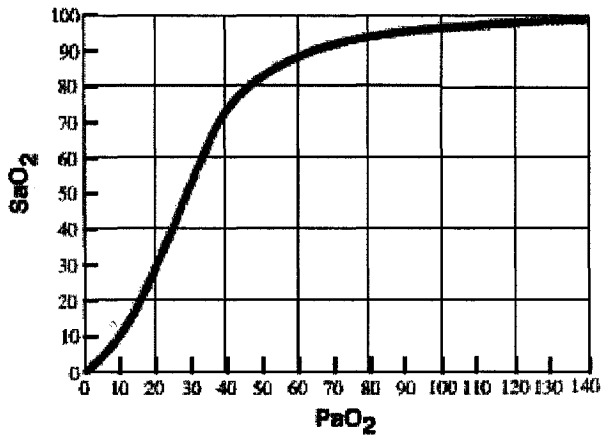

Figure 2.8: Oxyhemoglobin dissociation curve [8].

and expressed in percent. The venous blood oxygen saturation is determined by the focal parenchymal CMR_{O_2}, in combination with CBF and total hemoglobin concentration in the local vasculature as well as the arterial oxygenation level. Under baseline conditions, CMR_{O_2} and CBF are very slowly varying [260], producing an average oxygen saturation of about 98% in arterial, ~80% in capillary and ~60% in venous blood [157, 365]. Notwithstanding the temporal variations, due to the variability and complexity of vascular architecture, baseline blood oxygenation level also varies across the brain. Upon activation, changes in each of the three physiological parameters affect local blood oxygenation level. (Moreover, Y may also be influenced by any activation-induced decreases in hematocrit [22, 189, 305].) While an increase in CMR_{O_2} acts to decrease Y, the disproportionately large rise in blood flow, as discussed earlier, produces a net focal increase in blood oxygen saturation during heightened functional activity. In view of the oxygen extraction occurring predominantly at the level of capillaries, the arterial blood oxygenation level remains the same, while the capillary and venous oxygenations rise by ~6% and ~12%, respectively, following a typical functional activation [365].

2.2.2 Biophysics and modeling of BOLD fMRI signal

In addition to the conformational changes in hemoglobin's structure, magnetic properties of the heme iron of a hemoglobin molecule also change following oxygenation [270]. Specifically, the deoxygenated heme iron ion is in the high-spin ferrous state. Its four unpaired electrons aligned parallel to the magnetic field, the deoxygenated heme Fe(II) is paramagnetic (*i.e.* has a small positive magnetic susceptibility, $\chi > 0$) [50, 60]. Upon binding with oxygen, however, the iron ion changes to low-spin state. In the absence of unpaired electrons, the net magnetic dipole moment is determined by the effect of the magnetic field on the orbital motions of the electrons. The oxygenated heme Fe(II) is thus diamagnetic, exhibiting a very small, yet negative magnetic susceptibility [50, 60]. Overall, the magnetic susceptibility of blood changes linearly with its oxygen saturation [366].

Due to the compartmentalization of deoxygenated hemoglobin iron atoms to erythrocytes and the diamagnetic nature of parenchyma (the magnetic susceptibility of tissue being $\sim$-9 ppm [336]), there is a small (typically $<$1 ppm [336]) bulk magnetic susceptibility (BMS) difference between the erythrocytic cytoplasm and plasma (which is diamagnetic) as well as between blood on the whole and tissue. (Notably, under physiological conditions, venous blood is still diamagnetic on the whole [336].) The latter difference is demonstrated in the middle panel of Figure 2.9, showing a cartoon profile of the magnetic field offsets (w.r.t. the static magnetic field) inside and outside of the venules containing partly deoxygenated blood (average offset being on the order of few μT [336]).

Furthermore, these BMS differences change with alterations in blood oxygen saturation and hence, following focal changes in functional activity. Upon an increase in local neuronal activity, the blood oxygenation level rises (*i.e.*, assuming normal conditions, the fraction of deoxygenated heme iron atoms decreases), so that the erythrocytic susceptibility drops and hence the BMS differences just described decrease. In other words, the magnetic field profile across a vascularized tissue element becomes more homogeneous, as illustrated in the bottom panel of Fig. 2.9 for the same venular network, now filled with blood of higher oxygen saturation.

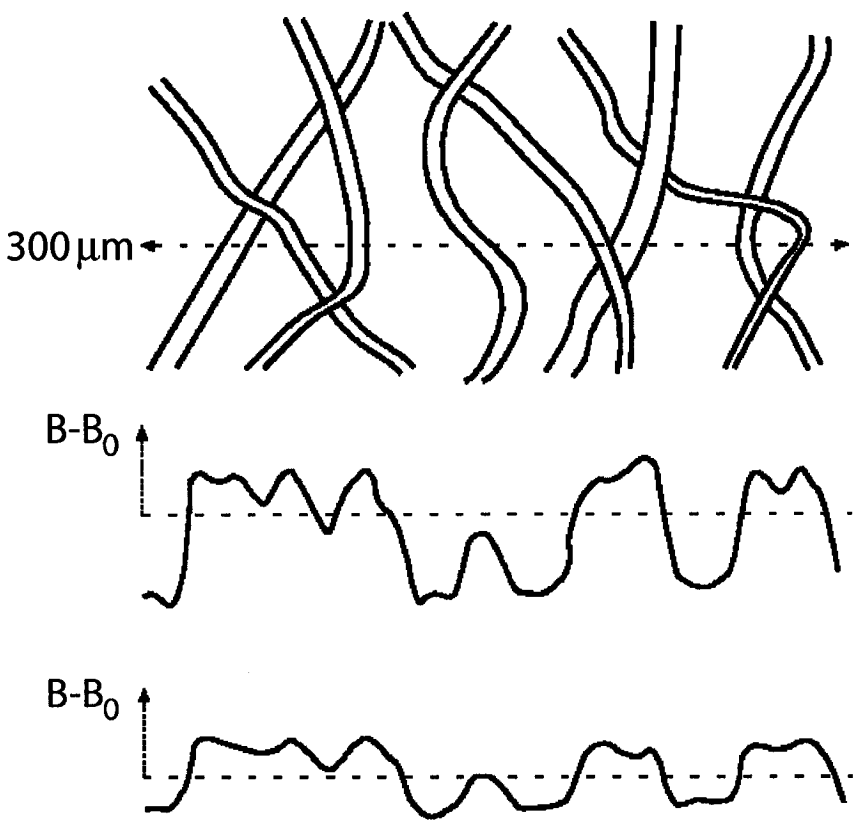

Figure 2.9: A schematic of a venular network (top) and the corresponding magnetic field profile, along the dotted line, when the venular blood is largely deoxygenated (middle) or oxygenated (bottom). [71].

The signal measured in a typical BOLD fMRI study reflects a non-equilibrium value of coherent transverse water magnetization, generated by RF excitation. In particular, the timing parameters of BOLD fMRI experiments are chosen to produce a weighting of the signal that emphasizes the activation-induced changes in the time constant of the roughly exponential decay of spin phase coherence in the plane orthogonal to the direction of the external static magnetic field. Such activation-induced differences in the apparent transverse relaxation rate (R_2^*) arise from the changes in the magnetic flux density (B) experienced by a spin ensemble under investigation following focal functional activation. The more homogeneous magnetic field profile during focal functional activation (w.r.t. resting conditions, as illustrated in Fig. 2.9) corresponds to a narrower distribution of B values; therefore less variability in the precessional frequencies (f) of the individual proton spins (f being directly proportional to B, in line with the Larmor equation) and hence slower overall dispersion of the phase coherence within the ensemble. In other words, a higher BOLD fMRI signal will be measured at activation, relative to baseline, as a result of the slower decay (smaller R_2^*) produced by the increased homogeneity in the focal miscroscopic magnetic field profile, arising from the activation-induced increase in the capillary and venous blood oxygenation levels.

This inhomogeneous BMS effect arises for both intra- and extravascular spins and is influenced by the transcytolemmal and transendotheilial magnetic susceptibility differences, respectively, the geometry of the vascular compartment (its shape, size, and wall curvature), and the overall geometry of the set-up (the vessel's orientation relative to B_0 and its proximity to other compartments of differing magnetic susceptibility) [336]. An additional, homogeneous BMS effect arises for the proton spins inside the blood vessels and is affected by the transcytolemmal $\Delta\chi$, the shape of the vascular compartment and its orientation with respect to B_0.

Both intravascular and extravascular spins are undergoing constant anisotropic diffusion, with the water exchange time being short (0.6 to 10 ms [42, 46, 130, 131, 148, 246, 346, 379]) across the erythrocytic membrane, but long (~0.65 s [201]) across the capillary

wall. (The intravascular spins are, of course, also flowing, at speeds varying both across the vascular tree and with the local metabolic demands, as described earlier.) This diffusion has a moderating effect on the BOLD signal [50]. As the spins move around randomly, they experience a range of field offsets, so that over a given interval between the RF excitation and readout (a.k.a. echo time) the histories of field offsets experienced by the proton spins comprising the spin ensemble become more concordant. In other words, the rate of phase dispersion is reduced and a higher signal is measured. The longer the effective diffusion distance in the direction of the maximal spatial field gradient caused by the perturbers (RBCs in the case of intravascular spins; and vessels in the case of extravascular spins), the more pronounced this effect. Previously described factors will dictate the field inhomogeneities profile, while the nature and speed of diffusion (*i.e.*, the shape of the diffusion displacement distribution and mean diffusivity) will be determined by the tissue microstructure. (A simple corollary is that the diffusion will be more effective in reducing the extravascular BOLD effect surrounding capillaries as opposed to venules due to a much smaller capillary radius, the spatial extent of the inhomogeneities varying in proportion to the perturber's radius [50].)

Despite the small blood volume fraction of the brain (~4% on average [50]), the stronger intravascular relative to extravascular BOLD effect described above results in a very significant intravascular contribution to the total BOLD response, especially at 1.5 T, with about 70% of the BOLD response being eliminated through strong flow-weighting gradients [33]. (The decreased intravascular contribution at higher fields results from a rapid rise in the absolute transverse relaxation rate of blood with increasing field strength [50].) In view of the subtleties of the BMS effect in combination with the complexities of the vascular tree architecture, a detailed mathematical description of the BOLD phenomenon is exceedingly complex: so much so that analytical approaches have almost entirely given way to numerical methods [336]. Following numerous other investigators, we have employed empirical techniques to study the BOLD fMRI mechanism in the present project.

This empirical approach to BOLD mechanism analysis typically involves only the extravascular BOLD signal modeling [49, 77, 155, 158, 163, 191], though largely analogous expressions may be written for the intravascular BOLD response. In the deoxyhemoglobin dilution model [155], for instance, the transverse relaxation rate of tissue is assumed to follow linear dependence on venous blood volume and supra-linear dependence on venous deoxyhemoglobin concentration [155]. (In turn, a quadratic dependence of intravascular R_2^* on deoxyhemoglobin concentration is expected [130, 347, 378].) The constant of proportionality is a sample- and field strength-dependent lump constant; the exponent of the supralinear (but subquadratic) dependence reflects the average blood volume within the sample [155]. Given an exponential decay of transverse magnetization, the activation-induced BOLD signal change is then related to the activation-induced change in R_2^*. For small change in R_2^*, BOLD response is further expressed as a function of echo time, the forementioned proportionality constant, and the baseline and activation values of venous CBV and venous dHb concentration [155]. Invoking the previously described relationship between blood flow and volume, as well as the coupling between blood flow and oxygen consumption, BOLD response may also be expressed as a function of CBF and CMR_{O_2} values at baseline and activation [155].

Clearly, validation of such top level BOLD models requires independent measures of the underlying physiological parameters, namely blood flow, oxygen consumption and venous blood volume. In view of the existence of non-invasive MR techniques for the measurement of CBF and CMR_{O_2} (elaborated upon in Chapter 6), the first three studies of this thesis focus on the development of a non-invasive method for cerebral blood volume measurement.

2.3 Cerebral blood volume measurements

An ideal method for measurement of cerebral blood volume in vivo in humans would be accurate, precise, reproducible, non-invasive, inexpensive, robust to a wide range of hemody-

namic perturbations and easily integrated into clinical protocols. At the same time, it would afford high temporal and spatial resolution and provide high functional specificity [256]. In practice, methods for blood volume measurements provide various trade-offs between these characteristics, as dictated by their primary applications. Indeed, the long-standing motivation for measuring cerebral blood volume is the assessment of the cerebrovascular reserve (CVR), typically performed via a vasodilatory challenge involving an increase in the inspired CO_2 levels [214] or an administration of acetazolomide [358]. A markedly decreased response is customarily interpreted as an indication of an already vasodilated vasculature (CBV increasing in the autoregulatory phase immediately following a drop in cerebral perfusion pressure (CPP), resulting from an arterial obstruction) and used to assess which, if any, surgical procedure is indicated (*e.g.*, revascularization through carotid endarterectomy, arterial hypertension management; antiedema therapy, or a neuroprotective trial) [17].

In stroke, monitoring of CBV (in combination with CBF and CMR_{O_2}, or, OEF, if available) is crucial for identification of the ischemic core, the penumbra and the regions of reperfused tissue [17, 78, 236]. Following a drop in CPP, a progressive change in the coupling between flow and volume occurs distal to the arterial obstruction [74, 309, 334], with an elevated compensatory CBV taken as an indicator of viability of hypoperfused tissue [249]. Furthermore, measurement of blood volume is critical to distinguishing a vasogenic or cytotoxic edema from elevated CBV with vasoparalysis in cases of increased intracranial pressure [249]. Blood volume measurements have also been employed in carcinomas, to evaluate tumor grade [9, 299] and assess response to treatment [10, 269]. The quantification of CBV is also of interest in these conditions for tracking of angiogenesis, or the generation of capillaries from preexisting blood vessels [89]. In epilepsy, relative CBV maps have been employed to localize the ictal and interictal epileptogenic foci and study tissue damage [97, 280, 362, 380]. Cerebral blood volume has been evaluated in the study of vascular and metabolic impairments in patients with Alzheimer's disease and vascular

dementia [254]. In neuropharmacological MRI, CBV measurements have been used in the study of the location and temporal evolution of the hemodynamic response to drugs [57].

Predictably, given such a wide range of applications, numerous methods have been developed to provide quantitative measurements of blood volume. Over a decade prior to the advent of fMRI, positron emission tomography has been used to provide quantitative maps of cerebral blood volume, first using $C^{11}O$ inhalation and, thereafter, the shorter half-lived $C^{15}O$ administration [136, 281, 377]. (Carbon monoxide, containing the radioactively labeled oxygen, binds to hemoglobin molecules in red blood cells and thus serves as an intravascular tracer to quantify blood volume [281].) More recently developed methods have allowed estimates of arterial blood volume via PET [170, 263] and have employed simplified bolus strategies, allowing more flexible and versatile paradigms [263]. While many important findings on blood volume distribution under physiological and various pathological conditions have been and are still made using PET [169, 210, 236, 239, 254, 277], these methods provide limited spatial and temporal resolution, are expensive, invasive, and often unavailable. Moreover, with respect to brain function applications, the paradigm design is restricted, both in terms of the acquisition time (typical $C^{15}O$ study requiring 10 minutes of continuous tracer inhalation [244]) and repeatability, in view of radiation exposure regulations. Notwithstanding, PET studies allow measurements of various hemodynamic and metabolic parameters - CBV, CBF, CMR_{O_2}, OEF, CMR_{glu}- as well as a variety of neurotransmission parameters [244]. PET has largely superseded single photon emission computed tomography (SPECT) techniques [305], following the development of short half-lived tracers and models for generation of quantitative parametric images [244]. Despite their lower spatial and temporal resolution and decreased sensitivity [244], SPECT methods for measuring CBV (using *e.g.* 99mTc-labeled RBCs) are still occasionally employed [226, 304, 357] due to their wider availability.

Cerebral blood volume is frequently evaluated via dynamic computed tomography (D-CT) by administering an intravenous bolus injection of an iodinated contrast material and applying the standard indicator dilution analysis to the data on the first pass of the contrast

agent through the cerebral circulation [14, 15, 30, 105, 141, 152, 219, 252, 253, 259, 343]. However, the accuracy of this technique and some of its methodological aspects (*e.g.*, the selection of the arterial input vessels and venous function region of interest [187]) are still under investigation [152]. Alternatively, following the central volume principle, CBV may be estimated as a product of ^{133}Xe inhalation CT CBF measurement and dynamic CT mean transit time estimate [249, 313]. Clearly, these techniques raise issues surrounding patient discomfort and safety risks from radiation exposure [256] in addition to partial volume effect issues in generation of quantitative maps [243].

On the other hand, most of the existing MR data on CBV comes from contrast enhanced MRI (ceMRI) studies. Indeed, the first human fMRI brain maps, obtained by Belliveau *et al.* in 1991 [20], were of CBV changes accompanying visual stimulation. The passage of a bolus of gadolinium-DTPA (Gd-DTPA, an intravascular MR contrast agent) was rapidly imaged using T_2^*-weighted acquisitions [20, 298]. The effect of Gd-DTPA is to produce microscopic magnetic field inhomogeneities, thus enhancing the rate of spin-spin relaxation. As before, the analysis relies on the application of the indicator dilution theory to establish the relationship between the contrast agent and CBV in addition to the observed linear dependence of the tissue transverse relaxation rate on the contrast agent concentration [20, 21]. Specifically, as the contrast agent passes through the brain, a signal attenuation directly proportional to the concentration of the contrast agent is observed. Integrating the area under the concentration time curve provides a measure of CBV. By repeating this experiment in baseline and activation conditions and subtracting the calculated CBV images, a functional activation map can be produced. The major shortcomings of the method, however, are poor temporal resolution and limited number of functional measurements that can be performed, due to the administration of the contrast agent.

Unlike dynamic bolus methods, steady-state techniques require a contrast agent with a long intravascular half-life (*e.g.* ultra small superparamagnetic particles) which alleviates the requirement for a bolus injection and affords continuous monitoring of CBV changes. One such agent is MION (monocrystalline iron oxide nanocolloid), which has been used in

anaesthetized rats to provide a five-fold increase in SNR over BOLD contrast at 2 T [235] and in awake, behaving macaques, resulting in a three-fold increase in sensitivity over BOLD at 3 T [211]. While MION concentrations used in these experiments are considerably higher than those approved for humans, initial testing of stable blood-pool contrast agents in humans has begun [308]. This approach provides high SNR and temporal resolution, though, as with Gd-DTPA bolus methods, toxicity issues limit the number and frequency of studies that can be performed on an individual.

Overall, the ceMRI methods are still costly and restrict the paradigm design [93, 289]. (Absolute CBV measurement also remains difficult since it requires reliable quantification of the arterial input function [93, 289].) Due to their limited temporal resolution and repeatability, they are ill-suited for BOLD mechanism investigations. Notably, while the BOLD response is affected by changes in the venous blood volume, as discussed earlier, the data obtained in all of these studies reflect total cerebral blood volume changes.

More recently, noninvasive imaging of cerebral blood volume in humans has been done using diffuse optical tomography (DOT) [28, 29, 88, 109, 345], with focal CBV estimates available by near-infrared spectroscopy (NIRS) [94, 301, 372, 384]. In these methods, two or more optodes are applied to the scalp and the measured changes in nearinfrared light absorption at multiple wavelengths converted into changes of concentration in the dominant chromophores (typically using a modified Beer-Lambert law), namely oxy- and deoxyhemoglobin. (Alternatively, a much higher signal-to-noise ratio may be realized by administering a highly absorbing intravascular chromophore, such as indocyanine green [160].) Cerebral blood volume is then estimated from the total hemoglobin concentration, while assuming a value for the hemoglobin concentration in blood. Quantification, however, requires quantification of the differential pathlength factor, to account for the differences in the actual distances traveled by light at each wavelength in view of the scattering and absorption properties of tissue. Due to the heterogeneity in optical properties of tissue [58], the ensuing modeling is predictably very complex. Moreover, in the noninvasive DOT applications, the effect of the initial and final passage of light through the extracerebral

tissue must also be accounted for. Notwithstanding the partial volume and penetration effects, DOT may afford very high temporal resolution measurements of hemodynamic parameters, especially if the partial volume effect is constrained by concurrent fMRI measurements [156].

Chapter 3

Susceptibility-induced Spin-echo Signal Dephasing in Tissue

3.1 Preface

The overall goal of the methodological work undertaken in this thesis is the development of a noninvasive fMRI method for measuring venous blood volume changes. To isolate the blood signal, this method (described in Chapter 5) relies on the difference in the transverse relaxation behaviour of tissue *v.s.* deoxygenated blood with respect to refocusing interval variation. Therefore, we first investigated the dependence of spin-spin relaxation rate in tissue on the refocusing rate. In general, the transverse relaxation of tissue is affected by the refocusing interval. The range of the refocusing rates that produces a significant change in the $T_{2_{tissue}}$, however, depends on a number of tissue parameters that have been only partly described: namely, the magnitude of the microscopic field inhomogeneities, their spatial profile and the "nature and speed" of water diffusion in the tissue (*i.e.*, the shape of the diffusion displacement distribution and mean diffusivity). A complete analytical theory of susceptibility induced tissue signal dephasing in a cerebrovascular network is lacking, the authors typically calling for more elaborate models of vascular network and largely relying on simulations for partial validation [173, 193, 194]. Moreover, there is no data available

on T_2 as a function of the Carr-Purcell-Meiboom-Gill (CPMG) refocusing interval and oxygenation level. To investigate the possible dependence of tissue T_2 on the refocusing intervals of interest for our CBV quantification method, we undertook a T_2 relaxometry study of the occipital lobe in a large group of healthy young adults. The small decreases in the apparent T_2's observed (of 3.3±1.5 ms in GM and 3.0±1.5 ms in WM for τ_{180} increase from 8 to 22ms) were consistent with blood being the only source of refocusing interval dependence of apparent T_2 in grey and white matter of the occipital lobe. These empirical results established a negligible effect of the refocusing interval on the transverse relaxation time of tissue for the refocusing intervals of interest here.

Quantitative T_2 in the occipital lobe: the role of the CPMG refocusing rate

Bojana Stefanovic, John G. Sled, and G. Bruce Pike

McConnell Brain Imaging Centre, Montreal Neurological Institute,

3801 University St., McGill University, Montreal, Quebec, Canada

H3A 2B4

Journal of Magnetic Resonance Imaging, 2003; 18(3): 302-9

3.2 Abstract

Purpose: To investigate the dependence of occipital gray and white matter T_2 on the Carr-Purcell-Meiboom-Gill (CPMG) refocusing interval, thereby testing the basis of a novel fMRI method for blood volume quantification, and addressing recent questions surrounding T_2 contrast in the occipital lobe.

Materials and Methods: A CPMG sequence with 1x1x5 mm^3 resolution was used to quantify T_2 in a single axial slice at the mid-level of the occipital lobe in 23 healthy adult volunteers. Refocusing intervals of 8, 11 and 22 ms were compared. A Bayesian classifier was used to classify a 1x1x1 mm^3 T_1-weighted 3D data set into gray matter, white matter and cerebrospinal fluid, with an average 95% *a posteriori* probability used as threshold for inclusion into a tissue specific ROI.

Results: The usual T_2 contrast between the gray and white matter (*i.e.*, $T_{2GM} > T_{2WM}$) was observed, with a highly significant effect of tissue type on the estimated T_2 ($p < 10^{-5}$). The observed T_2 gradually decreased with increasing refocusing interval, for a drop of 3.3±1.5 ms in gray and 3.0±1.5 ms in white matter between the 8 and 22 ms refocusing interval acquisitions.

Conclusion: The observed T_2 shortening is consistent with the effect of the dramatic decrease in T_2 of partly deoxygenated blood on this range of refocusing rates.

Key words: T_2 relaxation; occipital lobe; refocusing rate

3.3 Introduction

The difference in the rates of transverse relaxation between various tissues represents a fundamental source of contrast in MRI. Quantification of T_2 is important for optimization of acquisition parameters, longitudinal examinations, direct comparisons between studies, and enhancement of pathological specificity. Furthermore, T_2 relaxometry has recently been used to measure hemodynamic and metabolic parameters fundamental to brain function investigations [353].

A plethora of T_2 quantification studies established slower transverse decay in the gray *vs.* white matter of healthy adult brain [36, 119, 361]. This common T_2 ordering is thought to primarily reflect the rapid decay of the myelin-associated water in combination with the preponderance of myelin sheath in the white matter [369]. However, a significant amount of regional heterogeneity within each tissue has been documented [117, 369]. Moreover, dramatic age specific variations have been reported: most notably, an inversion of the common gray-white matter T_2 contrast in the newborn, hypothesized to result from incomplete myelination [104]. A shortening of T_2 has been observed in the deep gray matter structures of the extrapyramidal system [116, 359, 382], as well as in the cerebral cortices [140, 149, 383]. While this enhanced transverse decay is very frequently postulated to arise from progressive accumulation of ferritin with age, a number of rigorous quantitative relaxometry studies showed no correlation between tissue iron concentration and T_2 across different brain regions [41, 54, 55]. In particular, having quantified T_2 via both MRI and MRS in a set of cadaveric brains, Chen *et al.* [54] performed quantitative assays for iron and ferritin of the same specimens, but found no consistent correlation between either ferritin or iron concentration and T_2 values. Recently, an inversion of T_2 contrast between gray matter (GM) and white matter (WM) in the occipital lobe of healthy adults has been reported at 1.5T at 1x1.3x2 mm^3 resolution and hypothesized to result from larger ferritin deposits in the occipital gray (*vs.* white) matter [386]. Another recent study also documented shorter T_2 in gray than in white matter of the occipital lobe at both 4 and 7T [19].

In addition to T_2 shortening, the presence of an agent of high magnetic susceptibility (such as ferritin in oligodendrocytes [174]) may give rise to a dependence of T_2 on the interval between the refocusing pulses (τ_{180}) in a Carr-Purcell-Meiboom-Gill (CPMG) experiment. Specifically, T_2 is expected to decrease with refocusing interval elongation due to increased extent to which water molecules sample the magnetically inhomogeneous environment surrounding the agent within an inter-echo interval [143]. This phenomenon has been extensively studied both in iron-rich gray matter [54, 174, 359, 382] and in blood, where partial deoxygenation leads to the production of paramagnetic deoxyhemoglobin [130, 347, 379]. Indeed, in the context of fMRI, we have developed a technique for measurement of activation-induced blood volume changes that achieves blood signal isolation at 1.5T by assuming that only the T_2 of blood (*vs.* those of tissues) changes with the refocusing interval [339]. Contrary to this assumption, albeit at higher fields, a recent study reported very pronounced occipital gray and white matter T_2 dependencies on the refocusing rate at both 4T and 7T, the estimated T_2 decreasing by 30-40% between a short (6-7 ms) and a set of long (above 10 ms) refocusing interval acquisitions [19]. While a greater decrease of the blood T_2 with refocusing interval elongation is expected at higher fields, the overall shortening of blood T_2 in combination with low tissue blood content, makes it unlikely that the blood T_2 dependence on the refocusing interval alone fully explains these findings.

In view of the reported magnitude of tissue T_2 shortening with increasing refocusing interval at 4 and 7T suggesting an extra-vascular source of this dependency, we set out to explore this phenomenon at 1.5T. We thus investigate the refocusing rate dependence of T_2 in gray and white matter in the occipital lobe of a large group of healthy human volunteers at 1.5T. We have hypothesized that the variation of the refocusing intervals in the range of interest produces no effect on the extravascular brain tissue T_2. The measurements were obtained using a 32-echo CPMG sequence with three different refocusing intervals, namely 8, 11, and 22 ms. Due to the potential of voxels partially filled by cerebrospinal fluid (CSF) to confound the tissue T_2 relaxometry, we sought to define regions of interest

(ROIs) with minimal partial volume contamination. At the same time, we aimed to include as many voxels in our ROIs as possible, maximizing both SNR and the robustness of our T_2 estimates. Therefore, we used a manually-trained Bayesian classifier, supplied with high resolution (1x1x1 mm^3) T_1-weighted volumes, to identify gray, white and CSF regions having a small likelihood of contamination by other tissues. Non-linear least squares minimization was performed to fit the echoes to a mono-exponential model. We present the estimated T_2 values in each region of interest along with the ROI description. The results of a multi-factor analysis of variance of the T_2 estimates as well as direct comparisons are provided, illustrating the effects of tissue type and refocusing interval on T_2 values, while controlling for inter-subject variability.

3.4 Materials and methods

3.4.1 Measurements

The experimental protocol consisted of a 3D RF-spoiled T_1-weighted gradient echo (1x1x1 mm^3) sequence for tissue classification purposes; followed by three versions of a 32-echo single-slice CPMG (1x1x5 mm^3) sequence for T_2 quantification. The single slice for the CPMG acquisitions was located axially, at the mid-line of the occipital lobe and positioned to exactly span five 1-mm slices of the T_1-weighted volumetric acquisition. The head of the subject was immobilized using a vacuum bag and all acquisitions were obtained in a single session to minimize the probability of misregistration. Twenty three healthy adult volunteers were studied (10 females and 13 males), with an age distribution of 29±5 years (mean±standard deviation), and a range of 24 to 42 years. In view of a very slow increase in occipital cortex iron levels following the first two decades of life [140], this age range ensured minimal differences between iron levels in the occipital cortices of the subjects. Informed consent was obtained prior to each session in accordance with institutional guidelines. The first four subjects were examined on a Siemens 1.5T Magnetom Vision system, and the remaining 19 on a Siemens 1.5T Magnetom Sonata system (following

upgrade). The high resolution gradient echo sequence employed a 256 mm field of view, 256x256 matrix, TR/TE of 22/10 ms, and non-selective 30° RF-spoiled excitation. The CPMG sequence is illustrated schematically in Figure 3.1. The inter-echo intervals in the three CPMG sequence versions were 8, 11, and 22 ms, this choice being driven by the range employed in our cerebral blood volume (CBV) methodology, optimal sensitivity to potential ferritin-induced T_2 shortening (based on the T_2 relaxometry data from the extrapyramidal system [359]) in combination with hardware limitations, power deposition considerations, gradient performance, spatial encoding, and SNR requirements [99]. Indeed, the sequence parameters were optimized to provide robust T_2 measurements with the shortest achievable inter-echo intervals, given the primary motivation of investigating the T_2 dependence on a range of refocusing intervals of interest for our CBV methodology. The three CPMG variants were played out in randomized order. To minimize the confounding effects of imperfect slice profiles and sensitivity to B_1 inhomogeneities, non-selective composite 90°_x-180°_y-90°_x pulses were used for refocusing. To suppress stimulated echoes, flow effects, and signal contributions outside of the slice of interest, the refocusing pulses were flanked by spoiling gradients, alternating in sign and decreasing in magnitude [282]. The total diffusion weighting due to these gradients was small, with b-value less than 1 s/mm^2 in the last echo. Identical crusher gradient amplitudes and timing with respect to the refocusing pulses in all three versions of the CPMG sequence ensured identical b-values. A 256 mm field of view, with a 256x256 matrix, and a 2 s repetition time were used in each CPMG acquisition. The total scan time per subject was approximately 40 minutes.

3.4.2 Data Analysis

Masks of the occipital lobe were manually defined on the volumetric T_1-weighted data. Tissue segmentation within these masks was then performed using a parametric Bayesian approach that assumes the voxel intensities are drawn from a mixed population of three statistical distributions (GM, WM, and CSF) [25]. Only voxel intensities from the T_1-weighted 1 mm isotropic resolution scans were considered in the segmentation process.

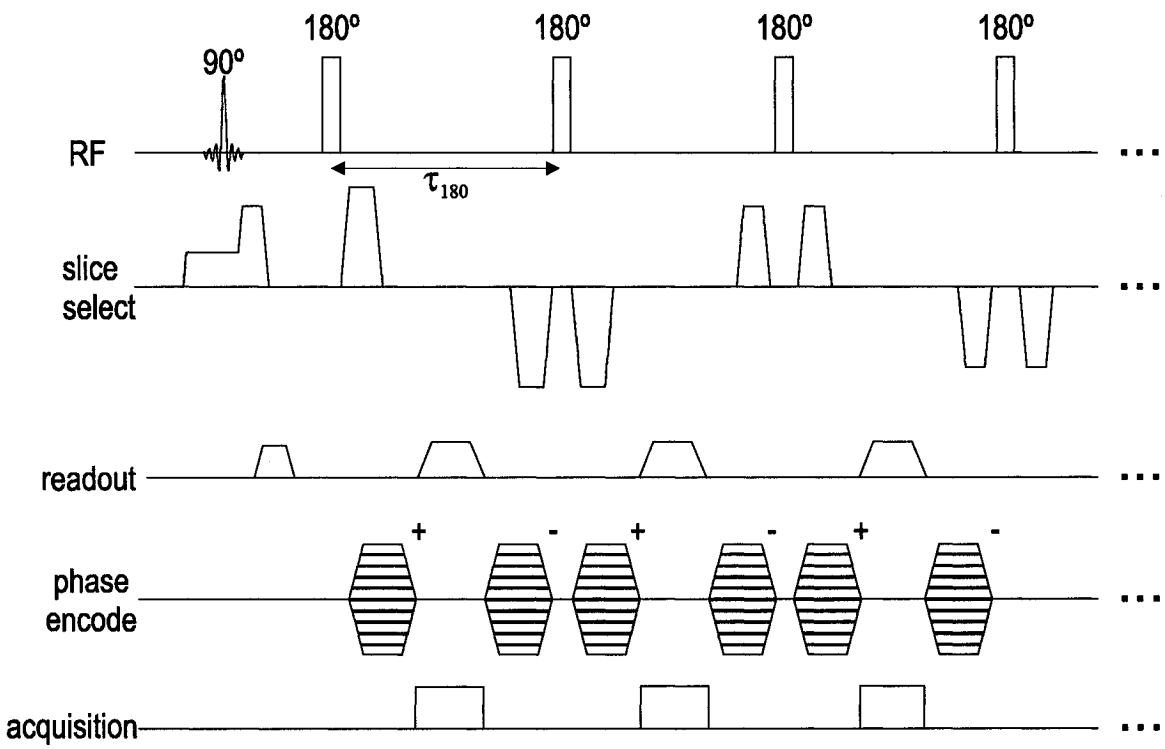

Figure 3.1: Schematic of the CPMG sequence used for T_2 quantification. The spoiler gradients in the slice select direction alternate in sign and decrease in magnitude with each echo. The refocusing interval (τ_{180}) is respectively set to 8, 11, and 22 ms in the three CPMG sequence variants employed.

All class conditional probability distributions were assumed to be Gaussian; and the class prior probabilities were equal for the three classes. For each subject, three sets of 100 manually selected voxels belonging to each of GM, WM, or CSF were used to compute mean intensity and standard deviation for each class. This training data set allowed an explicit calculation of the parametric estimates of the *a posteriori* probabilities as scaled likelihoods of voxel intensity value given that the voxel belongs to a class, in accordance with the Bayes's theorem [85].

The Bayes classification produced three normalized *a posteriori* probability maps, respectively specifying the probabilities of voxels belonging to GM, WM, or CSF. From each of these probability maps, we selected the 5 1-mm axial slices contained in the 5-mm transverse slice of the CPMG acquisitions. Thereafter, a careful visual inspection of multi-modal overlaid data, on a subject-by-subject basis, was performed to check for intra-scan movement and ensure the spatial alignment of the 3D T_1-weighted scan and the CPMG data set. The threshold for inclusion of a $1\text{x}1\text{x}5mm^3$ voxel from the CPMG slice into a tissue specific ROI was a 95% average of normalized *a posteriori* probabilities of the five corresponding $1\text{x}1\text{x}1mm^3$ voxels from the 3D T_1-weighted data. The resulting gray matter ROI, for example, was composed only of voxels having at least 95% probability of being gray matter, with average normalized *a posteriori* probability of CSF of 0.6±0.4%. This analysis approach thus afforded rigorous minimization of partial volume errors while maximizing the SNR and hence T_2 estimation accuracy.

For each echo time, the CPMG data from all voxels within each ROI were averaged. The first two echoes of the 8-ms acquisition, the first echo of the 11-ms acquisition; as well as the last 9 echoes of the 11-ms acquisition and the last 20 echoes of the 22-ms acquisition were discarded to ensure comparable temporal sampling windows (namely, 24-256 ms, 22-253 ms, and 22-264 ms for 8-, 11-, and 22-ms acquisitions, respectively). Non-linear least squares minimization (via the Nelder-Mead Simplex method) was used for fitting of the resulting decay curves to a mono-exponential decay model. Multi-exponential fitting was explored, but afforded no additional information and was hence discontinued. This result

was expected, since the sampling time window, from ~20 to ~260 ms, used for fitting resulted in a much reduced myelin water contribution [369] and was insufficient for robust detection of the CSF peak (with the CSF contribution expected to be minimal, anyhow, given the stringent ROI selection procedure). Three-factor analysis of variance was used to investigate the effects of tissue type, refocusing interval, and inter-subject variability on the estimated transverse relaxation time constant. Tukey's procedure was employed *post hoc* to identify significant pairwise differences.

3.5 Results

Sample regions of interest produced by Bayesian classification of a subject's T_1 data, followed by averaging and thresholding at the 95% level (as described above) are shown in Figure 3.2a and 3.2b. The corresponding plots (Figure 3.2c and 3.2d) show the logarithm of averaged ROI signal intensities from the last 30 echoes of the 8 ms echo spacing acquisition and the logarithm of the corresponding fitted values in the same subject.

The T_2 data for the 23 subjects are listed and summarized in Tables 3.1 and 3.2, for white and gray matter, respectively. The average normalized Bayesian *a posteriori* probabilities for the white matter ROIs were 99±0, 1.0±0.4 and 0.0±0.0% for WM, GM, and CSF, respectively. For the gray matter ROIs, the average *a posteriori* probabilities were 99±1, 0.7±0.4 and 0.6±0.4% for GM, WM, and CSF, respectively. The errors in T_2 estimates quoted in the Tables are based on 95% confidence intervals derived from the residual errors in the mono-exponential fits. Finally, the mean T_2 data across subjects, summarized in the last rows of Tables 3.1 and 3.2, are plotted in Figure 3.3, showing the average estimated gray and white matter T_2 values, respectively, from 8-, 11- and 22-ms refocusing interval acquisitions.

To investigate the effects of inter-subject variability, tissue type and refocusing rate, a three-factor ANOVA was performed. At $\alpha = 0.05$, the inter-subject variability in estimated T_2 was not significant (p=0.97). In contrast, there was a very strong effect of the tissue

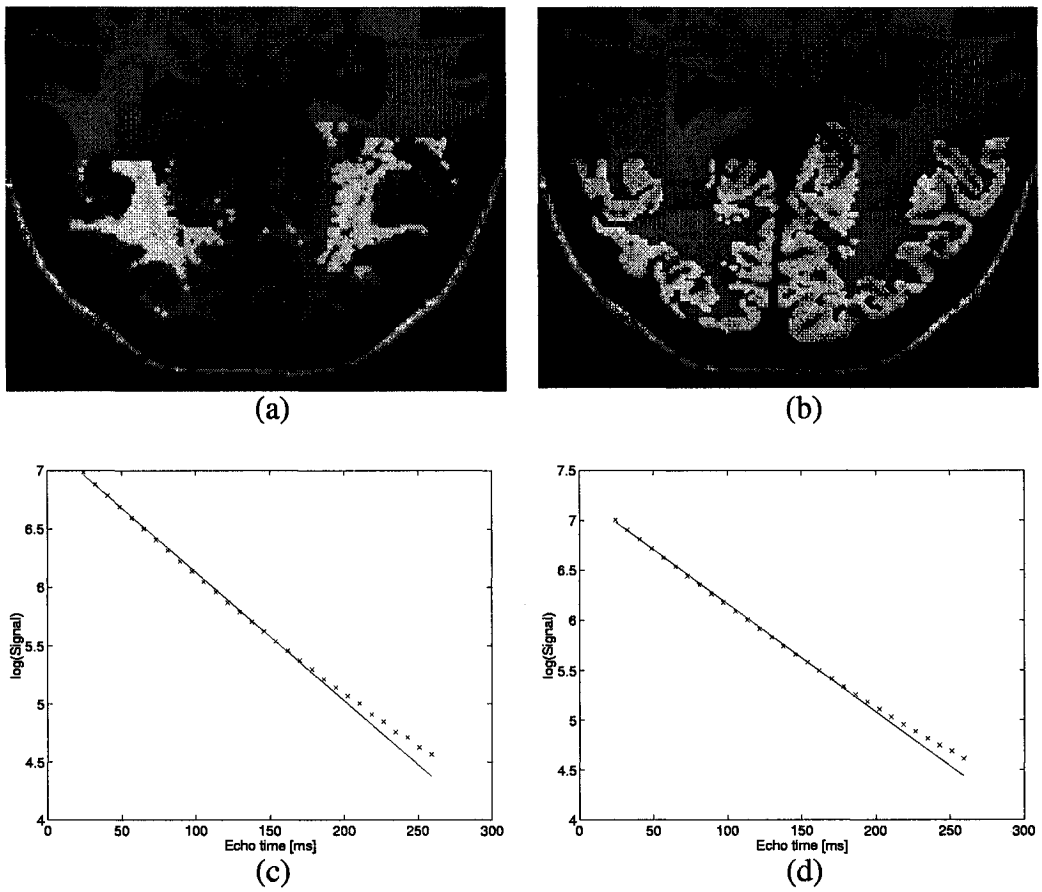

Figure 3.2: The WM (a) and GM (b) regions of interest in the occipital lobe of a subject obtained by Bayesian classification followed by thresholding of the average estimated *a posteriori* probabilities at the 95% level. The logarithm of averaged ROI signal intensities at each echo time (shown as 'x') and the logarithm of the corresponding nonlinear fits (shown as solid line) for the 8-ms refocusing interval acquisition for WM (c) and GM (d), respectively. Note the leveling off in the last few echoes due to Rician distributed noise.

Table 3.1: The occipital WM T_2 estimates from CPMG acquisitions with varied refocusing intervals.

WM ROI (cc)	T_{2WM}^{8} (ms)	T_{2WM}^{11} (ms)	T_{2WM}^{22} (ms)
4.2	89±1	87±2	85±3
5.4	85±1	84±2	83±2
4.0	88±2	87±2	86±3
7.4	80±1	78±1	80±2
4.9	91±2	90±2	87±4
5.4	90±1	88±1	85±3
4.4	91±2	89±3	86±4
7.4	87±2	85±2	84±3
7.2	89±2	87±2	86±3
4.2	82±2	83±2	81±2
7.0	97±2	96±3	92±4
3.6	93±3	94±3	91±5
4.2	86±1	83±2	81±2
6.1	85±1	84±1	82±2
3.8	83±1	83±1	81±2
2.4	83±2	83±2	80±2
6.4	81±1	81±1	80±2
1.5	86±2	86±2	84±3
4.9	92±2	91±2	88±3
3.5	91±2	89±2	86±3
5.0	83±1	82±2	83±2
4.4	92±2	91±2	87±4
3.4	83±2	84±2	82±2
4.8±1.6	87±4	86±4	84±3

Table 3.2: The occipital GM T_2 estimates from CPMG acquisitions with varied refocusing intervals.

GM ROI (cc)	T_{2GM}^{8} (ms)	T_{2GM}^{11} (ms)	T_{2GM}^{22} (ms)
8.2	94±2	92±2	89±4
7.8	89±2	88±2	87±3
6.4	91±2	89±2	89±4
6.7	87±2	85±2	87±3
6.4	94±2	92±2	89±3
7.8	100±2	99±3	95±4
4.7	94±2	93±3	89±4
8.0	91±2	91±2	89±3
5.4	89±2	88±2	87±3
2.9	87±2	88±2	85±3
3.6	102±3	100±3	97±4
6.6	94±2	95±3	92±4
5.1	95±2	94±3	91±3
8.3	94±2	92±2	90±3
8.7	95±2	93±3	92±4
4.0	91±2	90±2	87±3
6.7	86±2	87±2	86±2
3.2	87±2	88±2	85±3
6.3	98±2	96±3	93±4
7.8	92±1	91±2	88±3
6.0	89±2	87±2	87±3
5.8	95±2	92±2	90±4
4.4	94±3	93±3	90±5
6.1±1.7	93±4	91±4	89±3

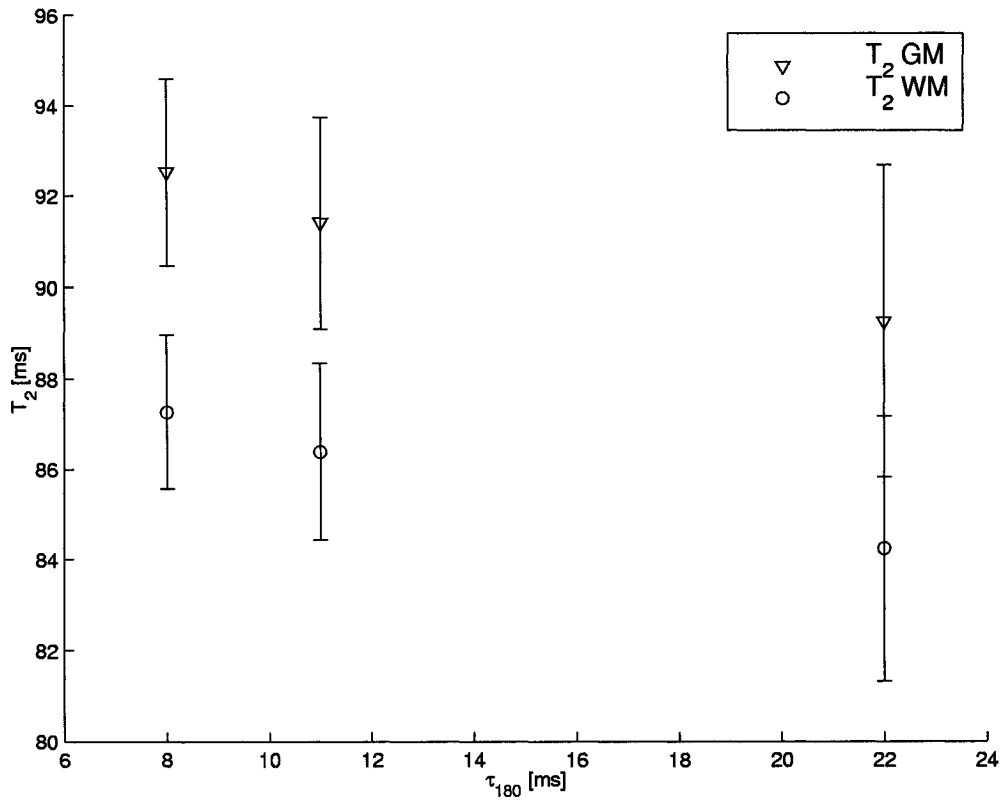

Figure 3.3: Average occipital GM and WM T_2 estimates from CPMG acquisitions with 8, 11 and 22 ms refocusing intervals. The error bars represent the standard deviation of T_2 estimates across subjects.

type on the T_2 estimate ($p < 10^{-5}$). The effect of the refocusing interval was also statistically significant ($p < 10^{-3}$), with the post-hoc Tukey's analysis revealing a significantly different T_2 estimate from 22-ms acquisition as opposed to those from either 11- or 8-ms acquisitions. Specifically, the estimated T_2 decreased by an average of 3.3±1.5 ms in gray and 3.0±1.5 ms in white matter between the 8- and 22-ms acquisitions. In both tissues, the T_2 dropped by 2.1±1.4 ms between the 11- and 22-ms acquisitions.

Within subject two-factor analysis of variance, considering the effects of tissue type and refocusing rate, detected no statistically significant effect of the refocusing interval in any subject (p>0.34). In 14 out of 23 subjects, the effect of tissue type was statistically

significant at $\alpha = 0.05$ ($p<0.024$), with the gray matter T_2 being longer than that of white matter for all subjects at all refocusing intervals.

3.6 Discussion

The first finding of this study is the preservation of the common gray-white matter T_2 contrast in the occipital lobe of healthy adults. The results show a consistently longer T_2 in gray than in white matter. While the estimated T_2 values certainly lie in the expected range for the respective tissues observed in numerous other studies [32, 35, 119, 202, 369], a different choice of region of interest and/or averaging among a variety of areas, combined with the known heterogeneity of T_2 values hinders direct comparisons. The same contrast was also reported for an occipital lobe ROI at 3T by Wansapura *et al.* [361]. However, at 1.5T and with 1x1.3x2 mm^3 resolution, Zhou *et al.* observed an inversion of T_2 contrast between gray and white matter [386]. Bartha *et al.*, also reported shorter GM than WM T_2 values in the occipital lobe at both 4 and 7T [19].

It is important to consider the methodological differences between these two studies [19, 386] and the present work. Both studies had significantly different echo sampling than that used here: 6 echoes, 25 ms apart in the former [386]; and 4 echoes for the short refocusing interval (6-7 ms) or 3 echoes for the long refocusing interval (10-26 ms) in the latter [19]. The issues arising from few echoes in combination with mono-exponential analysis have been well documented [370]. Most notably, spurious statistically significant differences, of 5%-15%, were reported in estimated T_2 values depending on the number of echoes, echo spacing and the timing of the first echo [370]. On the other hand, a 32-echo 10-ms inter-echo interval CPMG sequence constitutes the *de facto* standard for in vivo T_2 relaxometry [282, 369, 370]. Regarding the difference in the extent of the sampling, we have reanalyzed our data with sampling windows aligned to those of Zhou *et al.* (thus truncating the data at 152 ms for the 8-ms refocusing data set, and at 154 ms for the 11- and 22-ms refocusing interval data sets). Notably, while the absolute values of all T_2 estimates

decreased, all the conclusions still held: *i.e.*, the usual T_2 tissue contrast was preserved for all subjects, at all refocusing intervals; there was a small but statistically significant effect of the refocusing interval, whereby the estimated T_2 decreased by an average 3±1 ms in GM and 3±2 ms in WM between 8- and 22-ms acquisitions.

We also noted that the subject age distribution in the study by Zhou *et al.* (32±8 yrs) was different than the one in our investigation (29±5 yrs), whereas the actual age ranges were quite similar (22 to 44 yrs in the former and 24 to 42 yrs in the latter). Although a very slow ferritin accumulation for either age range is expected in the occipital cortex based on the literature [140], we explored the effect of age on our T_2 estimates (both in terms of tissue T_2 contrast and the T_2 dependency on the refocusing interval) *post hoc* by looking at differences between the groups composed of the four youngest (24±0 yrs) and the four oldest (38±4 yrs) subjects in this study. We found a preserved, statistically significant ($p < 10^{-5}$) ordering of tissue T_2s (*i.e.*, $T_{2GM} > T_{2WM}$); a trend of decreasing T_2 with increasing refocusing interval ($p > 0.4$); and no statistically significant effect of age ($p > 0.7$).

The difference in the ROI definition may also account for the differences in the findings. Specifically, the volumes of interest (for both GM and WM) in the study by Zhou *et al.* were much smaller than the ones used here. The authors employed two occipital ROIs of 1-4 voxels each, *i.e.*, a volume of 0.0052-0.021 cc per tissue in each of the 8 volunteers, with GM ROIs apparently located in the area of the primary visual cortex. The regions of interest considered in this study, on the other hand, have an average (across the 23 subjects) volume of 4.8±1.6 cc and 6.1±1.7 cc in WM and GM, respectively (*cf.* Tables 3.1 and 3.2) and come from across the occipital lobe section enclosed in the axial CPMG slice. We thus expect our GM T_2 values to reflect an average across the occipital cortex and note that the variability in the occipital cortex cytoarchitecture, particularly the high density of granular cells and high degree of myelination of the primary visual cortex may underlie the different T_2 GM *vs.* T_2 WM ordering.

Finally, while the T_2 data in the study by Zhou *et al.* was of higher resolution (1x1.3x2 mm^3) than that obtained with our CPMG acquisition (1x1x5 mm^3), it is important to note that the careful analysis was undertaken to ensure minimal partial volume errors in our ROIs. The segmentation was thus based on Bayesian classification of a 1x1x1 mm^3 3D T_1-weighted acquisition. A very careful selection of the training data - namely, the selection of voxels within a very limited occipital VOI with separate training sets for each subject - is expected to provide very good Bayesian segmentation [25]. Indeed, a validation of the parametric Bayesian classification showed robust performance with respect to noise, RF inhomogeneities and slice thickness [197]. Moreover, minimal intensity nonuniformities arise in our, very limited, occipital VOI. We thus expect excellent performance of the Bayesian segmentation and, based on visual inspection, very good spatial coincidence between the high resolution 3D T_1-weighted scan and the 2D CPMG data, thereby ensuring a very low CSF contamination of our ROIs (with average normalized *a posteriori* probability of CSF in the GM ROI of 0.6±0.4%) and a correspondingly high sensitivity to the intrinsic contrast between GM and WM (that might otherwise be obscured by partial voluming between GM and CSF). Overall, given our substantial subject pool, large number of echoes, extensive ROIs and very low partial voluming, we feel confident of the presented occipital T_2 estimates. We also note that our experimental results agree well with the preliminary theoretical predictions of tissue T_2 (of 92 ms for T_{2GM} and 87 ms for T_{2WM}) presented by Zhou *et al.* and based on the water content, myelin water fraction and blood volume of gray and white matter, respectively [386].

The second major finding of the present work is the statistically significant effect, after controlling for inter-subject variability, of the CPMG refocusing interval on the occipital tissue T_2 estimates at 1.5T. The small decrease, of 3±2 %, in the T_2 values of either tissue can be accounted for by the effect of blood. (It is worth noting that the very small blood content of either tissue as well as proximity of T_2 of blood to those of tissue at 1.5T precludes bi-exponential modeling of in vivo data: the mono-exponential decay model is thus applied to ROIs composed of both tissue and blood.) Specifically, the confinemen-

t of paramagnetic deoxyhemoglobin (dHb) to red blood cells gives rise to two vascular compartments with distinct magnetic properties: the intra-erythrocytic and the plasmatic. The exchange of water spins between these two environments (with exchange time of 6 to 8 ms [40, 67]) causes a Larmor frequency shift which, in turn, results in enhancement of the blood R_2 [46]. Following Luz and Meiboom's model of chemical exchange between multiple sites at different frequencies [225] to describe this dependency, the R_2 of blood (R_{2b}) is given by [379]:

$$R_{2b} = R_{2_0} + Hct(1-Hct)(\Delta\omega)^2\tau_{ex}(1-\frac{2\tau_{ex}}{\tau_{180}}\tanh\frac{\tau_{180}}{2\tau_{ex}}), \tag{3.1}$$

where R_{2_0} is the intrinsic R_2 of blood; Hct is the hematocrit; τ_{ex} is the average exchange time; and τ_{180} is the refocusing interval. The frequency shift resulting from the different susceptibilities of the two compartments, $\Delta\omega$, depends on the level of blood oxygenation [379]:

$$\Delta\omega = \eta(1-\frac{Y}{100})\omega_0, \tag{3.2}$$

where ω_0 is the Larmor frequency; η is a dimensionless constant determined by the shape and spacing of dHb-containing erythrocytes as well as the susceptibility of dHb; and Y is the blood percent oxygenation. Parametrizing these equations with physiological values from the literature [353], the T_2 of venous blood (having oxygen saturation of ~60% [353]) decreases by ~ 45% between the 8- and 22-ms refocusing interval acquisitions, in accordance with the published values from in vitro experiments [379]. Thus, even with the small blood content of the tissue (~6% for GM and ~4% for WM [353]), a change in the observed T_2 is expected. Assuming a slow exchange across the capillary wall, the normalized signal from a voxel composed of either white or gray matter and blood is:

$$\frac{S}{S_0} = x_t e^{-R_{2t}TE} + x_b e^{-R_{2b}TE}, \tag{3.3}$$

where x_t and x_b are tissue and blood water volume fractions, respectively. Furthermore, the blood component is composed of arteriolar, capillary and venous contributions, with respective volume fractions and oxygen saturation levels set to literature values [353]. Fitting the signal values predicted by this bi-exponential equation to the mono-exponential decay model, the T_2 estimate decreases by 3 ms in gray and 2 ms in white matter between the 8- and 22-ms refocusing interval acquisitions, in excellent agreement with our observed in vivo drop of 3.3±1.5 ms in gray and 3.0±1.5 ms in white matter. The presence of paramagnetic deoxyhemoglobin attenuates the extra-vascular signal as well, due to diffusion of tissue spins in the local magnetic field gradients surrounding the partially deoxygenated blood vessels. However, the extravascular effect of deoxyhemoglobin is minimized [353] by the employment of the train of refocusing pulses in the CPMG acquisitions used here.

On the other hand, there are potential extravascular sources of tissue T_2 dependence on the refocusing interval. Notably, the heterogeneously distributed ferritin, with its antiferromagnetic core [43], is expected to induce local magnetic field perturbations, thereby shortening the T_2. Indeed, pronounced T_2 decreases have been observed in the extrapyramidal system in a number of brain iron studies [116, 359, 382]. However, the importance of the ferritin's relaxivity effect relative to other in vivo transverse relaxation mechanisms remains disputed [54, 55]. Finally, the occipital cortex has a low non-heme iron content (an average 4.55±0.67 mg of iron per 100g of fresh weight [140]) compared to that of the extrapyramidal system (with a mean of 15.36±4.86 mg of iron/100g fresh weight [140]).

In spite of an expected increase in ferritin's relaxivity at higher fields, it is questionable whether ferritin accumulation alone can account for the dramatic (30-40%) refocusing interval dependent variation of occipital tissue T_2 estimates, observed by Bartha *et al.* at 4 and 7T, between the short (τ_{180} <10 ms) and long (τ_{180} >10 ms) refocusing interval acquisitions [19]. In particular, they reported strong refocusing rate dependence of occipital WM T_2 despite the extremely low concentration of ferritin in the occipital WM [83, 151]; as well as similar WM and GM T_2 drops despite a large difference in the tissues' ferritin contents. Both of these propound a source of magnetic inhomogeneities other than ferritin. Irrespec-

tive of the origin of the observed relaxation enhancement, however, the degree of the T_2 shortening and the range of refocusing intervals over which it occurs depend on the nature of the underlying transverse relaxation enhancement mechanism as well as the strength of the external magnetic field. Hence, due to the lack of definitive knowledge about the underlying mechanism(s), an extrapolation of the 4 and 7T data to 1.5T is not available. While the limited T_2 shortening with increasing refocusing interval observed here at 1.5T most likely arises from the changes in the T_2 of the partly deoxygenated blood in the regions of interest, we cannot rule out more pronounced occipital tissue T_2 shortening at higher fields, possibly due to a combination of relaxation mechanisms. Nevertheless, the small observed magnitude of the T_2 shortening at 1.5T for the refocusing intervals of interest provides support for our CBV methodology [339]. Specifically, the isolation of the blood signal in that method, allowing for quantification of CBV changes accompanying functional activation, is achieved through variation of the refocusing interval, at constant echo time, in neighboring measurements, thus relying on the uniqueness of T_{2blood} dependency on the refocusing interval in the range of refocusing intervals explored here.

In conclusion, we have observed the common gray-white matter T_2 contrast (*i.e.*, $T_{2GM} > T_{2WM}$) in the occipital lobe and a small, but a statistically significant ($p < 10^{-3}$) decrease of tissue transverse relaxation time with increasing CPMG refocusing interval (3.3±1.5 ms drop in T_2 of gray and 3.0±1.5 ms drop in T_2 of white matter for refocusing interval elongation from 8 to 22 ms). The estimated T_2 values lie in the expected range based on the earlier T_2 relaxometry studies and are in close agreement with theoretical GM and WM tissue T_2 calculated from estimates of the water content, myelin water fraction and blood volume of each tissue [386]. The observed shortening of the estimated T_2 can be accounted for by the known effect of refocusing interval on the T_2 of partly deoxygenated blood. The results also lend support to the hypothesis of a refocusing rate independent T_2 of extravascular brain tissue at 1.5T.

Chapter 4

Susceptibility-induced Spin-echo Signal Dephasing in Blood

4.1 Preface

Having established that the refocusing interval variation employed in our venous CBV measurement technique has a negligible effect on the tissue relaxation time, we proceeded to carefully quantify the effect of the refocusing interval (τ_{180}) on the spin-spin relaxation time in blood, at various levels of oxygen saturation (Y). The findings of in vitro human whole blood relaxometry studies described in the following manuscript allow estimation of venous CBV changes via our novel technique and are also of interest for signal modeling in spin-echo blood oxygenation level dependent (BOLD) experiments. A range of blood oxygenation levels, pertinent to normal functional physiology, was achieved through an exercise paradigm. The multi-echo data for T_2 estimation was collected in vitro, while probing an extensive range of refocusing intervals. Ensemble fitting of the entire set of T_2 estimates was performed using both the fast chemical exchange model and the model of diffusion in weak magnetic field inhomogeneities. A large reduction in the residual sum-of-squares was found in the diffusion modeling (when compared to fast exchange modeling) and led to its selection in describing the spin-spin relaxation rate enhancement by deoxyhe-

moglobin compartmentalization. The longitudinal relaxation rate decreased linearly with Y and increased with hematocrit. These parametrizations of the dependence of transverse and longitudinal relaxation rates on oxygen saturation allow the prediction of the blood signal at any oxygenation level and refocusing interval. Furthermore, the results support the application of the recent diffusion model in describing the deoxyhemoglobin-induced blood transverse relaxation rate enhancement at 1.5 T. Finally, the data collected allow selection of the sequence parameters in our CBV method to minimize the sensitivity of the recorded activation-induced signal change on the intravascular spin-echo BOLD effect and hence provide robust estimation of venous CBV changes accompanying normal functional activation.

Human Whole Blood Relaxometry at 1.5 T: Assessment of Diffusion and Exchange Models

Bojana Stefanovic and G. Bruce Pike

McConnell Brain Imaging Centre, Montreal Neurological Institute,

3801 University St., McGill University, Montreal, Quebec, Canada H3A 2B4

Magnetic Resonance in Medicine, 2004; 52(4): 716-23

4.2 Abstract

Human whole blood relaxometry experiments were performed to allow the prediction of blood signal changes with blood oxygen saturation (Y) and refocusing interval (τ_{180}), of particular interest in spin-echo blood oxygenation level dependent experiments and in a recently proposed non-invasive fMRI method for cerebral blood volume measurements. Ensemble fitting of the entire set of T_2 estimates, obtained over an extensive range of Y and τ_{180} values, was performed using both the fast chemical exchange model and the model of diffusion in weak magnetic field inhomogeneities. Diffusion modeling resulted in a large reduction in the residual sum-of-squares when compared to fast exchange modeling. The longitudinal relaxation rate decreased linearly with Y and increased with hematocrit.The results support the application of the recent diffusion model in describing the deoxyhemoglobin-induced blood transverse relaxation rate enhancement at 1.5 T.

Key words: blood, relaxation, diffusion, exchange

4.3 Introduction

Due to the paramagnetic nature of deoxyhemoglobin (dHb), partial deoxygenation of blood leads to the establishment of microscopic magnetic field gradients and, consequently, an enhanced rate of spin dephasing - an effect widely exploited in the blood oxygenation level dependent (BOLD) fMRI. Both extra- and intravascular compartments contribute to the total BOLD response, with the relatively long exchange time of water across the capillary wall (on the order of 0.5 s [306]) rendering the two compartments separate on the time scale of an MRI experiment. Despite a very small cerebral blood volume fraction, the increase in the T_2 of blood with oxygenation is so much greater than that of tissue that almost all of the spin echo BOLD response at 1.5 T originates in the vasculature [353]. This strong dependency of blood T_2 on the degree of oxygen saturation (Y) has been used for venous blood oximetry [379] as well as oxygen extraction measurements [130]. The associated sensitivity of blood T_2 on the refocusing interval [346] has recently been exploited to isolate the blood signal and afford non-invasive measurements of cerebral blood volume (CBV) changes [339]. Accurate quantification of the physiological parameters of interest via these techniques is contingent on the robust quantitative prediction of spin-spin relaxation in blood over the physiological range of Y and for the refocusing intervals employed in a given acquisition. In this study, we set out to characterize the effect of blood oxygenation and refocusing interval on T_2 of human whole blood, in the context of normal brain physiology.

Although numerous studies have been performed on red blood cell suspensions, whole bovine blood, and human whole blood to investigate the dependence of blood T_2 on various physiological parameters, a complete understanding of the underlying mechanism is still lacking. Invariably, the studies reported a pronounced shortening of T_2 with deoxygenation and refocusing interval elongation. Qualitatively, this phenomenon clearly results from sequestration of paramagnetic deoxyhemoglobin (dHb) in red blood cells of partly deoxygenated blood [346]. Quantitatively, however, much controversy remains, with various models having been proposed to explain the effect, including fast chemical exchange of water protons between the two compartments [46, 130, 131, 379] and/or diffusion in the

intra- and/or extracellular magnetic gradients [42, 120, 346]. In view of the complexity of diffusion modeling [246], a number of researchers in the past have used the exchange model as a convenient analytical approximation [42]. Recently, Jensen and Chandra described a detailed theoretical model of the transverse relaxation rate enhancement in the presence of weak microscopic field inhomogeneities [172] and applied it to the published Carr-Purcell-Meiboom-Gill (CPMG) data for isotonic and hypotonic red blood cell suspensions using canine as well as human blood. Brooks *et al.*, in turn, showed the equivalence between the chemical exchange model and the diffusion model in the short- and long-echo limits [44]. Nevertheless, a considerable variability in the parameter estimates has been reported in practice across different studies employing either exchange or diffusion models [130, 246].

In addition to consideration of spin-spin relaxation, an effect of deoxygenation on the spin-lattice relaxation time is also of interest, since the typical repetition time in an fMRI experiment (chosen to maximize temporal resolution) makes the resulting BOLD signal sensitive to T_1 variations. Moreover, a dependency of T_1 on Y (and hence the extent of T_1 variation across the vasculature) would affect perfusion quantification via arterial spin labeling [324], techniques dependent on blood signal isolationas well as the aforementioned technique for CBV quantification [339]. In contrast to a number of earlier studies [18, 335, 346], a recent report [324] documented a sensitivity of T_1 in blood on hematocrit as well as oxygen saturation. The dHb-induced changes in T_1, of much smaller relative magnitude than those of transverse relaxation time, have been postulated to result from direct dipolar interactions of water protons with the paramagnetic deoxyhemoglobin [324].

To investigate the relaxation mechanisms in human whole blood, particularly as they pertain to the brain activation physiology, we tested the current models of spin-spin relaxation in blood and provided in vitro estimates of each model's parameters while spanning the fMRI relevant range of blood oxygenation levels and an extensive set of refocusing intervals. To complete the blood signal characterization, the dependence of $T_{1_{blood}}$ on Y and hematocrit was examined. Beyond providing insight into blood relaxation behavior, we strove to arrive at a robust parametrization of the best performing model, thereby enabling

precise quantification of intravascular spin-echo signal changes following brain activation and facilitating accurate measurements of the physiological parameters of interest in the acquisition strategies relying on the dHb-induced blood T_2 shortening phenomenon.

4.4 Theory

The confinement of the paramagnetic deoxyhemoglobin to red blood cells gives rise to two vascular compartments of distinct magnetic properties: the intra-erythrocytic and the plasmatic. The exact mechanism of the deoxygenation induced shortening of the T_2 of blood has been variably ascribed to the transmembrane exchange of water spins between the two environments [40, 46, 67] and/or diffusion in the local intracellular [121], extracellular [37] or combination of intra- and extracellular magnetic field gradients [120, 346].

In the exchange model, the spins experience effectively instantaneous jumps between the two compartments [46]. Following Luz and Meiboom's model of fast chemical exchange between two sites at different frequencies [225], the dependency of blood T_2 (T_{2b}) on the refocusing interval (τ_{180}) is given by:

$$\frac{1}{T_{2b}} = \frac{1}{T_{2_0}} + \gamma^2 K_0 \tau_{ex} \left(1 - \frac{2\tau_{ex}}{\tau_{180}} \tanh \frac{\tau_{180}}{2\tau_{ex}}\right), \tag{4.1}$$

where T_{2_0} is the intrinsic T_2 of blood (here indicating the limiting T_2 of blood as the refocusing interval tends to zero); γ is the gyromagnetic ratio (2.675×10^8 rad/s/T); K_0 is the variance of microscopic spatial field inhomogeneities [172]; and τ_{ex} is the average exchange time of a spin between the two compartments.

Alternatively, Jensen and Chandra have recently described the effect of weak microscopic field inhomogeneities on the spin-spin relaxation in the presence of diffusion of significant magnitude relative to the length scale of the field inhomogeneities [172]. The

dependence of blood T_2 on the refocusing interval was described as [172]:

$$\frac{1}{T_{2b}} = \frac{1}{T_{2_0}} + G_0 \frac{\gamma^2 r_c^2}{2D} F(\frac{2D\tau_{180}}{r_c^2}), \tag{4.2}$$

where G_0 is the mean squared magnitude of the field inhomogeneities; r_c is the characteristic length scale for the spatial variations of the field inhomogeneities; and D is the diffusion coefficient. The function F is given by [172]:

$$F(x) = \frac{1}{\sqrt{\pi}} \int_0^\infty \frac{e^{-y}}{\sqrt{y}} (1 - \frac{1}{xy} tanh(xy)) dy. \tag{4.3}$$

4.5 Methods

4.5.1 Blood Collection and Handling

Whole blood specimens were obtained by venipuncture from four healthy adults on two separate occasions. The blood was drawn from the superficial veins of the non-dominant forearm into 15 mm diameter, 3 mL, draw dry heparanized syringes (Becton Dickinson Vacutainer Systems, Franklin Lakes, New Jersey), with special care being taken to avoid any air bubble formation in the vacutainer. The oxygen saturation was modified in vivo via exercise. Specifically, forearm occlusion was achieved by inflation - to ~50 % above the subject's systolic pressure - of a blood pressure cuff, positioned ~4 cm superior to the olecranon process. The first sample was drawn with the arm at rest. The subject was then instructed to lift a 5 lbs hand weight repeatedly by alternating elbow flexion and extension (with the non-dominant arm) for about 4 minutes. Another two blood samples were drawn in the course of the exercise. Finally, the forearm cuff was released and the last blood sample drawn during the ensuing hyperoxymic stage. Informed consent was obtained prior to each session in accordance with institutional guidelines.

Immediately following the phlebotomy, the filled vacutainers were placed in a custom-built gear made of LEGO (The Lego Group, Billund, Denmark). They were secured in a

wooden frame, custom built to fit into the transmit/receive CP Extremity Coil (Siemens, Erlangen, Germany), with the long axes of vacutainers parallel to the applied static magnetic field. A long wooden rod connected the frame to a veristaltic pump (Manostat, New York), allowing rotation of the vacutainers about their long axes, at ~20 rpm. The pump was connected to a custom built switch, which received triggers from the scanner and provided the pump with power (hence enabling the gear rotation) only during the delay period at the end of each repetition (with the pump switched off 1 s prior to the readout). The chosen rotation frequency prevented the settling of erythrocytes, known to significantly affect the lineshape within 2-3 min [114, 241, 335], while minimizing the inertial motion of blood during readout. The rotation rate employed corresponds to an average linear velocity below 1 cm/s and is hence representative of blood flow in the microvasculature [306].

Within five minutes following the completion of the MR relaxometry measurements, the blood samples were analyzed using a Bayer 800 series blood analyzer and co-oximeter system (Bayer AG, Leverkusen, Germany). The measurements of the blood gases and oxygen status were corrected for the scanner room temperature (22°C). The co-oximetry was done on each sample to establish the content of hemoglobin and its derivatives as well as estimate the hematocrit (Hct).

4.5.2 Blood Relaxometry

Two single slice sequences were used for in vitro blood T_2 relaxometry: a T_2 prepared segmented EPI sequence [38] (2.3x2.3x5 mm^3) on the first set of blood samples, and a 32 echo CPMG sequence (2x2x5 mm^3) on the second set of blood samples. The former sequence contained a non-selective T_2-weighted preparation composed of a non-selective 90° excitation, followed by a train of hard refocusing pulses with subsequent non-selective tip-up, slice-selective excitation and segmented EPI readout. This scheme is particularly suited to the application at hand because it allows very short refocusing intervals to be probed, a critical issue in view of the time scale of the exchange/diffusion processes being investigated. The refocusing intervals employed were 2, 2.5, 3, 3.74, 4, 4.5, 5, 7, 10, 12, 14, 17, 20, 30,

and 40 ms. This sampling was motivated by a number of considerations: the expected high rate of change of T_2 blood with respect to the refocusing interval for τ_{180} below 10 ms; the comparison between the T_2 blood estimates from the T_2 prepared EPI data with those of the CPMG acquisition; and the refocusing intervals employed in our CBV technique [339]. The order of acquisitions with different refocusing intervals was randomized. To investigate the reproducibility of the blood T_2 estimates over the scanning window, at least two randomly selected refocusing intervals were probed twice in the course of a scanning session. To minimize the confounding effects of imperfect slice profiles and sensitivity to B_1 inhomogeneities, non-selective composite 90°_x-180°_y-90°_x pulses were used for refocusing, with their phases following the MLEV pattern [215]. Finally, a large spoiling gradient was applied following the slice-selective tip-up to dephase any remaining transverse magnetization. For each refocusing interval, six different T_2 preparation durations were run, providing six effective echo times, equally spaced over the sampling window, which extended from 20 to 120 ms for the shortest, and from 80 to 480 ms for the longest refocusing interval acquisitions, respectively. The acquisition parameters included a 150 by 112.5 mm FOV, with a 64x48 matrix, EPI factor of 3 (*i.e.*, 3 k-space lines per readout), readout bandwidth of 616 Hz/pixel, and a 3 s repetition time.

The purpose of the 32 echo CPMG acquisition, the *de facto* standard for T_2 relaxometry [282], was to test the robustness of the T_2 prepared segmented EPI sequence in quantifying the T_2 of blood in vitro. The inter-echo intervals in the various CPMG sequence versions were 7.5, 8, 8.5, 9, 9.5, 10, 11, 12.5, 15, 17.5, 20, 25, 30, 35, and 40 ms. The sequence parameters were optimized to provide robust T_2 measurements with the shortest achievable inter-echo intervals. The CPMG variants were played out in randomized order. As before, non-selective composite 90°_x-180°_y-90°_x pulses were used for refocusing. To suppress stimulated echoes, flow effects, and signal contributions outside of the slice of interest, the refocusing pulses were flanked by spoiling gradients, alternating in sign and decreasing in magnitude [282]. The total diffusion weighting due to these gradients was small, with $b<1$ s/mm^2 in the last echo. Identical crusher gradient amplitudes and timing

with respect to the refocusing pulses in all versions of the CPMG sequence ensured identical b values. A 256 by 128 mm field of view, with a 128x64 matrix, readout bandwidth of 315 Hz/pixel, and a 4 s repetition time were used in each CPMG acquisition.

The spin-lattice time constant of blood was quantified using a single slice Look-Locker sequence [186] with a segmented EPI readout (2.3x2.3x5 mm). A composite 90°_x-180°_y-90°_x pulse was used for non-selective inversion, with TI set to 15 ms. Each of the four 20° excitation pulses, applied every 495 ms, was followed by a readout with a TE of 10 ms. The readout bandwidth was set to 140 Hz/pixel, with 150 mm readout FOV, 75 % phase FOV, and a 4 s repetition time. The total scan time per set of four blood samples was approximately 80 minutes. In each case, the imaging slice was 5 mm thick, perpendicular to the long axes of the vacutainers, and positioned at the center of the 20 mm long blood filled compartment. Localized shimming was done on the imaging slice at the beginning of the experimental protocol. All studies were performed on a Siemens 1.5 T Magnetom Sonata system (Siemens, Erlangen, Germany).

4.5.3 Data Analysis

Non-linear least squares minimizationwas used for fitting of the multi-echo data from both T_2 prepared segmented EPI and CPMG acquisitions in the region of interest at the center of each vacutainer (hence avoiding any partial volume effect) to a mono-exponential decay model. Subsequently, the repeatability quotient [26] within each method was calculated to assess the repeatability of the measures across time, thereby testing the effects of the erythrocytic metabolism over the course of the experiment on the T_2 estimates. The limits of agreement [26] between the two methods were computed to test the validity of using the T_2 prepared segmented EPI acquisition for T_2 relaxometry. Both exchange and diffusion models were then fitted to the T_2 estimates derived from the T_2 prepared EPI data. In each case, the nonlinear model fitting was performed using a trust region method. For both model structures, two model orders were investigated: a constrained model, in which T_{2_0} was fixed across oxygen saturation levels; and an unconstrained one, in which the T_{2_0}

was allowed to vary with Y. In all cases, a single common τ_{ex} for exchange or $r_c^2/2D$ for diffusion was imposed on all T_2 *vs.* τ_{180} curves, while K_0 (in exchange) or G_0 (in diffusion) varied with Y. An F-test was employed to select the optimal model order within each model structure. The dependence of the variance of microscopic spatial field inhomogeneities on blood oxygen saturation level was also investigated. Non-linear least squares minimization was used for fitting the mono-exponential recovery model to the Look-Locker data. The dependence of the resulting T_1 estimates on Y was explored via non-linear least squares minimization and two-way analysis of variance employed to assess the effect of hematocrit on the T_1 estimates.

4.6 Results

4.6.1 T_2 Relaxometry

The mean difference across time for the repeated T_2 estimates (N=20) using the T_2 prepared multi-shot EPI acquisition was 0.1±1.7 ms (mean±standard error). The corresponding repeatability coefficient was 15 ms, so that an absolute difference in the repeated T_2 estimates of less than 15 ms is expected in 95 % of the cases given an approximately normal distribution of the differences [26]. A higher repeatability was observed for the CPMG based T_2 estimates (N=8), as expected, with mean difference across time of 0.0±1.8 ms and the repeatability coefficient of 10 ms. The limits of agreement (*i.e.* two standard deviations of the differences) for T_2 estimates (N=5) from acquisitions with matched refocusing interval, blood oxygen saturation, and hematocrit using T_2 prepared segmented EPI and 32 echo CPMG acquisitions were -7.8 ms to 2.7 ms (95 % confidence interval of -13 ms to -2.1 ms for lower; and -2.9 ms to 8.4 ms for the upper bound). The mean difference between the T_2 estimates of the two measurement techniques was -2.5 ms, with zero included in the 95 % confidence intervals on this bias.

The set of T_2 estimates (N=120), obtained from mono-exponential modeling of T_2 prepared EPI data from blood samples with matched hematocrit (51.2±0.4 %, mean±standard

Table 4.1: Exchange and diffusion model parameter estimates. The exchange time (τ_{ex}) estimate was 3.0±0.2 ms, with the intrinsic spin-spin relaxation time ($T_{2_{0,exchange}}$) and the curvature term (K_0) shown in columns 2 and 3 below. For the diffusion model, the characteristic length scale of spatial variations of field inhomogeneities (r_c) was 4.3±0.2 μm (assuming a D of 2.0 μm^2/ms); and the intrinsic spin-spin relaxation time ($T_{2_{0,diffusion}}$), 203±3 ms, with the curvature term (G_0) listed in column 4.

Y [%]	$T_{2_{0,exchange}}$ [ms]	K_0 [10^{-14} T^2]	G_0 [10^{-14} T^2]
93	198±5	0.5±0.1	0.8±0.1
87	197±5	1.4±0.2	1.9±0.2
72	200±6	2.9±0.4	3.7±0.4
66	183±7	3.7±0.5	5.5±0.6
62	184±7	4.6±0.6	6.6±0.8
48	179±9	7.3±1.0	10.1±1.2
43	169±10	9.3±1.3	13.2±1.7
42	166±10	9.4±1.3	13.6±1.8

error), was fitted using Eqs. 4.1 and 5.1. Allowing for variation of the intrinsic T_2 of blood with oxygenation level produced a better fit (at 0.01 level of significance) in the exchange but not in the diffusion modeling, as established by the F-test of the reduction in the sum of squared residuals (SSR), in going from constrained to unconstrained models within each model structure (p values of $4.7\text{x}10^{-8}$ and $1.3\text{x}10^{-2}$ for exchange and diffusion models, respectively). Furthermore, the comparison of the sum of squared residuals for the selected model order within each model structure led to the selection of the diffusion model (in view of the constrained diffusion model producing a lower SSR than the unconstrained exchange model: $SSR_{diffusion}$ ~1.85 ms^2 and $SSR_{exchange}$ ~2.49 ms^2). The estimated blood T_2 values at different levels of oxygen saturation as well as the fits of the unconstrained exchange and constrained diffusion models to these data are shown in Figure 4.1. Table 4.1 summarizes the results of this modeling.

Given the selection of the higher order model within the fast exchange formulation, the intrinsic blood spin-spin relaxation time estimates from this modeling ($T_{2_{0,exchange}}$) were re-

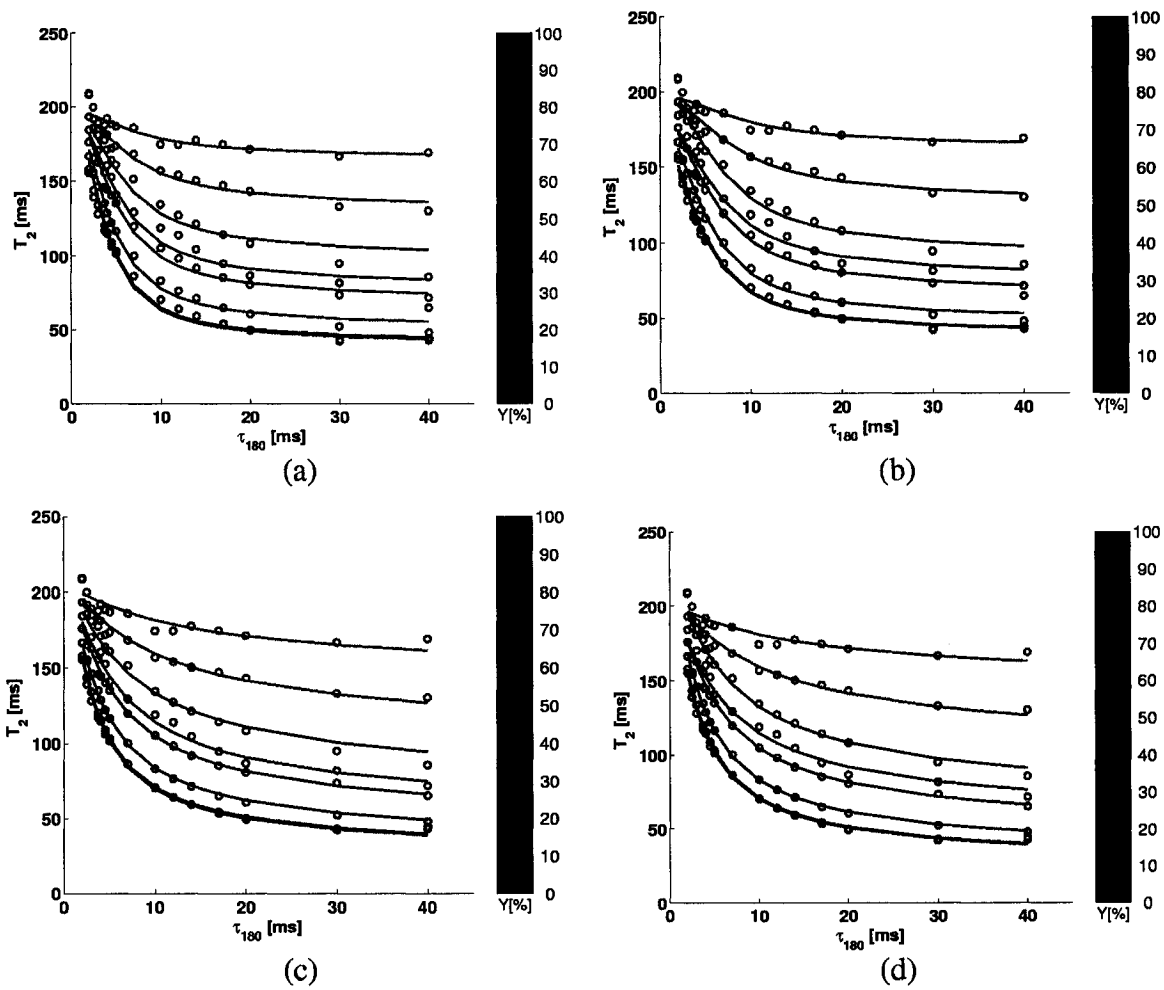

Figure 4.1: The T_2 blood estimates and the fits of the constrained (a) and unconstrained (b) exchange; and constrained (c) and unconstrained (d) diffusion models. The hematocrit of the blood samples employed was 51.2±0.4 % (mean±standard error). Note the near coincidence of the bottom two curves, as expected in view of the corresponding blood samples having very similar oxygen saturation, with Y of 42 and 43 %, respectively.

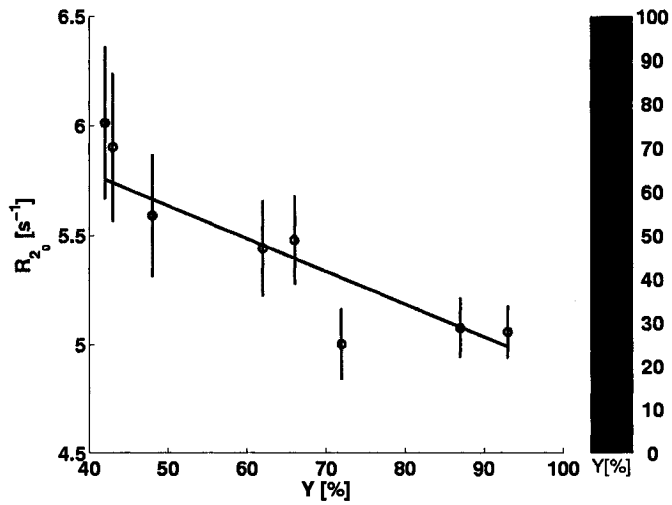

Figure 4.2: The intrinsic blood spin-spin relaxation rate estimates from fast exchange modeling fitted against oxygen saturation. The intercept estimate was 1/(157±6) ms^{-1} and the slope, dR_{2_0}/dY, (-0.0150±0.0037)x10^{-3} ms^{-1}/%. The SSR was 0.687x10^{-3} ms^2 and normalized mean squared error (NME), 2.33x10^{-3}.

gressed against the blood oxygen saturation, for comparison with literature (*cf.* Figure 4.2). A significant correlation was found: $r^2 \sim 0.83$ and $p \sim 4.8 \times 10^{-10}$. Following the expected dependencies [268], the estimates of the mean squared magnitude of the field inhomogeneities (K_0 and G_0) were fitted as quadratic functions of the blood oxygen saturation using weighted least-squares. These fits are shown in Figure 4.3, and the corresponding parameter estimates and fits quality assessment listed in Table 4.2.

Table 4.2: The fits of mean squared magnitude of the field inhomogeneities estimated from the exchange (K_0, first row) and diffusion (G_0, second row) models against $(1 - Y/100)^2$.

Slope [10^{-13} T^2]	SSR [10^{-27} T^4]	NME [10^{-15}]
3.1±0.2	1.37	1.74
4.5±0.5	1.07	2.73

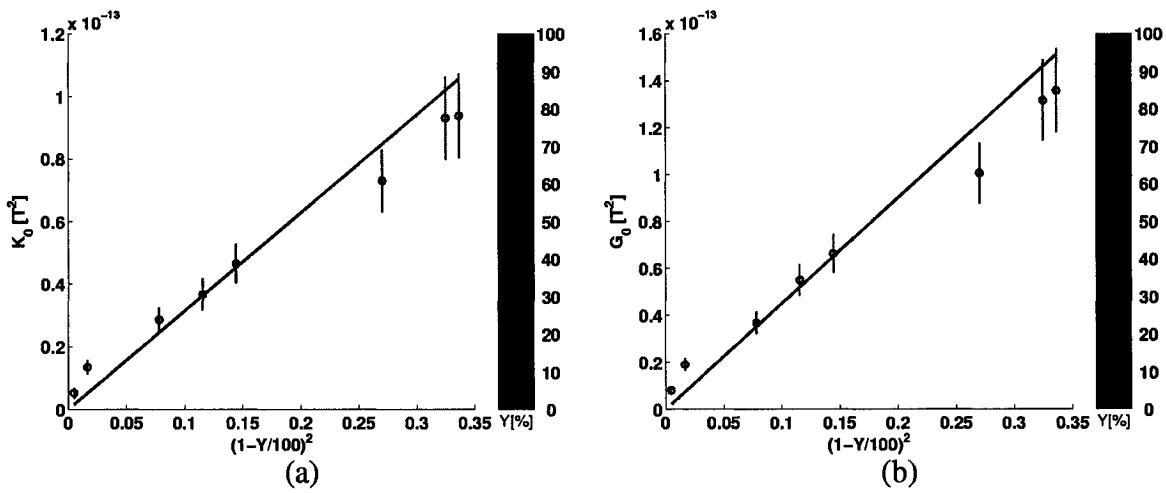

Figure 4.3: The K_0 estimates from the exchange (a) and G_0 estimates from the diffusion (b) model fitted as quadratic functions of the oxygen saturation level.

Combining the above results, the dependence of blood T_2 on the oxygen saturation, Y, and refocusing interval, τ_{180}, at 1.5 T, for the physiologically relevant hematocrit is best modeled by Eq. 5.1 with T_{2_0} of 203±3 ms, $r_c^2/2D$ of 4.60±0.42 ms and G_0 given by:

$$G_0 = (4.50 \pm 0.51) 10^{-13}\,[\mathrm{T}^2] \left(1 - \frac{Y}{100}\right)^2. \tag{4.4}$$

4.6.2 T_1 Relaxometry

The Look-Locker data, obtained from the same set of blood samples (hematocrit of 51.2±0.4 %, mean±standard error), were fitted to a mono-exponential recovery model via the non-linear least squares minimization. The dependence of the resulting T_1 estimates on Y was obtained by linear fitting of the spin-lattice relaxation rates. The results are shown in Figure 4.4. The linear dependence of R_1 on Y is thus described as:

$$\frac{1}{T_1} = \frac{1}{996 \pm 36}\,[\mathrm{ms}^{-1}] - (1.22 \pm 0.54) 10^{-6}\,[\frac{\mathrm{ms}^{-1}}{\%}]\; Y. \tag{4.5}$$

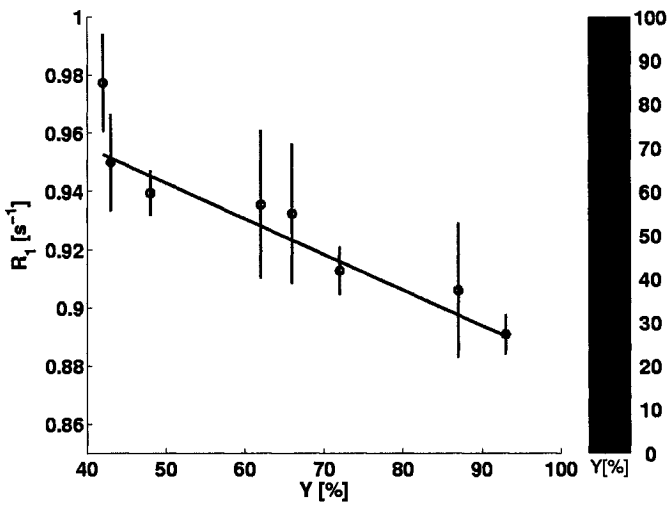

Figure 4.4: The spin-lattice relaxation time of blood fitted against oxygen saturation for the blood samples employed with Hct of 51.2±0.4 % (mean±standard error). The intercept estimate was 1/(996±36) ms^{-1}, and the slope, dR_1/dY, (-0.00122±0.00054)x10^{-3} ms^{-1}/%. The SSR was 1.05x10^{-3} ms^2 and NME, 4.22x10^{-3}.

The effect of hematocrit on T_1 was investigated by using the above fit to compare the T_1 estimates based on the samples with Hct of 51 % to those obtained for a set of blood samples with Hct of 45 %. Two-way analysis of variance reported a statistically significant effect (F = 123 and $p < 10^{-9}$) of hematocrit on the T_1 estimates when controlling for oxygen saturation, the T_1 increasing with decreasing hematocrit.

4.7 Discussion and Conclusions

The current findings strongly support the diffusion over the fast chemical exchange model for describing the dependency of the spin-spin relaxation time in blood on oxygen saturation and refocusing interval at 1.5 T. In line with earlier studies [130, 323, 379], the dependence of the transverse relaxation rate shift on blood oxygen saturation was well modeled by a quadratic function. The model order optimization led to the selection of the constrained diffusion model, with a constant intrinsic transverse relaxation time. Even when T_{2_0} was allowed to vary with Y, we found no significant correlation of the result-

ing $T_{2_{0,diffusion}}$ estimates with oxygen saturation (data not shown): the slight variation in these estimates for different Y may have derived from small differences in the hematocrit of individual blood samples, in addition to noise.

In contrast, the quality of the exchange model fit significantly improved when the intrinsic transverse relaxation time was allowed to vary with oxygen saturation, with the $T_{2_{0,exchange}}$ estimates increasing linearly with Y, as reported earlier [130]. This preference for the Y-dependent $T_{2_{0,exchange}}$ possibly attests to the limitations of using the fast exchange formulation, the "rapid" exchange limit being just achieved at 1.5 T [242]. While our exchange time estimate of 3.0±0.2 ms lies well within the literature range of 0.6 to 10 ms [42,46,130,131,148,246,346,379], the limited applicability of the fast chemical exchange model to the present circumstances hinders the exact interpretation of this parameter [120,130].

The parametrizations obtained agree very well with those estimated by Jensen and Chandra for the human whole blood data published by Brooks *et al.* Specifically, for fully deoxygenated blood, the model of uniformly magnetized, randomly distributed spheres (*i.e.*, Eq. 53 in [172], with $(4\pi\rho R^3/3)$ set to Hct) produced a G_0 estimate of $6.32\text{x}10^{-13}$ T^2, compared to $(4.50\pm0.51)\text{x}10^{-13}$ T^2 predicted here (*cf.* Eq. 5.2). The latter G_0 value corresponds to a susceptibility difference between plasma and fully deoxygenated erythrocytes of $(1.69 \pm 0.38)\text{x}10^{-7}$ cgs emu/cm^3 Oe, or $(21.2 \pm 4.8)\text{x}10^{-3}$ in SI, the corresponding literature range being $1\text{x}10^{-7}$ to $3.5\text{x}10^{-7}$ cgs emu/cm^3 Oe [40,242,335,347,353,366,378]. In view of the limitations of the random spheres model [172], this agreement is reasonable. For Brooks's data with Y of 2 % [42], Jensen's fit produced a G_0 estimate of $4.16\text{x}10^{-13}$ T^2 (scaled to 1.5 T) which is in excellent agreement with G_0 of $(4.32\pm0.49)\text{x}10^{-13}$ T^2 obtained from the Eq. 5.2 here. The characteristic length scale for the spatial variations of the field inhomogeneities of 4.3±0.2 μm obtained is also in line with Jensen's estimate of 4.2 μm [172]. For the same data set, the present exchange model parametrization predicts a K_0 of $(3.01\pm0.15)\text{x}10^{-13}$ T^2 and an exchange time of 3.0±0.2 ms, compared to

the corresponding Jensen's estimates of 2.60×10^{-13} T^2 (again scaled to 1.5 T) and 3.6 ms, respectively.

It is important to stress that while our results support the use of Jensen and Chandra's diffusion model of spin-spin relaxation enhancement in partially deoxygenated blood over fast exchange at 1.5 T, they do not rule out some contribution of chemical exchange to R_2 enhancement. Furthermore, at fields above 1.5 T, a regime change, from rapid to intermediate exchange, occurs so that the chemical exchange contribution, in contrast to the diffusion one, does not scale with B_0^2 [209, 242, 378]. As expected from the theoretical work of Brooks *et al.* [44] and clearly seen from the similarity of panels in Fig. 4.1, the chemical exchange model has the ability to reproduce the essential characteristics of the diffusion model: all that the present results demonstrate is that the diffusion model fits the data better. The quantification of the relative contributions of the two mechanisms is not achievable through the present comparison of the rather simplified descriptions of exchange and diffusion phenomena afforded by models under investigation and is beyond the scope of this study, the primary objective here being robust blood signal characterization in SE functional brain activation experiments using the best performing model.

The parametrization of the diffusion model obtained allows ready evaluation of intravascular SE signal changes upon functional activation. Specifically, for a venous blood oxygen saturation change from 65 to 75 % and with the typical spin echo BOLD TE of 100 ms, venous blood transverse relaxation time elongation from 62 to 94 ms is predicted, for a corresponding venous blood signal change of 74%. (The total intravascular SE BOLD response, however, will be determined by the relative volume contributions of the different vascular compartments and the changes in their respective oxygenation levels, dictated by activation-induced perfusion and oxygen consumption changes [353].)

With respect to spin-lattice relaxation, the observed increase of T_1 with decreasing Hct is in agreement with an earlier report [324]. This phenomenon has been attributed to a higher protein content of red blood cells with respect to plasma [175]. Moreover, the rise in T_1 with the oxygenation level, postulated to arise from direct (though limited) proton-

dHb dipolar interactions [324], agrees with the reports at 4.7 and 0.19-1.4 T [131, 324] but not with a study at 1.5 T [18]. A significantly smaller effect of Y on R_1 at 1.5 T with respect to that reported at 4.7 T in combination with limited sampling (only 2 oxygenation levels having been probed in [18]) may have precluded the detection of this dependency in the earlier 1.5 T study [18].

Two methodological notes, on temperature and hematocrit, should be made. Based on the published value of the *ex vivo* erythrocyte metabolism rate at 37°C [134], the expected drops in Y and pH over the course of the relaxometry measurements undertaken ($\sim$80 minutes) are 3$\pm$1 % and 0.08$\pm$0.03 pH units and thus within the standard error of the blood gas analyzer (as attested by repeated measurements on the same blood samples performed for repeatability assessment). The temperature of 22°C reduces the red blood cell metabolism even further, while the corresponding T_2 shortening is expected to be limited at 1.5 T over this range of temperatures ($\sim$5% decrease in T_2 from 37 to 22°C [338]). On the other hand, the spin-lattice relaxation time is known to significantly decrease with decreasing temperature, by $\sim$12 % between 37 and 22°C [223]. This study did not investigate the dependence of T_2 on the hematocrit, the application to normal brain physiology being a primary motivation for the experiment. The blood samples presently employed for spin-spin relaxometry were drawn from healthy, young adult males; the T_2 estimates derived from samples obtained from female volunteers, with Hct of 45-48%, showing the same functional dependence on Y and τ_{180} (data not shown). Over the physiological range of Hct (quoted as 30-50% [346]), a $\pm$15 % variation in T_2 has been reported [346]. The mean squared magnitude of the field inhomogeneities, G_0, in the diffusion model varies linearly with hematocrit (*c.f.* Eqn. 53 of [172].

To ensure robust prediction of blood relaxation rates, the experimental procedure included relaxation rates estimation on samples with same Hct and Y derived from different subjects, repeated refocusing interval measurements, and different acquisition strategies. A comparison of the relaxation times thus estimated with the literature values, nevertheless, requires normalization for a series of experimental conditions, as frequently emphasized.

Notably, extrapolating the Eqs. for R_2 (for long echo time) by Spees *et al.* to our Hct values yields very good agreement. Our T_2 values (*c.f.* Fig. 4.1c) are, however, somewhat higher than the ones reported by Wright *et al.* [379]. The venous T_2 range obtained here for very fast refocusing is also somewhat higher than the one reported by Stadelmann *et al.* (T_2 ~146 ms for venous blood at τ_{180} of 3 ms). On the other hand, higher corresponding T_2 values have been measured by both Golay *et al.* [130] and Silvennoinen *et al.* [324], likely reflective of these measurements having been made at higher temperature (37°) and lower hematocrit (44%).

In summary, current findings provide support for the application of the recently reported model of diffusion in weak microscopic field inhomogeneities in describing the spin-spin relaxation rate enhancement in human whole blood at 1.5 T. The parametrization of this model in combination with the described linear decrease of spin-lattice relaxation rate with blood oxygen saturation allow ready evaluation of intravascular blood signal changes for a given change in blood oxygen saturation at the selected refocusing interval. Moreover, an accurate quantification of physiological parameters of interest in methods relying on dHb-induced T_2 shortening phenomenon is afforded.

4.8 Acknowledgments

The authors would like to thank Mr. Andre Cormier for the construction of the wooden frame allowing fastening of the blood sample gear and interfacing to the veristaltic pump for the in vitro blood experiments as well as Prof. John G. Sled for helpful discussions and critical reading of this manuscript. This work was supported by the Natural Sciences and Engineering Research Council of Canada and the Canadian Institutes of Health Research.

Chapter 5

Quantitative Dynamic fMRI Measurement of CBV

5.1 Preface

In the following chapter, a new, non-invasive fMRI technique for direct quantification of venous cerebral blood volume changes is presented, providing a means to measure changes in the key hemodynamic parameter underlying the widely employed BOLD response and test the frequently assumed flow-volume relationship. Venous refocusing for volume estimation (VERVE) isolates the deoxygenated blood signal by exploiting the dependence of transverse relaxation rate in deoxygenated blood on the refocusing interval, while assuming negligible effect of the currently employed refocusing rate variation on the extravascular signal, as supported by the findings of the occipital lobe relaxometry study presented in Chapter 3. This technique was applied in a visual stimulation study of healthy human volunteers. In vitro human whole blood T_2 relaxometry data, described in Chapter 4, were used in simulations of a functional activation model to account for the intravascular BOLD effect and hence estimate the venous cerebral blood volume changes. The average venous blood volume change in the visual cortex region of interest, upon a robust visual stimulation, was estimated at 16±2%. The method allows noninvasive dynamic monitoring of

venous cerebral blood volume, thereby enabling further investigation of the physiological parameters determining the BOLD fMRI response.

Venous Refocusing for Volume Estimation: VERVE fMRI

Bojana Stefanovic and G. Bruce Pike

McConnell Brain Imaging Centre, Montreal Neurological Institute,

3801 University St., McGill University, Montreal, Quebec, Canada H3A 2B4

Magnetic Resonance in Medicine, in press

5.2 Abstract

A novel, noninvasive MRI-based method for measuring changes in venous cerebral blood volume (CBV_v) is presented. Venous refocusing for volume estimation (VERVE) exploits the dependency of the spin-spin relaxation rate of deoxygenated blood on the refocusing interval. Interleaved CPMG EPI acquisitions following a train of either tightly or sparsely spaced hard refocusing pulses (every 3.7 or 30 ms, respectively), at matched echo time were used to isolate the blood signal while minimizing the intravascular blood oxygenation level dependent (BOLD) signal contribution. The technique was employed to determine the steady-state increase in the CBV_v in the visual cortex (VC) in seven healthy adult volunteers, during flickering checkerboard photic stimulation. A functional activation model and a set of previously collected in vitro human whole blood relaxometry data were used to evaluate the intravascular BOLD effect on the VERVE signal. The average VC venous blood volume change was estimated at 16±2%. This method has the potential to provide efficient and continuous monitoring of venous cerebral blood volume, thereby enabling further exploration of the mechanism underlying BOLD signal changes upon physiological, patho-physiological and pharmacological perturbations.

Key words: venous cerebral blood volume; refocusing rate; BOLD; fMRI;

5.3 Introduction

While blood oxygenation level dependent (BOLD) functional magnetic resonance imaging (fMRI) has become a major tool for examining brain function, the understanding of the mechanism underlying BOLD signal remains incomplete. Much work has been dedicated to the investigation of neuronal correlates of the BOLD response under normal physiological conditions, at the core of establishing its validity as a marker of neuronal activation.To facilitate quantitative interpretation of BOLD signal changes, in turn, a number of research groups [49, 77, 155, 163]have proposed models of the BOLD response dependence on key metabolic and hemodynamic parameters: the cerebral metabolic rate of oxygen consumption (CMR_{O_2}), cerebral blood flow (CBF) and cerebral blood volume (CBV). Typically, no attempts were made in these studies to quantify CBV directly: instead, CBF was measured and a power-law relationship ($CBV=0.8\ CBF^{0.38}$) assumed based on the PET experiments by Grubb *et al.* involving P_aCO_2 manipulations in anesthetized rhesus monkeys [135]. While recent PET studies in humans have reproduced this dependence both during P_aCO_2 perturbations and upon visual stimulation [171],a systematic underestimation by the power-law based CBV estimates has been reported in bolus tracking fMRI studies in humans [216]. Furthermore, the assumption that the flow-volume coupling is maintained between focal functional activations and transient, mild, global P_aCO_2 perturbations, employed in the hypercapnic calibration of the BOLD response for purposes of CMR_{O_2} quantification [77, 155, 185], has recently been questioned [162]. Similarly, in pharmacological MRI studies employing vasodilatatory agents (*e.g.* ethanol, cocaine, and nicotine), concerns have been raised about the affected vascular compartment as well as the resulting CBF-CBV coupling [311]. A disrupted flow-volume coupling has been reported in a number of diseased states, *e.g.* increased volume in spite of decreased flow in oligemic and truly ischemic stages of "misery perfusion" [17]. Finally, irrespective of the steady state CBV-CBF link following physiological or pathological perturbations, an even greater uncertainty surrounds the flow-volume coupling under transient conditions in humans. Notably, a number of transient features in the BOLD response (typically the post-

stimulus undershoot, but, tentatively, the initial dip as well) have been suggested to result from differences in the temporal evolution between CBV and CBF [50, 233].

The traditional T_2^*-weighted dynamic bolus tracking methods for measuring CBV, frequently applied in humans [20, 111, 216, 248, 274], have provided limited temporal resolution and repeatability, thus being ill-suited for BOLD mechanism investigations. To address the quantification challenge with these methods, a Look Locker based T_1 relaxometry with Gd-DTPA injection has recently been used to measure total CBV increase upon visual stimulation in humans [110]. In both rodents and non-human primates, important information on CBV changes and flow-volume coupling has been afforded by experiments employing superparamagnetic nanoparticles [233, 326].Beyond issues surrounding species differences, however, the data obtained in all of these studies reflect total cerebral blood volume changes. In contrast, the BOLD response is affected by changes in the venous blood volume (CBV_v) [49]. While CBV_v change is typically equated to total CBV change, a substantial arterial contribution (~36%) to total volume change has recently been reported in perfluorocarbon studies of anesthetized rats undergoing hypercapnia [91, 208]. If representative of functional activation in humans, such pronounced arterial CBV contribution to total CBV change translates into an underestimation of the increase in the rate of oxygen consumption for a given BOLD response (CBV_v and CMR_{O_2} both attenuating the BOLD response) when equating venous CBV increases to measures of total volume increases. Dynamic and independent quantification of venous CBV changes under a variety of conditions is thus essential for our understanding of normal brain physiology, mechanism underlying transient and steady-state BOLD responses, as well as clinical applications of BOLD fMRI.

In the present study, we describe a new, noninvasive fMRI technique for direct quantification of venous cerebral blood volume changes. Venous refocusing for volume estimation (VERVE) isolates the deoxygenated blood signal by exploiting the dependence of transverse relaxation rate in deoxygenated blood on the refocusing interval. We employed this technique in a visual stimulation study of healthy adult volunteers. Independently collected,

in vitro human whole blood T_2 relaxometry data were used for functional activation modeling to account for the intravascular BOLD effect and hence estimate the venous cerebral blood volume changes. The potential of the method to provide accurate dynamic monitoring of the stimulation-induced changes in the volume of the partly deoxygenated blood is discussed.

5.4 Theory

The relatively slow exchange of water across the capillary wall ($\tau_{ex} > 0.5$ s [110])renders the extra- and intravascular compartments effectively separateover the echo time interval of a typical MRI experiment. The confinement of the paramagnetic deoxyhemoglobin (dHb) to red blood cells gives rise to two intra-vascular compartments of distinct magnetic properties: the intra-erythrocytic and the plasmatic. The transcytolemmal exchange of water spins between these two environmentsand/or diffusion in the local intra- and/or extracellular magnetic gradients result in the shortening of T_2 in blood (T_{2_b}) with decreasing blood oxygenation (Y) and refocusing interval (τ_{180}) elongation, as described in a number of in vitro and in vivo blood spin-spin relaxometry studies [130, 379].We have recently reported [340] on a series of blood relaxometry experiments, providing parametrization of the best performing model. At 1.5 T and for the physiologically relevant hematocrit, the model of diffusion in weak microscopic field inhomogeneities, described of Jensen and Chandra [172]:

$$\frac{1}{T_{2b}} = \frac{1}{T_{2_0}} + G_0 \frac{\gamma^2 r_c^2}{2D} F\left(\frac{2D\tau_{180}}{r_c^2}\right), \tag{5.1}$$

was parameterized with $r_c^2/2D$ of 4.60±0.42 ms (where r_c is the characteristic length scale for the spatial variations of the field inhomogeneities and $D \sim 2.0$ μm^2/ms, the diffusion coefficient in blood); and T_{2_0}, the intrinsic spin-spin relaxation time in blood, of 203±3 ms. With F as defined in [172], the mean squared magnitude of field inhomogeneities, G_0 (in

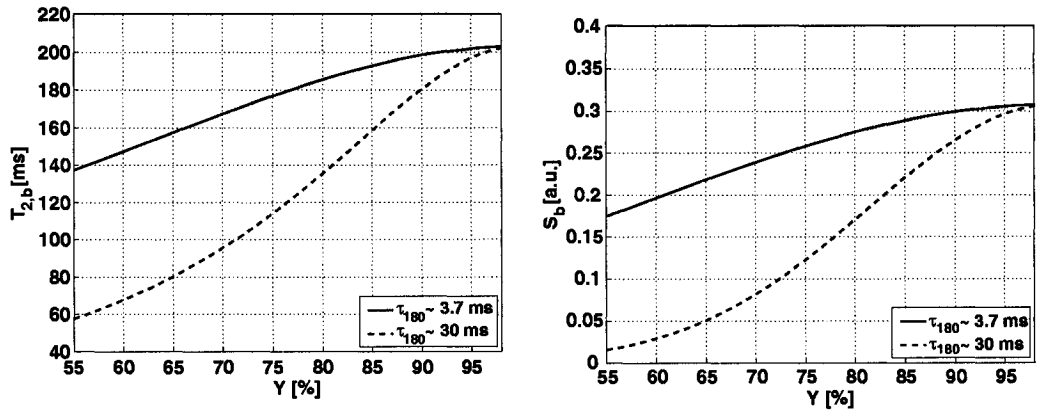

Figure 5.1: The variation in the spin-spin relaxation time of blood (T_{2_b}) (a) and normalized blood signal (S_b)at a TE of 240 ms (b) for physiologically relevant blood oxygen saturations and refocusing intervals of 3.7 and 30 ms. The plots are based on the diffusion model parametrization derived in an earlier in vitro T_2 relaxometry study of human whole blood [340].

units of T^2), followed a quadratic dependence on the blood oxygenation, Y (in percent):

$$G_0 = (4.50 \pm 0.51)10^{-13} \left(1 - \frac{Y}{100}\right)^2. \tag{5.2}$$

Briefly, no dependence of T_{2_b} on the refocusing rate is expected for fully oxygenated blood. As blood oxygenation level decreases, however, the sensitivity of T_{2_b} on τ_{180} increases, a shorter refocusing interval resulting in longer spin-spin relaxation time due to increased effectiveness of the refocusing pulses. Following the above parametrization, the variation in the transverse relaxation rate of blood at the presently selected refocusing intervals, of 3.7 and 30 ms, is displayed in Figure 5.1a for Y on the physiologically relevant range. The corresponding normalized blood signal, at a TE of 240 ms (used in our current implementation of VERVE sequence), is shown in Figure 5.1b.

In principle, the transverse relaxation time in tissue may also change with the refocusing interval. While a number of mechanisms may be involved in such a dependence, the diffusion and/or proton exchange in the presence of the anti-ferromagnetic ferritin are the

most frequently postulated sources [174]. To investigate the dependence of tissue T_2 on the refocusing interval, we undertook a T_2 relaxometry study of the occipital lobe (in view of the present visual stimulation paradigm) in a large group of healthy young adults [341]. In summary, the small decreases in the apparent T_2s (of 3.3±1.5 ms in GM and 3.0±1.5 ms in WM for τ_{180} increase from 8 to 22ms) were consistent with blood being the only significant source of refocusing interval dependence of apparent T_2 in grey and white matter of the occipital lobe. In the following, we therefore assume a negligible effect of refocusing interval - over the presently employed range and at 1.5 T - on the transverse relaxation time of tissue (T_{2_t}).

Given the slow exchange of water across the capillary wall with respect to the TE interval, the total signal, coming from a voxel composed of tissue and blood and measured in a Carr-Purcell-Meiboom-Gill (CPMG) acquisition, is given by:

$$S = S_t + S_b = f_t\, M_{0_t}\, e^{-TE/T_{2_t}(Y,\tau_{180})} + f_b\, M_{0_b} e^{-TE/T_{2_b}(Y,\tau_{180})}, \tag{5.3}$$

where f_t and f_b are tissue and blood water volume fractions; while M_{0_t} and M_{0_b} are the longitudinal magnetizations of tissue and blood immediately preceding the excitation. In light of the above discussion, only T_{2_b} is expected to change between two interleaved measurements employing the refocusing intervals on the present range (but matched echo times) at a given Y. In other words, negligible effect of the fast *v.s.* slow refocusing interval on the extravascular spin-spin relaxation time is expected. The difference between the fast (short τ_{180}) and slow (long τ_{180}) refocusing measurements (henceforth referred to as the VERVE signal) thus isolates the blood signal. Furthermore, performing these two measurements at both activation to baseline and taking the ratio of the activation and baseline signal differences results in the following relative VERVE signal:

$$rVERVE = \frac{\Delta S_{b,A}}{\Delta S_{b,B}} = \frac{f_{b,A}}{f_{b,B}}\,\frac{\Delta \hat{S}_{b,A}}{\Delta \hat{S}_{b,B}} = \frac{f_{b,A}}{f_{b,B}}\,\frac{e^{-TE/T_{2_b}(Y_A,\tau^F_{180})} - e^{-TE/T_{2_b}(Y_A,\tau^S_{180})}}{e^{-TE/T_{2_b}(Y_B,\tau^F_{180})} - e^{-TE/T_{2_b}(Y_B,\tau^S_{180})}}, \tag{5.4}$$

where $f_{b,A}$ and $f_{b,B}$ are the blood water volume fractions at activation and baseline, respectively; Y_A and Y_B are activation and baseline blood oxygen saturations; τ_{180}^F and τ_{180}^S are the refocusing intervals in the fast and slow refocusing acquisitions; $\Delta S_{b,A}$ and $\Delta S_{b,B}$ are the activation and baseline VERVE signals; and $\Delta\hat{S}_{b,A}$ and $\Delta\hat{S}_{b,B}$ are the *volume normalized* VERVE signals at activation and baseline, respectively. (Note that *relative* is used throughout the text to refer to the ratio of activation to baseline signal.) If the difference between the volume normalized blood signal in fast and slow refocusing measurements is the same at baseline and activation (i.e. if $\Delta\hat{S}_{b,A}/\Delta\hat{S}_{b,B} \sim 1$), the relative VERVE signal is equal to the activation-induced change in blood volume. Graphically, this condition translates into a Y-independent vertical separation between the fast and slow refocusing signal curves of Figure 5.1b over the Y range of interest. The degree of deviation of $\Delta\hat{S}_{b,A}/\Delta\hat{S}_{b,B}$ from unity under normal physiological conditions (henceforth referred to as the intravascular spin-echo (SE) BOLD effect), is explored in the Simulations section (the simulation set-up being described in the first subsection of the Methods and the corresponding findings outlined in the first subsection of the Results).

5.5 Methods

5.5.1 Simulations

Accurate estimation of venous CBV changes via VERVE depends on the assessment of the intravascular SE BOLD effect on the activation-induced VERVE signal changes. While prior in vitro blood relaxometry studies provided a robust parametrization of blood spin-spin relaxation time dependence on blood oxygenation levels of interest and presently employed refocusing intervals, independent dynamic quantification of venous blood oxygenation level in vivo is highly complex. Therefore, a series of simulations were performed, modeling blood oxygenation level changes following normal functional brain activation and assessing the sensitivity of the VERVE signal change to the corresponding intravascular BOLD effect. In vitro blood relaxometry data collected earlier [340] were used to predict blood

signal changes given the simulated venous oxygenation levels. Considering the intravascular compartment alone, smaller blood signal difference between fast and slow refocusing acquisitions at activation relative to baseline (*c.f.* the decreasing vertical separation between the curves of Fig. 5.1b for Y increasing from 55 to 75%) leads to underestimation of the venous blood volume changes by the blood signal change.

To investigate the IV SE BOLD effect on the total voxel signal, a model of functional activation was implemented, thereby parametrizing both voxel composition and simulating a range of blood oxygenation changes, as determined by the relative increases in flow, volume, and oxygen consumption. The voxel was assumed to comprise grey matter and blood, with the volume of water in the vasculature relative to the total water volume in the voxel (*i.e.* the blood water volume fraction) given by:

$$f_b = \frac{K_{BW}}{K_{BW} + (\frac{1}{K_B} - 1)K_{TW}}, \tag{5.5}$$

where K_{BW} and K_{TW} are blood and tissue water volume contents and K_B is the blood content of the voxel. The intravascular water was, in turn, distributed across arterial, capillary and venous compartments, with their respective fractional sizes obtained from literature [353]. The water volume in tissue made up the rest of the voxel water volume. The total water volume of the voxel was kept constant between baseline and activation, CBV increases thereby assumed to occur at the expense of tissue water volume [50].

The resting values of blood volume, flow, oxygen consumption, and total hemoglobin (Hb_t) concentration, obtained from literature, determined the oxygen extraction rate (OER) and venous blood oxygenation (Y_v) at baseline:

$$OER = \frac{CMR_{O_2}}{[Hb_t]Y_a CBF}, \text{ and} \tag{5.6}$$

$$Y_v = Y_a\ (1 - OER). \tag{5.7}$$

The arterial oxygen saturation (Y_a) was held at 98%,and the average capillary oxygenation (Y_c) estimated as [365]:

$$Y_c = Y_a - (Y_a - Y_v)\left(\frac{1}{OER} + \frac{1}{ln(1-OER)}\right). \tag{5.8}$$

The largest activation-induced change in Y (and hence maximal IV SE BOLD effect) hence occurred in the venous compartment.

The compartmental distribution of CBV changes was assigned assuming predominant arterial contribution to total vascular resistance [235]. The total blood volume change was prescribed based on the power-law relationship between CBV and CBF, with α of 0.4 [135, 171]:

$$CBV_A = CBV_B \left(\frac{CBF_A}{CBF_B}\right)^{\alpha}. \tag{5.9}$$

The total signal equation (*i.e.* Eq. 5.3 with M_0 as per Eq. 5.10) was then used to predict the measured signal in voxels composed of grey matter and blood. The aforementioned parametrization of the diffusion model was used to predict the T_2 of blood at each baseline and activation oxygenation level, for the presently employed refocusing intervals. A wide range of activation-induced blood flow increases (from 5 to 100%) was investigated, with the coupling ratio between ΔCMR_{O_2} and ΔCBF (henceforth abbreviated as Ψ, so that $\Psi \sim \Delta CMR_{O_2}$ / ΔCBF) allowed to vary from 0.4 to 1.0 [155, 163, 185]. All model parameters are listed in Table 5.1.

5.5.2 Sequence

The complete VERVE sequence is illustrated in Figure 5.2. It employs a T_1/T_2 selective 90°_x-τ-180°_y-τ-90°_x – TI preparation for SNR efficient nulling of CSF [374], with interleaved EPI readout following a train of either tightly or sparsely spaced hard refocusing pulses, at matched echo times. Hard composite 90°_x-180°_y-90°_x refocusing pulses are used to minimize the sensitivity to B_1 inhomogeneities. Stimulated echos are attenuated by MLEV phase cy-

Table 5.1: All the parameters used in the functional activation model for estimation of IV SE BOLD effect on VERVE signal changes. (The densities, ρ_{blood} and ρ_{GM}, are used to convert the blood and tissue water contents by weight to the corresponding water contents by volume.)

Variable	Description	Definition
$[Hb_t]$	total hemoglobin concentration	8.41 mmol/L [210]
K_{BW}	blood water content	0.801 g/g [178]
K_{TW}	grey matter water content	0.819 g/g [178]
ρ_b	blood density	1.060 g/cm^3
ρ_{GM}	grey matter density	1.0497 g/cm^3
K_B	blood content a GM voxel	0.056 g/g [210]
f_b	blood water volume fraction	Eq. 5.5
f_t	tissue water volume fraction	1-f_b
Y_a	arterial blood oxygenation	98 %
Y_c	capillary blood oxygenation	Eq. 5.8
Y_v	venous blood oxygenation	Eq. 5.7
CBF	cerebral blood flow	0.420 mL/(g min) [264] @ rest
ΔCBF	percent change in cerebral blood flow	5-100 %
CMR_{O_2}	rate of oxygen consumption	1.51 μmol/(g min) [264] @ rest
Ψ	oxygen consumption-to-flow ratio	0.4-1.0 [155, 163, 185]
OER	oxygen extraction rate	Eq. 5.6
CBV	cerebral blood volume	33.1μL/g [264] @ rest
ΔCBV	percent change in cerebral blood volume	100*[(CBF_A/CBF_B)$^{\alpha}$-1]
rCBV	relative cerebral blood volume	activation to baseline CBV
$fCBV_{a/c/v}$	compartmental CBV distribution	0.21/0.33/0.46 [353]
$f\Delta CBV_{a/c/v}$	compartmental ΔCBV distribution	0.27/0.11/0.62 [235]
VERVE	VERVE signal	$S(\tau^F_{180})$-$S(\tau^S_{180})$, with S as per Eq. 5.3
rVERVE	relative VERVE signal	activation to baseline VERVE: Eq. 5.4

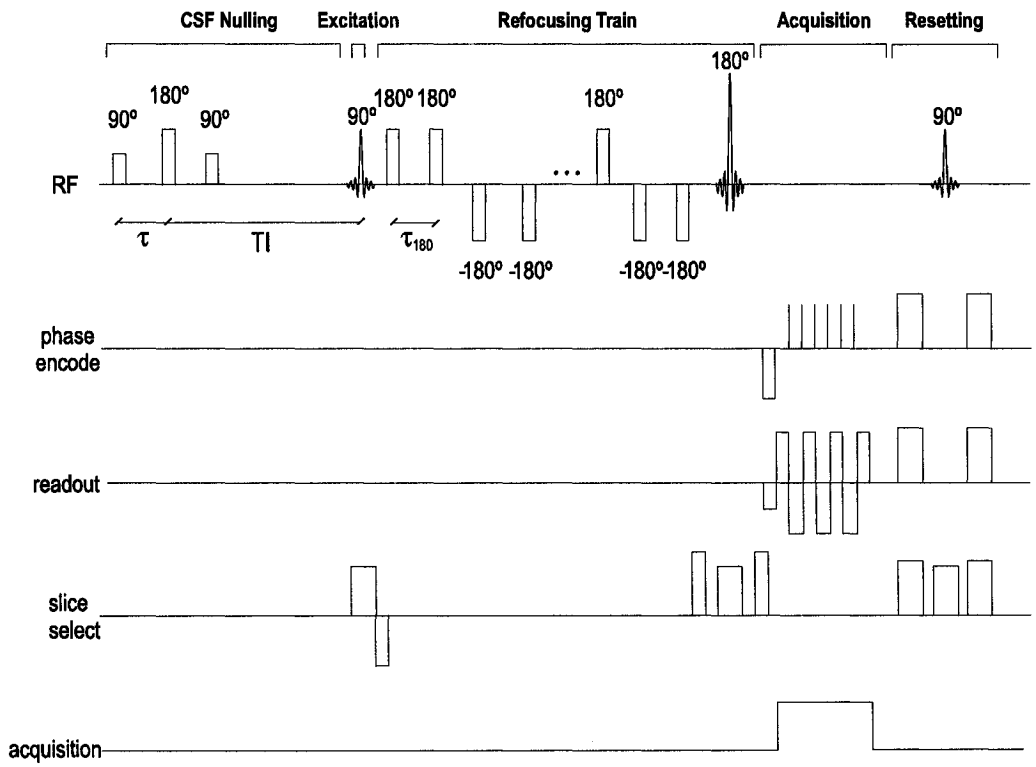

Figure 5.2: VERVE sequence diagram. The 90°_x-τ-180°_y-τ-90°_x-TI preparation is used to null the CSF signal efficiently [374]. The interval between the refocusing pulses (τ_{180}) is varied in alternate measurements, while keeping the echo time constant. Two sets of strong crushing gradients in all directions, intercepted by a 90° excitation pulse, follow the EPI readout to dephase the residual transverse and longitudinal magnetization.

cling [215] on the refocusing pulses and one cycle of RF chopping on the excitation pulse (resulting in 2 signal averages). The current implementation alternates between 64 refocusing pulses spaced by 3.7 ms and 8 refocusing pulses spaced by 30 ms. The refocusing intervals were chosen to minimize the sensitivity of the difference signal to the intravascular SE BOLD effect (*c.f.* Simulations). The final refocusing pulse is slice-selective and flanked by crushing gradients. To ensure equal T_1 recovery in each measurement, the magnetization is reset following the readout by a saturation pulse flanked by crushing gradients. We employed a 256-mm field of view (with 64x64 matrix), TR of 2 s, TI of 900 ms and the delay (τ), in 90°_x-τ-180°_y-τ- 90°_x-TI preparation, of 100 ms.

The magnetization of blood available at the time of the excitation is given by [374]:

$$M_{0_b} = 1 - e^{-\frac{TI-\tau}{T_{1_b}(Y)}}(1+(1-e^{-\frac{TR-TI-\tau}{T_{1_b}(Y)}})e^{-\frac{2\tau}{T_{2_b}(Y,2\tau)}}). \quad (5.10)$$

An analogous expression holds for tissue excitation-time magnetization, M_{0_t}. While the impact of Y on T_{1_t} is assumed to be negligible, no assumptions are made about the effect of Y on T_2 in tissue: any blood oxygenation-level induced changes in the T_2 of tissue cancel out through the subtraction of the interleaved fast and slow refocusing measurements at constant Y of each physiological state of interest. The substitution of the two excitation-time magnetization expressions into Eq. 5.3 produces the total signal equation.

5.5.3 Experimental Paradigm

The experimental protocol included a 3D RF-spoiled T_1-weighted gradient echo sequence for anatomical reference and a VERVE acquisition for CBV_v quantification. The T_1-weighted gradient echo sequence (1x1x1 mm^3) employed TR/TE of 22/10 ms and non-selective 30° excitation. The VERVE acquisition encompassed a single 5 mm-slice parallel to the calcarine sulcus, with FOV of 256 mm (64x64 matrix), TR/TE of 2000/240 ms, TI of 900 ms, the delay, τ, in the 90°_x-τ-180°_y-τ- 90°_x-TI preparation of 100 ms, and refocusing intervals of 3.7 ms and 30 ms in alternate measurements. One cycle of RF chopping on the excitation pulse was performed. The visual stimulation paradigm comprised 4 repetitions of 80/240/160 s off/on/off blocks: a uniform grey baseline alternating with a radial yellow/blue checkerboard of maximum intensity and at 4 Hz reversing contrast. Seven healthy adults (3 females and 4 males; average age 29±3 years) were studied on a 1.5 T Magnetom Sonata (Siemens, Erlangen, Germany) system. Informed consent was obtained from each subject prior to the scanning session, the experimental protocol having been approved by the Research Ethics Board of the Montreal Neurological Institute.

5.5.4 Data Analysis

The complex subtraction of data collected with opposite phase of the excitation pulse was performed (*i.e.* 2 signal averages taken) to minimize artifacts arising from any imperfections in the excitation pulse. The data were spatially smoothed using a two dimensional Gaussian filter with full width half maximum of 6 mm. The general linear model [376] was used to identify areas of statistically significant task correlation at the omnibus significance level of 0.05. Maps of percent signal changes were formed by calculating the average activation-induced changes in the signal differences between the fast and slow refocusing acquisitions. Time courses were generated by averaging the data in space, over the activated voxels, and in time, over all runs, followed by normalization to the average baseline signal.

5.6 Results

5.6.1 Simulations

The predicted venous SE BOLD effect, namely the $\Delta\hat{S}_{b,A}/\Delta\hat{S}_{b,B}$ term of Eq. 5.4 over a range of oxygen saturations representative of venous blood at rest and steady-state activation, is shown in Figure 5.3a. The contours over this surface for constant activation-induced venous blood oxygenation increases are plotted in Figure 5.3b. As expected, in the absence of any Y changes between baseline and activation, $\Delta\hat{S}_{b,A}/\Delta\hat{S}_{b,B}$ equals unity and the VERVE signal change equals the actual venous CBV change. Predictably, as the activation blood oxygenation level increases, smaller activation (relative to baseline) VERVE signal results in underestimation of the CBV_v increase. A ~20% underestimate of relative CBV_v by relative VERVE signal results from a hefty 20% venous oxygenation increase upon activation (*c.f.* Fig. 5.3).

Taking into account all three vascular compartments (with distinct contributions to resting CBV and activation-induced CBV increases) in addition to tissue and allowing a range

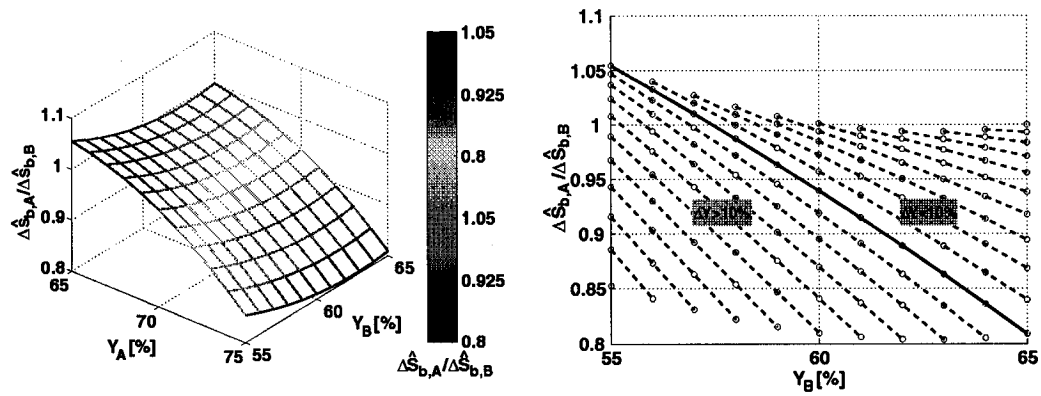

Figure 5.3: The plot of $\Delta\hat{S}_{b,A}/\Delta\hat{S}_{b,B}$ term of Eq. 5.4 for the baseline (Y_B) and activation (Y_A) blood oxygen saturations representative of venous blood in functional activation paradigms. The iso-ΔY contours (ΔY from 0 to 20%, in 1% increments) of the entire surface in (a) are shown in (b).

of blood flow increases and $\Delta CMR_{O_2}/\Delta CBF$ coupling ratios results in the percent difference between prescribed relative CBV_v and relative VERVE signal plotted in Figure 5.4. (Note that the physiological range of blood oxygenation changes of interest is thus established, as a function of flow increase and $\Delta CMR_{O_2}/\Delta CBF$ coupling ratio.) The prescribed relative CBV_v and the corresponding VERVE estimates are displayed Figure 5.5. As before, increasing the oxygenation change between baseline and activation, increases the underestimation of the VERVE-based relative CBV_v ($rCBV_v$) estimate. An additional underestimation now results from the resting IV SE BOLD effect, namely the difference in the oxygen saturation of individual blood compartments, so that some underestimation of venous blood volume changes occurs even for no activation-induced change in oxygen saturation levels in any one blood compartment (*i.e* for $\Delta CMR_{O_2}/\Delta CBF$ of 1.0). With $\Delta CMR_{O_2}/\Delta CBF$ of 0.5, established earlier for the same visual stimulation paradigm in humans [155], a representative 10% change in the venous blood oxygenation results in ~15% underestimation of relative venous CBV by relative VERVE. Moreover, for this expected

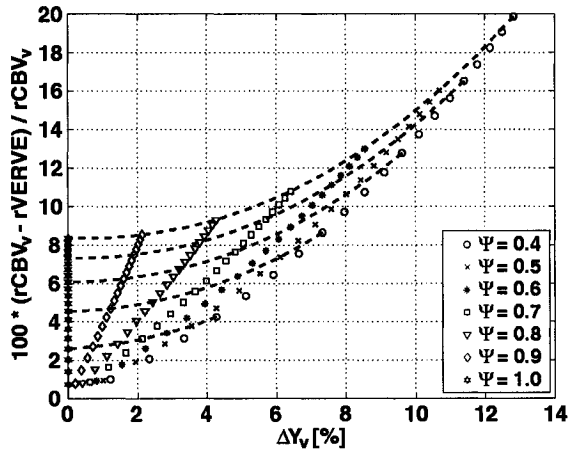

Figure 5.4: The percent difference between the simulated relative CBV_v and the relative VERVE signal plotted as a function of blood oxygenation change resulting from CBF increases from 5 to 100% (in 5% increments) and Ψ ($\Delta CMR_{O_2}/\Delta CBF$ coupling ratio) from 0.4 to 1.0 [155, 163, 185]. The iso-ΔCBF contours (in increments of 20%) are displayed as dashed curves.

Ψ of 0.5, the underestimation of CBV_v change by VERVE is well modeled ($r^2 \sim 0.8$) by:

$$(rCBV_v - 1) = 2.01\ (rVERVE - 1). \tag{5.11}$$

This linear calibration of relative VERVE signal, shown as the dashed line in Fig. 5.5, is henceforth applied for estimation of the corresponding relative venous CBV change.

5.6.2 Visual Stimulation Studies

The VERVE t-value map and CBV_v percent difference image, overlaid on the T_1-weighted anatomical image, are displayed in Figure 5.6 for one subject. The CBV_v image is calculated based on linear scaling of the corresponding VERVE image (*c.f.* Eq. 5.11), to account for the expected IV SE BOLD effect. The time course of venous CBV (again based on linear correction of the corresponding VERVE data) in the same subject is shown in Figure 5.7. Table 5.2 lists the average VERVE-based estimates of the venous CBV in visual cortex (VC) ROI of each subject. For the seven volunteers studied, the stimulation-induced

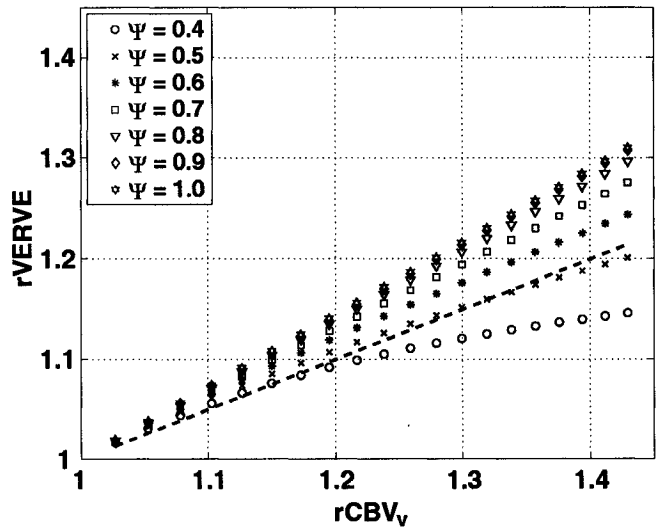

Figure 5.5: The relative VERVE signal and the simulated relative CBV_v, for ΔCBF from 5 to 100% (in 5% increments) and $\Delta CMR_{O_2}/\Delta CBF$ coupling ratio (Ψ) from 0.4 to 1.0 [155, 163, 185]. The optimal linear fit to simulated data with Ψ of 0.5 is plotted as a dashed line, corresponding to Eq. 5.11 in the text.

change in the VC VERVE signal was 8±1%, for an estimated average venous CBV change of 16±2% following calibration (*c.f.* Eq. 5.11).

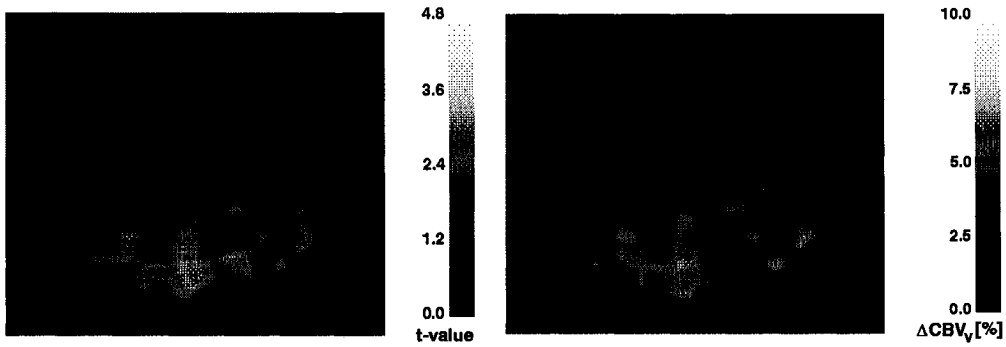

Figure 5.6: A subject's t-value map (a) and a CBV_V percent difference map (b), superimposed on the corresponding anatomical image. The threshold of statistical significance was 4.6 (α=0.05). The CBV_V changes are calculated by linear scaling of the corresponding VERVE signal changes (*c.f.* Eq. 5.11).

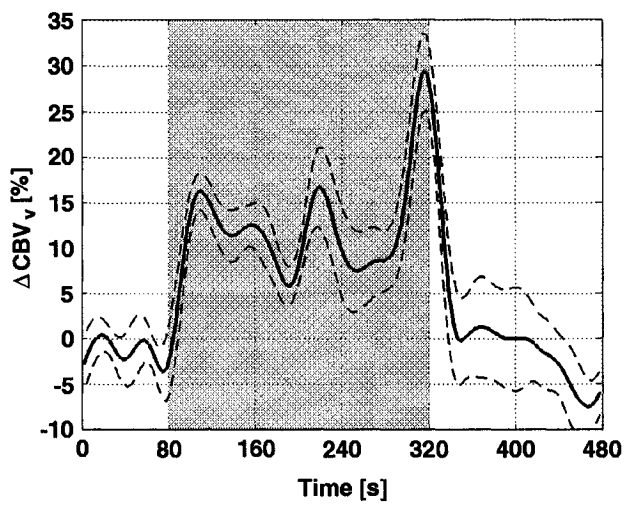

Figure 5.7: The time course of CBV_V changes in a subject's visual cortex ROI (obtained by t-map thresholding). The shaded region represents stimulus-on period. The time course data has been low pass filtered using a Hanning window (with FWHM of 24 s) and averaged over 4 runs. The y-scale is based on linear scaling (*c.f.* Eq. 5.11) of the corresponding VERVE signal changes.

Table 5.2: VERVE-based estimates of the venous blood volume changes (ΔCBV_v) based on linear calibration of VERVE signal (*cf.* Eq. 5.11). The errors in ΔCBV_v are propagated from the temporal errors in the relative VERVE signal from each subject's ROI, obtained by thresholding of the corresponding t-map. The across-subject average is quoted along with the standard error of the mean.

Subject Id.	ΔCBV_v [%]
1	14±3
2	19±10
3	25±17
4	18±6
5	15±1
6	11±2
7	12±3
	16±2

5.7 Discussion and Conclusions

We have described a novel method that allows noninvasive, repetitive measurements of venous cerebral blood volume changes. In response to visual stimulation, an average 16±2% venous blood volume increase in the VC ROI of 7 healthy adults has been estimated. While no data on venous CBV (CBV_v) increases upon functional activation in humans are available, CBV_v changes may be estimated based on the reported increases in total cerebral blood volume (CBV_t) in combination with the resting and activation blood volume distribution across the microvascular compartments. In particular, total CBV changes have been measured upon visual stimulation in humans using various modalities. Ito *et al.* reported VC CBV_t increases, upon photic flicker stimulation, of 10±13% (for 2Hz stimulation) and 21±5% (for 8Hz stimulation) using $H_2^{15}O$ PET [171]. Bolus tracking MRI experiments reported average CBV_t increases in human VC of 32±10% [20], 10.9±2.5% [248], 23.5±14.6% [111], 28±7% [274] and 18.2±2.8% [216] (the last value obtained following correction for the effects of the first on the second bolus injection). Veins being the capacitance vessels of the vascular tree [50], the venous volume contribution to total CBV has been estimated at ~40-60% [5, 50, 264, 365].Moreover, passive venous dilatation is customarily assumed to dominate the total CBV change [50, 235], consistent with observation of delayed CBV changes with respect to CBF increases [235]. On the other hand, a recent perfluorocarbon MRS study of hypercapnic perturbation in rodents suggested only a 36% venous contribution to total CBV increase [208]. Given these ranges on baseline and activation CBV distribution, the forementioned total CBV increases in human VC correspond to a very broad range of CBV_v changes, from ~6 to ~50%, easily including the present estimates but being too wide to engender much validation power.

The blood signal isolation in the present technique is achieved by varying the CPMG refocusing rate. The method therefore critically relies on the uniqueness of the τ_{180}-dependence of spin-spin relaxation time in blood. We investigated the validity of this assumption in a set of T_2 relaxometry experiments using human whole blood samples with physiologically pertinent oxygenation levels (achieved through an in vivo exercise paradig-

m) and employing a broad range of refocusing intervals (including the ones used in the current VERVE implementation) to allow robust prediction of the intravascular signal [340]. Furthermore, in a large study of occipital lobe grey and white matter tissue transverse relaxation time at 1.5 T [341], we observed a small decrease in the apparent T_2 with τ_{180} increase on the range of interest. This drop was fully explicated by the pronounced effect of the employed τ_{180} on the T_2 of blood at this field strength, while considering the blood content of each tissue. We are thus confident that the present refocusing interval variation, at each physiological state of interest, enables robust isolation of the deoxygenated blood signal.

Notwithstanding the successful isolation of the blood signal, the quantification of the deoxygenated blood volume change is hampered by the dependence of T_2 in blood on the oxygenation level. In the absence of this IV SE BOLD effect, exact correspondence between VERVE signal change and actual CBV_v changes is expected. In practice, the blood vessels contained in an fMRI voxel have a range of baseline oxygenation levels, which increase upon activation (though almost fully oxygenated arteriolar side likely experiences negligible activation-induced Y changes), with the maximal IV SE BOLD effect occurring in the venous compartment. Over the broad range of baseline and activation venous oxygen saturations considered in the simulations, the relative VERVE signal was at most 20% lower than the actual relative CBV_v in a voxel composed of venous blood and tissue alone. Allowing a large variation in flow increases and oxygen consumption to flow coupling ratios resulted in a similar prediction of the degree of relative VERVE underestimation - up to 20% - of the relative venous CBV in a voxel consisting of 3 microvascular compartments in addition to tissue. For the $\Delta CMR_{O_2}/\Delta CBF$ of 0.5 (established earlier for the same visual stimulations in humans [155]), a linear calibration of VERVE signal changes was thus derived to account for IV SE BOLD effect on VERVE signal change. Moreover, following the VERVE acquisition, ASL measurements were performed in each subject, as a part of the same scanning session [342]. Using the flow increases thus obtained (mean subject ΔCBF of $37\pm7\%$) in the functional activation model described resulted in the average subject VC

ROI CBV_v increase of 16%, identical to that obtained through the forementioned linear calibration of the VERVE signal changes. While these independently collected CBF data do provide information about the venous oxygenation level changes (via expected coupling between flow and oxygen consumption), IV SE BOLD effect estimation would ideally be done through direct in vivo measurement of focal Y_v at rest and upon activation. Moreover, an independent method of venous CBV quantification would be employed to establish the errors in the calibrated VERVE signal. In any event, the accuracy of the VERVE-based CBV_v estimate is predicated on the tight coupling between changes in oxygen saturation and blood volume, so that the application of VERVE method, as presented here, is restricted to studies of normal functional brain activation.

In modeling the intravascular volume increase, a constant total water volume of the voxel was assumed [50]. An increased proton density model [365] has also been investigated (data not shown), with minimal ensuing changes in the ΔCBV_v estimates. On the other hand, simulations of potential activation-induced hematocrit (Hct) decreases [189]resulted in a smaller underestimation of CBV_v by VERVE: nevertheless, the paucity of quantitative data on Hct changes in focal functional activation has led us to keep the Hct constant in the current modeling. Finally, no attempts were made at modeling the flow dependence of oxygen diffusivity across the capillary wall [163], VERVE estimation being sensitive only to the final blood oxygenation levels.

To minimize the set of assumptions incurred in the CBV_v quantification, the presented technique involves two signal subtractions and hence suffers from a limited signal-to-noise ratio. However, a single difference of fast refocusing measurements at the physiological state of interest may be sufficient for CBV_v estimation if, for instance, (i) negligible extravascular T_2 changes occur with activation-induced increase in blood oxygenation level [353]; and (ii) increased proton density upon activation are assumed (ensuring the cancellation of the tissue signal in the difference between fast refocusing acquisitions at activation and baseline).

At higher magnetic field strengths, the spin-spin relaxation time of blood decreases (with both a decrease in the intrinsic T_2 and a more pronounced deoxygenation induced T_2 shortening) resulting in a downward vertical shift and sharper curvature of the iso-τ_{180} curves of Fig. 5.1 [209]. Upon appropriate adjustments in the VERVE sequence refocusing intervals and echo time, the increased available blood magnetization may be exploited to produce a higher signal-to-noise ratio in the resulting difference images.

In conclusion, we presented a novel, noninvasive MR method for quantifying changes in venous cerebral blood volume using deoxyhemoglobin as the endogenous contrast agent and exploiting the dependence of T_2 in deoxygenated blood on the refocusing interval. The underestimation of relative CBV_v by VERVE, due to the intravascular SE BOLD effect, was found to be at most 20% over the physiologically relevant range of oxygenations using previously obtained blood spin-spin relaxometry data and a model of normal functional brain activation. For the expected coupling between oxygen consumption and flow, a linear calibration of the VERVE signal was derived to account for the IV SE BOLD effect and produce estimates of venous CBV changes. The VERVE acquisition was applied in an fMRI study of 7 healthy young adults, visual stimulation resulting in an average visual cortex venous blood volume increase of 16±2%. The method affords noninvasive monitoring of venous CBV, of particular interest in studies of BOLD fMRI mechanism and investigations of flow-volume coupling in humans.

Acknowledgements

This work was supported by the Natural Sciences and Engineering Research Council of Canada and the Canadian Institutes of Health Research.

Chapter 6

BOLD Signal as a Marker of Neuronal Deactivation

6.1 Preface

The final manuscript of this thesis probes the physiology of normal brain activation further by focusing on the mechanism underlying sustained decreases in the BOLD fMRI response. Functional magnetic resonance imaging was used to measure changes in blood oxygenation level dependent (BOLD) signal, cerebral blood flow (CBF), and cerebral metabolic rate of oxygen consumption (CMR_{O_2}) accompanying neuronal inhibition. Eight healthy volunteers performed a periodic right-hand pinch grip every second using 5% of their maximum voluntary contraction), a paradigm previously shown to produce robust ipsilateral neuronal inhibition. To simultaneously quantify CBF and BOLD signals, an interleaved multi-slice pulsed arterial spin labeling (PASL) and T_2^*-weighted gradient echo sequence was employed. The CMR_{O_2} was calculated using the deoxyhemoglobin dilution model [77, 155], calibrated by data measured during graded hypercapnia. In all subjects, BOLD, CBF, and CMR_{O_2} signals increased in the contra- and decreased in the ipsilateral primary motor (M1) cortex. The relative changes in CMR_{O_2} and CBF were linearly related, with a slope of ~ 0.4. The coupling ratio thus established for both positive and negative CMR_{O_2} and

CBF changes is in close agreement with the ones observed by earlier studies investigating M1 perfusion and oxygen consumption increases. These findings characterize the hemodynamic and metabolic changes accompanying neuronal deactivation and thereby validate the use of BOLD fMRI as an indicator of downregulation in neuronal activity.

Hemodynamic and Metabolic Responses to Neuronal Inhibition

Bojana Stefanovic, Jan M. Warnking, and G. Bruce Pike

McConnell Brain Imaging Centre, Montreal Neurological Institute,

3801 University St., McGill University, Montreal, Quebec, Canada H3A 2B4

NeuroImage, 2004; 22(2): 771-8

6.2 Abstract

Functional magnetic resonance imaging (fMRI) was used to investigate the changes in blood oxygenation level dependent (BOLD) signal, cerebral blood flow (CBF) and cerebral metabolic rate of oxygen consumption (CMR_{O_2}) accompanying neuronal inhibition. Eight healthy volunteers performed a periodic right-hand pinch grip every second using 5% of their maximum voluntary contraction (MVC), a paradigm previously shown to produce robust ipsilateral neuronal inhibition. To simultaneously quantify CBF and BOLD signals, an interleaved multi-slice pulsed arterial spin labeling (PASL) and T_2^*-weighted gradient echo sequence was employed. The CMR_{O_2} was calculated using the deoxyhemoglobin dilution model, calibrated by data measured during graded hypercapnia. In all subjects, BOLD, CBF and CMR_{O_2} signals increased in the contra- and decreased in the ipsilateral primary motor (M1) cortex. The relative changes in CMR_{O_2} and CBF were linearly related, with a slope of ~ 0.4. The coupling ratio thus established for both positive and negative CMR_{O_2} and CBF changes is in close agreement with the ones observed by earlier studies investigating M1 perfusion and oxygen consumption increases. These findings characterize the hemodynamic and metabolic downregulation accompanying neuronal inhibition and thereby establish the sustained negative BOLD response as a marker of neuronal deactivation.

Key words: fMRI; negative BOLD; perfusion; oxygen consumption; inhibition;

6.3 Introduction

Functional magnetic resonance imaging (fMRI) using BOLD effect [261] has become a prominent tool for examining brain function. Despite a wealth of BOLD-based neuroscientific studies and a growing use of BOLD fMRI in clinical applications, the physiological mechanisms modulating the blood oxygen saturation in the context of neuronal activation remain incompletely understood. While many aspects of the steady-state positive BOLD response have been investigated, attention has only recently been given to sustained decreases in the BOLD signal.

In both animal [144, 315, 316] and human visual stimulation studies [69, 82, 317], decreased BOLD signal has been observed in the non-stimulated areas of the visual cortex upon partial visual field stimulation as well as areas corresponding to regions in the visual field not receiving the subject's attention [348]. Several theories have been put forth by the investigators to explain these observations: from the purely hemodynamic effect of "blood stealing" to neuronal inhibition, or some combination of these [69, 82, 317]. During an acoustically triggered saccade paradigm, a bilateral negative BOLD response has been reported in the visual cortex; simultaneously, near-infrared spectroscopy revealed decreased oxy- and increased deoxy-hemoglobin concentration (for an overall decrease in total hemoglobin) [367]. These findings have been attributed to decreased blood flow resulting from the inhibition of background activity in the visual cortex during saccades, as described in psychophysiologic studies [87].

A sustained negative BOLD response has also been observed in the motor cortex. A steady-state decrease in BOLD signal has been documented in the ipsilateral primary sensorimotor cortex of normal volunteers during sequential finger apposition [4, 257]. A PET study reported ipsilateral CBF decreases during low force, right index finger flexion [79]. In contrast, ipsilateral CBF increases were measured during high force finger flexion [79] and positive ipsilateral BOLD responses documented during circling shoulder movements [257]. Finally, a decreased BOLD signal has been documented in the ipsilateral primary sensorimotor cortex of normal volunteers performing a low force, phasic pinch grip

task [142], accompanied by a decrease in blood flow [159]. Transcallosal inhibition, reported in a plethora of transcranial magnetic stimulation (TMS) studies [31, 103, 118, 217, 255], has been suggested as the likely origin of these changes [142].

Determining the origins of sustained negative BOLD responses accompanying neuronal inhibition is important not only for understanding the BOLD mechanism, but also for probing the extent and nature of neurovascular coupling, thereby establishing the applicability of BOLD as a marker of up- as well as down- regulation of neuronal activity. We thus set out to investigate the hemodynamic and metabolic processes concomitant to the negative BOLD response in a low-force, phasic pinch grip of the right index finger and thumb in right-handed healthy volunteers. We hypothesized that the steady-state negative BOLD response resulted from sustained decreases in both perfusion and oxygen consumption and, furthermore, that the same relationship between CMR_{O_2} and CBF underlied both positive and negative steady-state BOLD signal changes. The variations in BOLD, CBF, and CMR_{O_2} were measured by interleaved T2*-weighted and PASL acquisitions, with hypercapnic calibration allowing CMR_{O_2} quantification. Here we report on the relationship between blood flow and oxygen consumption in regions of sustained BOLD and CBF signal increases, in the contralateral M1, and their decreases, in the ipsilateral M1. Since the paradigm employed induces ipsilateral neuronal inhibition, these findings have direct implications for the use of negative BOLD response as a marker of neuronal deactivation.

6.4 Methods

6.4.1 Motor Task

Prior to scanning, the maximum voluntary contraction of the right-handed pinch grip was measured for each subject. The subjects were then trained to perform the pinch grip task at a frequency of 1 Hz, as cued by a metronome. On each grip, subjects pressed a water-filled ball with the thumb and the index finger of the right hand. The ball was connected to a pressure transducer (Ashcroft, Stratford, Connecticut), in turn linked to a data acquisition

card (National Instruments, Austin, Texas). The real-time recording and analysis of the exerted pressure was done using MATLAB's data acquisition toolbox (Mathworks, Natick, Massachusetts). An auditory feedback was provided to the subject: a low frequency tone indicated that the force applied was in the desired range, namely within 15% of the target level; a high frequency tone accompanied too strong a force; and no tone was played out when insufficient force was exerted. To minimize habituation, the target level was randomized on each pinch grip and varied between 4 and 7% of the subject's MVC. A metronome, set at 60 beats per minute was on during the anatomical scan for accustomization and then switched off for the functional scan, the subjects having been instructed to maintain a pinch grip frequency of 1 Hz.

6.4.2 Hypercapnic Modulation

Mild hypercapnia was induced through administration of mixtures of carbon dioxide and air through a nonrebreathing face mask (Hudson RCI, Model 1069, Temecula, CA). At baseline, the subjects were inhaling medical air, supplied at 16 L/min. During hypercapnic perturbations, a premixed preparation of 10% CO_2, 21% O_2 and balance N_2 (BOC Canada Ltd., Montreal, Quebec, Canada) was combined with medical air in a Y-connector. The CO_2 concentration in the mixture varied between 2.5 and 10%. At each level, the flow rates were adjusted to maintain a total flow rate of 16 L/min. End-tidal CO_2 was measured via a nasal cannula with monitoring aspirator (Normocap 200, Datex Inc., Plymouth, Maine) and increased an average 23±2 mm Hg (or 54±4%) during inhalation of the highest concentration CO_2 mixture. Subjects were asked to breathe at a constant rate, and their respiratory rate was monitored via a respiratory belt.

6.4.3 Experiment

Eight healthy adults (2 females and 6 males; average age 28±3 years) participated in the study. All the subjects were right-handed, with an average Edinburgh inventory laterality

quotient [266] of 87±18. The scanning protocol consisted of a high-resolution 3D RF-spoiled T_1-weighted gradient echo (1x1x2 mm^3) sequence for anatomical reference, followed by interleaved multi-slice PASL and T_2^*-weighted gradient echo sequence for CBF and BOLD signal measurements. The high resolution gradient echo sequence employed a TR of 22 ms, a TE of 10 ms, and non-selective 30° RF-spoiled excitation. The CBF and BOLD acquisitions covered 7 slices (4x4x7 mm^3; inter-slice gap of 0.7 mm) parallel to the AC-PC line, with the seventh slice grazing the top of the brain. The CBF data were acquired using a proximal inversion with a control for off-resonance effects (PICORE) labeling scheme [375] with two presaturation pulses in the imaging region followed by an adiabatic FOCI inversion pulse [267] ($\beta = 1172\ s^{-1}$, $\mu = 8$, $T_p = 10.24$ ms, $B_{1,max} = 0.28$ Gauss, FOCI factor 9) in the labeling region (thickness of 100 mm, gap of 5 mm) and a post-label delay of TI=1200 ms. An EPI readout (2232 Hz/pixel) was employed, with an echo time of 22 ms for CBF and 50 ms for BOLD. In both cases, the repetition time was 2.5 s. The functional paradigm involved 12 sessions of 20 s/60 s/40 s off/on/off blocks, rest alternating with the low force, phasic, right-handed pinch grip, the beginning of each block being indicated by auditory cues. Following the functional scan, medical air alternating with graded hypercapnia was administered in 1 min/3 min/2 min blocks. Subjects were immobilized using a vacuum bag and a head holder assembly. The RF body coil was used for transmission and a quadrature head coil for signal reception. All the examinations were performed on a Siemens 1.5T Magnetom Sonata system. Informed consent was obtained from each subject prior to the scanning session, the experimental protocol having been approved by the Research Ethics Board of the Montreal Neurological Institute.

6.4.4 Data Analysis

The motion correction parameters of the functional data set were estimated using AFNI's 3dvolreg software [70] and the frames with estimated translation exceeding 1 mm or rotation greater than 1° excluded from the analysis. The data were spatially smoothed using a three dimensional Gaussian filter with full width half maximum of 6 mm. Drift was re-

moved by subtracting from each voxel's time course the first components of its discrete cosine transform, with a cutoff frequency of one half of the stimulation paradigm frequency. The generalized linear model [376] was used to identify areas of statistically significant task correlation at the omnibus significance level of 0.05 in BOLD and CBF data, respectively. Upon establishing statistical significance of both BOLD and CBF responses in both hemispheres of every subject, regions of interest were defined on BOLD and CBF percent signal change maps, respectively, by selecting the M1 voxels showing at least 30% of the peak signal change in the primary motor cortex. This selection strategy maximized the dynamic range of sampled CBF variations and thereby improved the robustness of the coupling ratio estimation. To allow for establishment of a physiological steady-state, the hypercapnic data acquired within half a minute following a change in the concentration of the inspired CO_2 was excluded from the analysis. The hypercapnic data were averaged across all subjects, at each level of hypercapnia, and a common maximum achievable BOLD signal change (M) was estimated by linear fitting of the transformed and averaged CBF data *vs.* averaged BOLD data to the deoxyhemoglobin dilution model [77, 155]:

$$\frac{\Delta\text{BOLD}}{\text{BOLD}_0} = M\left(1 - \left(\frac{\text{CBF}}{\text{CBF}_0}\right)^{\alpha-\beta}\right). \tag{6.1}$$

We thus assumed no effect of the mild hypercapnia elicited in this experiment on the rate of oxygen consumption. The α and β were set to 0.38 and 1.5, respectively [34, 135]. The individual task-induced CMR_{O_2} changes were next calculated using the estimated M (and its associated standard error) in combination with the measured BOLD and CBF data during the functional run, as follows [77, 155]:

$$\frac{\text{CMR}_{O_2}}{\text{CMR}_{O_2|0}} = \left(1 - \frac{\left(\frac{\Delta\text{BOLD}}{\text{BOLD}_0}\right)}{M}\right)^{\frac{1}{\beta}} \left(\frac{\text{CBF}}{\text{CBF}_0}\right)^{1-\frac{\alpha}{\beta}}. \tag{6.2}$$

Therefore, the errors in the M estimate from the linear fitting of the transformed and averaged CBF hypercapnia data to averaged BOLD hypercapnia data have been propagated into the errors on the calculated activation-induced CMR_{O_2} changes. Finally, a single straight line was fit to the noisy CMR_{O_2}, noisy CBF data pairs from both contra- and ipsilateral ROIs of all subjects to obtain an optimal estimate of the CMR_{O_2}/CBF coupling ratio. The quality of the fit was assessed by χ^2 analysis, with the χ^2 probability reported as q [284].

6.5 Results

Task induced increases in BOLD signal were observed, contralaterally, in the primary sensorimotor cortex (SM1), premotor cortex (PMC), supplementary motor area (SMA), as well as as part of the posterior parietal association cortex (PPC) flanking the postcentral sulcus. Ipsilaterally, BOLD signal increased in the secondary areas (namely, PMC, SMA and PPC), but decreased in the primary sensorimotor cortex. Figure 6.1 shows a slice of BOLD and CBF ROIs, summed over all subjects after registration [66] with the Montreal Neurological Institute template brain [96]. The world coordinates (x,y,z) of the center of mass of the percent difference based M1 ROIs transformed into the Talaraich space and summed over all subjects were (-39,-19,54) for contralateral BOLD, (41,-22,54) for ipsilateral BOLD, (-37,-20,56) for contralateral CBF, and (37,-22,56) for ipsilateral CBF. The BOLD and CBF regions of interest for a sample subject are displayed in Figure 6.2.

A typical set of BOLD signal and CBF time courses, in both contra- and ipsilateral M1 ROIs of a subject, is shown in Figure 6.3. Figure 6.4 displays the measured BOLD and CBF data pairs, for hypercapnic perturbation and motor task, as well as the calculated iso-CMR_{O_2} contours. In 7 out of 8 subjects, the magnitude of CBF and BOLD signal changes were significantly larger in the contra- than in the ipsilateral ROI. The maximum achievable BOLD signal increase (M), obtained by linear fitting of the average hypercapnia data across all subjects, was 0.072±0.010, corresponding to a ΔR_2^* of -1.4±0.2 s^{-1}. The χ^2 analysis

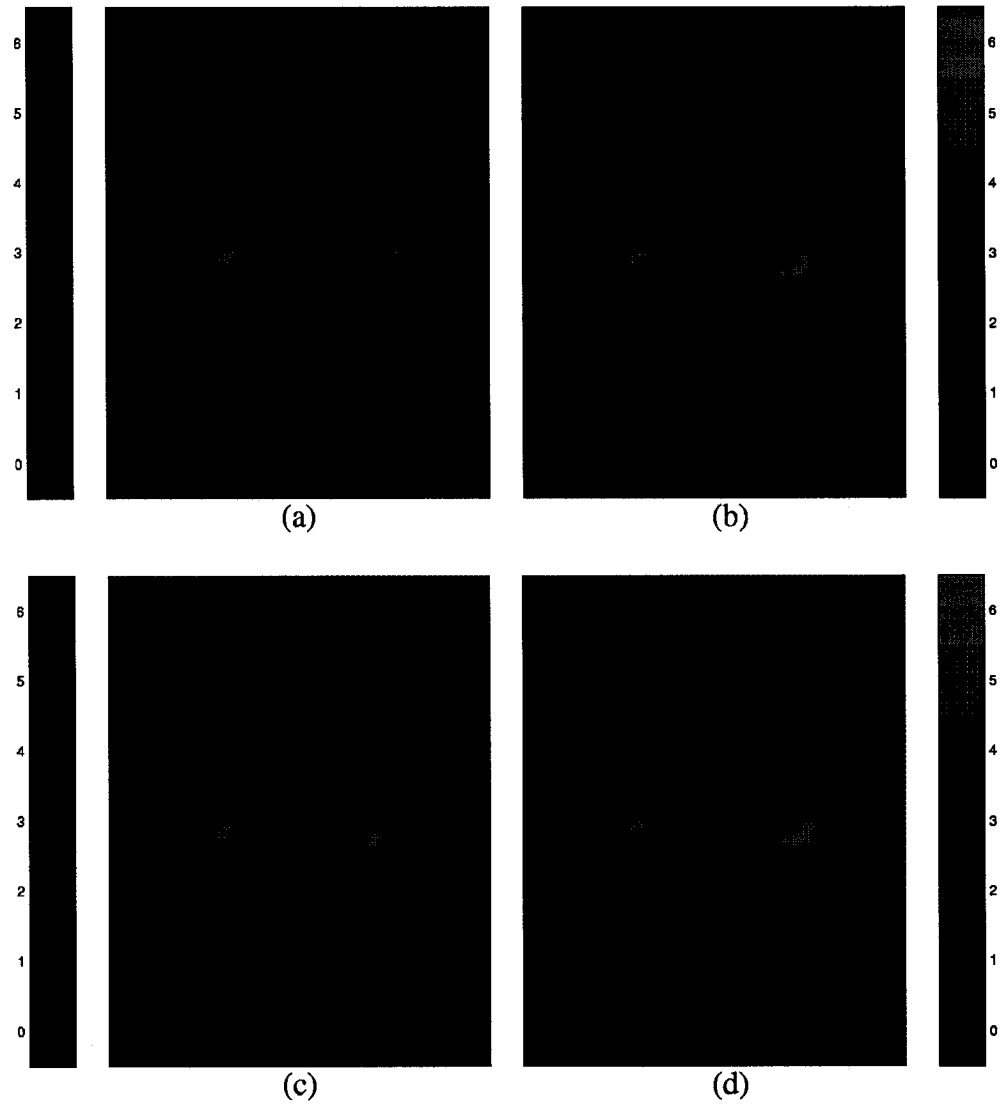

Figure 6.1: Regions of interest based on percent difference changes (left column) and t-values (right column), transformed into the Talaraich space and summed over all subjects, are overlaid on the average of all subjects anatomical scans in the Talaraich space. The top row shows BOLD and the bottom row CBF ROIs, the contralateral ROIs being displayed in red and the ipsilateral in green.

indicated a good fit (q=0.37) [284]. Finally, the calculated CMR_{O_2} and the corresponding measured CBF changes, for each subject, are displayed in Figure 6.5. The slope of the straight line fit to these data yielded a CMR_{O_2}/CBF coupling ratio of 0.44±0.04 (with q of 0.98 indicating an excellent χ^2 fit [284]).

(a) (b)

Figure 6.2: The regions of interest for BOLD (a) and CBF (b) based on respective percent difference changes in a subject. The contralateral ROIs are displayed in red and the ipsilateral in green.

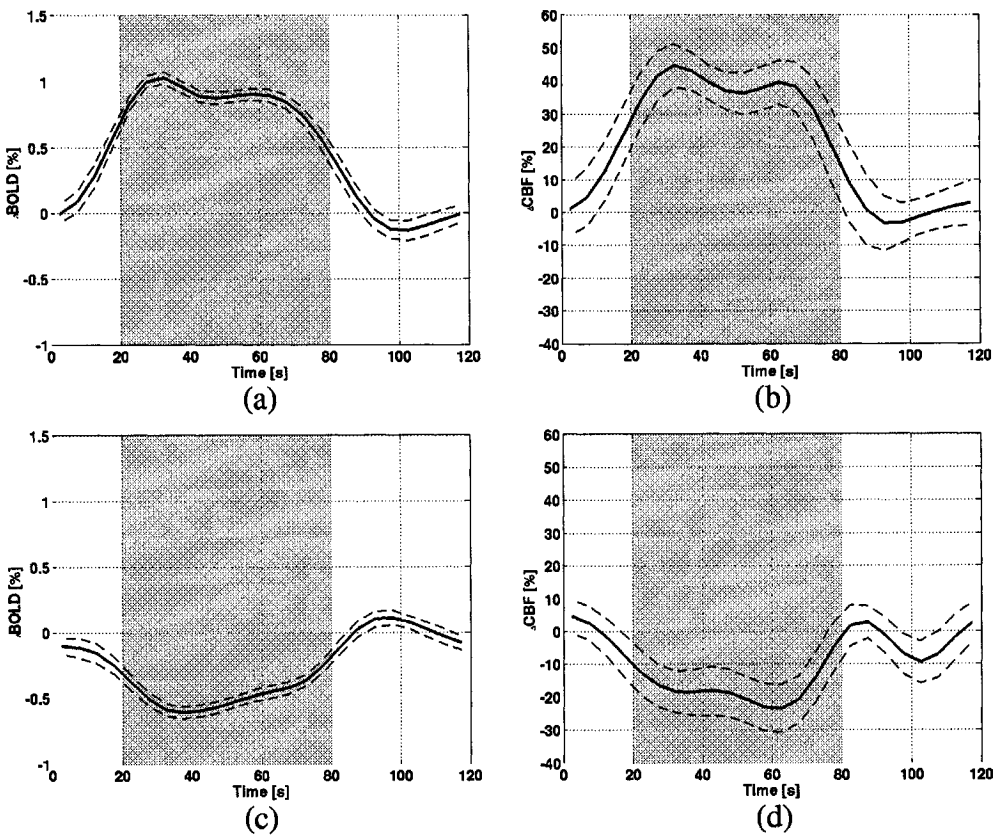

Figure 6.3: Time courses of contralateral (positive) BOLD (a) and CBF (b), as well as ipsilateral (negative) BOLD (c) and CBF (d) percent changes in a subject. The standard errors are shown as dashed lines. All time course data have been low pass filtered with a Hanning window (FWHM=20 s) prior to averaging across the 12 sessions.

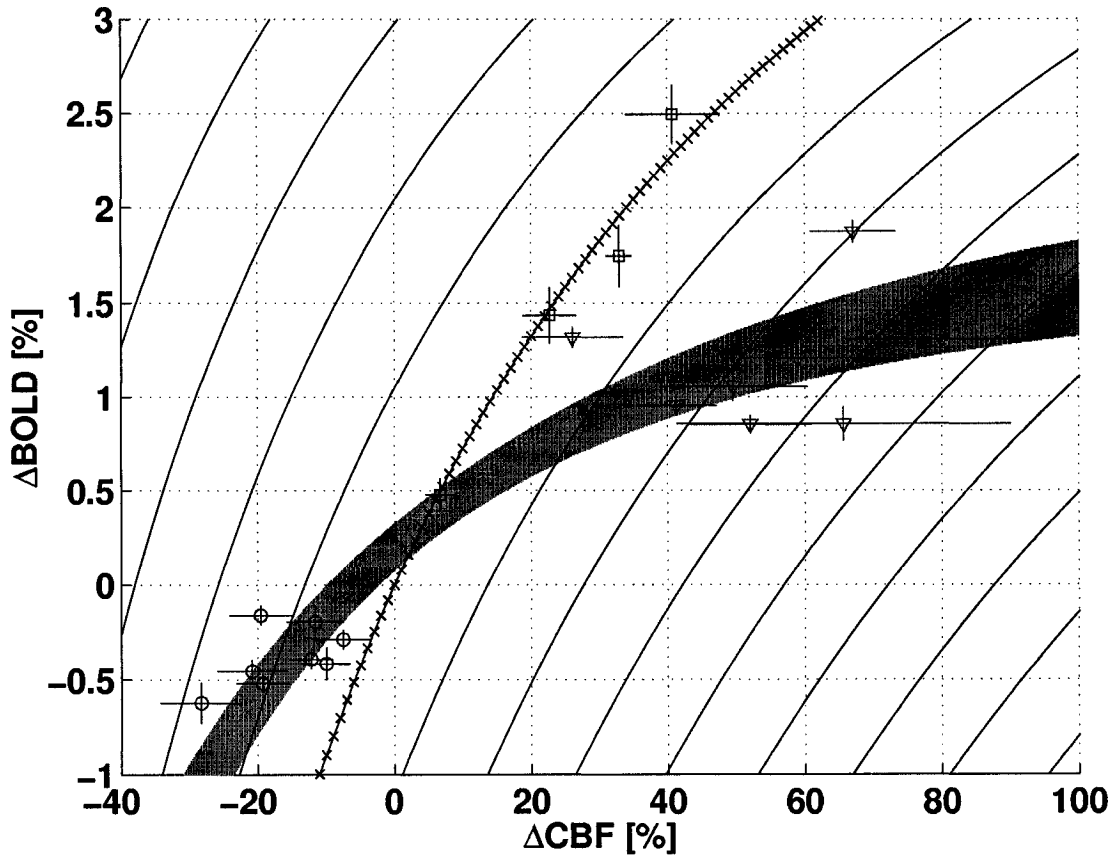

Figure 6.4: The percent changes in BOLD and CBF signals in the ipsilateral ROIs (blue circles) and contralateral ROIs (red triangles) for each subject. The average hypercapnia data (black squares) are displayed along with the corresponding fit, representing the baseline iso-CMR_{O_2} contour, and providing the estimate of the maximum achievable BOLD signal change. The estimated M was substituted into equation [13] of the deoxyhemoglobin dilution model [155] to generate non-baseline iso-CMR_{O_2} contours, at 10% intervals. The shaded area corresponds to the shaded region of Figure 6.5.

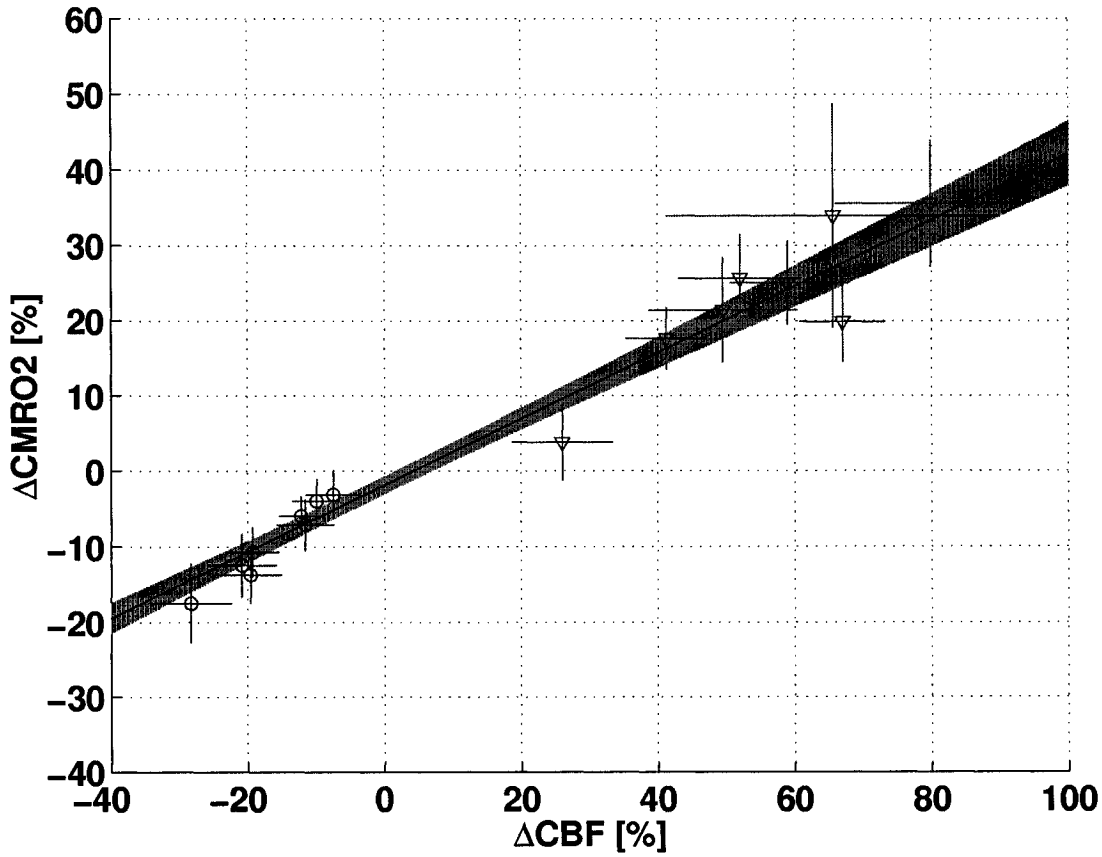

Figure 6.5: The oxygen consumption variations corresponding to each subject's perfusion changes induced by the motor task in ipsilateral ROIs (blue circles) and contralateral ROIs (red triangles). The optimal straight line fit (q=0.98) to these data is shown superimposed, providing the coupling ratio of 0.44±0.04. The shaded region represents the standard error in the linear fit.

6.6 Discussion

The present findings demonstrate a consistent coupling between perfusion and oxygen consumption governing both positive and negative BOLD responses. While no other results exist on the ipsilateral CBF and independently measured CMR_{O_2} changes in the context of this or an equivalent paradigm, similar data on the contralateral steady-state BOLD signal increases are available. Specifically, Kastrup *et al.* [185] report the maximum achievable BOLD signal change (M), averaged over all subjects, at 1.5 T and TE of 40 ms to be 9±3%, *i.e.*, ΔR_2^* of -2.2±0.7 s^{-1}, for bilateral finger tapping in healthy volunteers. The M estimated from our average graded hypercapnia data, of 7.2±1.0% (with q of 0.37) or ΔR_2^* of -1.4±0.2 s^{-1}, is thus in good agreement. Our M estimate is also in agreement with the average 9±1% or ΔR_2^* of -1.8±0.2 s^{-1} obtained in earlier 1.5 T motor cortex studies in our lab, using TE of 50 ms [12].

The slope of 0.44±0.04 of the best line fit to both contra- and ipsilateral CMR_{O_2} *vs.* CBF percent signal changes is only slightly larger than the average of 0.33±0.06 reported by Kastrup and 0.35±0.03 found in this lab [12]. The quality of the single linear fit to both ipsi- and contralateral CBF and CMR_{O_2} changes is excellent (q=0.98). Treating the data from each hemisphere separately produces slope estimates that are within one standard error of each other (results not shown). It is also instructive to note that fitting a separate M value for each subject, as was done by Kastrup *et al.*, does not influence the linear relationship between CMR_{O_2} and CBF data, but results in a small increase of the estimated coupling ratio and the corresponding error, to 0.53±0.06. In view of the uncertainty in the value of the exponent α, describing the flow/volume coupling in the deoxyhemoglobin dilution model, we have investigated the dependence of the present findings on variation of α. Specifically, over the range of reported α values from 0.38 (the presently selected value) to 0.18 [135, 179, 233], we observed a linear decrease in the estimated M value, from 7.2±1.0% to 6.3±0.9% (accompanied by a small drop in the quality of the fit, q decreasing from 0.37 to 0.35). Correspondingly, the estimated CMR_{O_2}/CBF coupling ratio increased, roughly linearly, from 0.44±0.04 to 0.53±0.05 (with negligible effect to the

quality of the linear fit). We also note that both M and coupling ratio estimates may be affected by systematic bias in the flow measurement of the presently employed PICORE tagging method. However, paralleling the low sensitivity of the coupling ratio estimate to variations in α over a physiologically relevant range, a bias in the flow measurement - as high as 30% underestimation for hypercapnia or 15% overestimation for motor activation - does not affect the finding of linear coupling between oxygen consumption and flow. Moreover, based on ASL kinetic signal model simulations (not shown), impact of such a bias on M and coupling ratio estimates is on the order of the random measurement error.

While the lack of independent oxygen metabolism measurements by Shmuel *et al.* precludes a CMR_{O_2}/CBF coupling ratio comparison, the present findings certainly agree with their qualitative conclusion of smaller relative changes in CMR_{O_2} than CBF in the regions of negative BOLD response [317]. We conclude that there is a consistent coupling between oxygen consumption and blood flow for sustained positive and negative BOLD responses.

Our ROI definition was carried out using the percent difference maps, combined with anatomical constraints. While the details of ROI delineation do not affect the linearity of the relationship between CMR_{O_2} and CBF, they do influence the coupling ratio estimate. Specifically, the present choice of ROIs maximizes the dynamic range of sampled data and hence the estimation power. Moreover, while incomplete overlap between the BOLD and CBF ROIs may introduce bias, only partial spatial congruency of the CBF and BOLD responses has been documented in a number of studies [218, 224, 234]. Finally, the CBF and BOLD ROIs employed are largely overlapping, as shown in Figures 6.1 and 6.2. Ideally, the regions of interest would be defined through a method that is independent of any metabolic and hemodynamic processes and, instead, probes the neuronal activity directly.

While no direct measurements of neuronal activity have been made in this experiment, numerous electrophysiological studies using transcranial magnetic stimulation (TMS) have documented that unihemispheric magnetic stimulation of the primary motor cortex can induce inhibition in the M1 of the other hemisphere [31, 103, 118, 217, 255]. This interhemispheric inhibition phenomenon also arises with voluntary manual tasks: the study

by Liepert *et al.* has reported a significant decrease in the TMS-induced motor evoked potentials in the relaxed contralateral first dorsal interosseous muscle, while the subjects were performing the current motor task with the ipsilateral hand [217].

The paradigm used in this study was chosen to ensure distinct blood supplies to the positive and negative BOLD response regions. Therefore, a purely hemodynamic effect involving a redirection of flow from the unactivated areas surrounding the activated ones, or blood stealing, is a highly improbable origin of the observed decreases in BOLD and CBF. Moreover, the right hand task in strictly right handed individuals maximized the degree of the inhibition: the dominant motor cortex having been shown to exhibit more inhibitory control over the non-dominant one than *vice versa* [56, 213, 217, 255, 257, 387].

Notwithstanding relatively sparse interhemispheric connections of the cortical motor areas representing the most distal parts of the extremities [75, 133, 240], the ipsilateral neuronal inhibition is likely mediated via activation (by excitatory axons crossing the corpus callosum) of local ipsilateral $GABA_B$ergic interneurons [4, 24, 76, 79, 142, 199, 257]. Other investigators have suggested that subcallosal routes may, in part, relay the inhibitory effect [31, 118]. Disfacilitation of the excitatory drive onto the α-motorneurons has also been proposed [118] (TMS not affording means of discerning between the two phenomena).

The underlying purpose of these interhemispheric inhibitory interaction is still not clear. On the basis of EMG recordings of bilateral muscle activation during complex unilateral motor tasks [198], the proposition has been made that the movements of distal extremities are prepared bilaterally, the late transcallosal inhibition then ensuring unilateral movement [39, 300]. In addition to the suppression of mirror movements, the ipsilateral inhibition may be aimed at reducing interference, aiding focus and thereby achieving high manual dexterity in complex unilateral tasks [115].

Irrespective of the exact purpose of the inhibitory effect in this paradigm, local changes in metabolic and hemodynamic processes most likely reflect net variations in focal energy requirements, in turn arising from the overall level of neuronal firing, BOLD signal changes thus being determined by a balance between increased and decreased neuronal ac-

tivity. The present findings extend the range of applicability of BOLD signal as a marker of neuronal state and hence brain function over a normal physiological range. Furthermore, the consistency of the coupling ratio for positive and negative BOLD response domains establishes existence of a unique relationship between blood flow and oxygen consumption in the healthy human brain. However, careful investigations, simultaneously quantifying hemodynamic and metabolic changes, are necessary to establish the role of BOLD in determining functional deficits and plasticity under pathological conditions.

6.7 Conclusion

We have found a consistent linear relationship between oxygen consumption and perfusion in regions of sustained positive as well as negative BOLD response under normal physiological conditions. The slope of the linear fit to CMR_{O_2} *vs.* CBF changes from both ipsi- and contralateral ROIs was 0.44±0.04, in agreement with earlier motor studies investigating steady-state BOLD signal increases. The current findings on the coupling between metabolic and hemodynamic processes underlying sustained BOLD decreases, in combination with extensive evidence on the accompanying neuronal inhibition from TMS experiments, provide support for steady-state negative BOLD response as a marker of neuronal deactivation.

6.8 Acknowledgments

The authors thank Dr. Richard Hoge for critical reading of the manuscript. This work was supported by the Natural Sciences and Engineering Research Council of Canada and the Canadian Institutes of Health Research.

Chapter 7

Conclusion

7.1 Summary and Implications

In this dissertation, venous refocusing for volume estimation (VERVE), a novel fMRI method for noninvasive, repetitive measurements of venous cerebral blood volume changes was introduced. The theoretical basis for the blood signal isolation strategy in this technique was established through a series of relaxometry measurements. These methodological developments were undertaken to allow the investigation of the BOLD mechanism and thus address some of the outstanding questions surrounding normal brain physiology. In addition, this thesis involved a study that focused on the controversial sustained decreases in the BOLD fMRI response and probed the applicability of negative BOLD response as a marker of neuronal downregulation.

In Chapter 3, important findings were made on the behaviour of tissue transverse relaxation in the occipital lobe. Significant methodological improvements were made with respect to the earlier studies [19, 386] investigating the grey-to-white matter contrast in the occipital lobe. Specifically, the present study employed the *de facto* standard sequence for in vivo T_2 relaxometry [282, 369, 370] (thereby avoiding possible spurious statistically significant variation in T_2 estimates [370]) and used much larger regions of interest compared to prior studies, thus maximizing the signal-to-noise ratio. At the same time, careful anal-

ysis (Bayesian classification of high resolution anatomical acquisition, and careful training data selection in each subject, combined with a very low threshold of average normalized *a posteriori* probability of CSF in the ROIs) afforded high sensitivity to the intrinsic contrast between grey and white matter. We found a preserved grey-to-white matter contrast in the occipital lobe of healthy, young adults, in contrast to earlier studies [19, 386], yet in agreement with theoretical predictions [386]. Moreover, the small decrease, of 3±2 %, in the apparent T_2 values of either tissue with refocusing interval elongation from 8 to 22 ms was in excellent agreement with theoretical predictions based on considerations of blood volume fraction of these tissues and the effect of this refocusing interval variation on the transverse relaxation time of blood. This study thus afforded significant insight into the refocusing interval dependence of tissue transverse relaxation, while providing the empirical basis for subtracting slow from fast refocusing interval acquisitions, in our VERVE method, to isolate the blood signal.

In the ensuing studies on blood relaxometry, described in Chapter 4, we collected the most extensive up-to-date set of $T_{2_{blood}}$ data over the physiologically pertinent range of blood oxygen saturation, hematocrit and CPMG refocusing intervals achievable in vivo. Simultaneous fitting of these data to the current models of blood relaxation rate enhancement due to sequestration of paramagnetic deoxygenated heme irons in erythrocytes provided strong support for the use of the diffusion [172] over fast exchange model [225]. Furthermore, a robust parametrization of the diffusion model was obtained, allowing prediction of the spin-echo intravascular BOLD effect at 1.5 T. In addition, support for recently reported [324] linear decrease of spin-lattice relaxation rate on blood oxygenation level was found, and a significant increase of $R_{1_{blood}}$ with hematocrit, findings of particular relevance for many MR techniques dependent on blood signal isolation or nulling [222, 258] as well as perfusion quantification via arterial spin labeling methods [324].

In Chapter 5, a novel noninvasive fMRI technique for quantification of venous cerebral blood volume changes was described. A signal model was developed, and in vitro blood relaxometry data used to optimize the sequence parameters. In addition, a model of phys-

iological changes accompanying normal brain activation was described and employed in combination with blood signal characterization from Chapter 4 as well as literature values, to evaluate the intravascular spin-echo BOLD effect on VERVE signal and achieve robust estimation of cerebral blood volume changes accompanying normal brain activation. The first noninvasive MR method for direct measurements of venous CBV was thus developed and demonstrated in the visual stimulation study of healthy, young adults. The findings indicate an average 16±2% increase of venous CBV in the visual cortex, concomitant to 37±7% increase in blood flow, in concordance with the theoretical predictions of venous dilatation dominating the total blood volume changes [50, 235] and a power law relationship applying between total CBF and total CBV changes [135, 171]. Most importantly, a noninvasive fMRI method for tracking the volume changes in the part of vascular tree pertinent to the BOLD fMRI signal is thus afforded, allowing further explorations into the mechanism underlying the most prominent current tool for studying brain function.

The final study of this dissertation, described in Chapter 6, focused on the physiological changes accompanying sustained decreases in the BOLD fMRI signal, a subject that has raised considerably controversy in the fMRI community over the last few years [142, 317, 328]. We employed a low-force phasic pinch grip, a task known to elicit neuronal excitation in the contralateral and inhibition in the ipsilateral primary motor cortex. Through interleaved BOLD and CBF measurements and a hypercapnic calibration, we thus quantified both CBF and CMR_{O_2} changes in response to normal functional activation in homologous brain regions. Notably, while BOLD, CBF and CMR_{O_2} all increased in the contralateral M1, negative BOLD response in the ipsilateral M1 was associated with decreases in both flow and oxygen consumption. Critically, the changes in CMR_{O_2} and CBF, in *both* contra- and ipsilateral regions, were well described by a straight line, with a slope of 0.44±0.04. For the first time, a consistent coupling between perfusion and oxygen consumption changes in response to both net increases and decreases in focal neuronal activity was thus demonstrated. Of particular importance to the range of BOLD applications in neuroscience, these findings support the prediction of a negative BOLD response

in the regions of net decreases of neuronal activity, following hemodynamic and metabolic changes that mirror those commonly found in areas of neuronal activation.

7.2 Future Work

The findings described in this thesis call for a number of future investigations. Given the difficulty of establishing a gold standard for venous cerebral blood volume measurements in vivo in humans (using any modality), the presently described technique is likely best validated using an invasive method, such as contrast enhanced MRI with perfluorocarbons [91,208] or diffuse optical tomography in combination with optical dyes in an animal model. Notwithstanding, the obvious and particularly important application of the VERVE method is the study of blood flow and venous volume coupling under a variety of conditions. First, a graded stimulation paradigm in a sizable cohort of age-matched adult volunteers (in light of known hemodynamic response changes with aging [150,291]) is required to establish a robust model of the steady-state CBF/CBV_v relationship in response to normal functional activation. Second, the extension of such studies to transient conditions is of interest for understanding the details of the hemodynamic response, especially in view of the suggested higher functional specificity of some transient segments of the BOLD response (*e.g.* the initial dip [47]).

The coupling of the flow and venous volume under physiological perturbations, such as hypercapnia or hypoxia is also of interest, not only for the understanding of hemodynamics and BOLD mechanism under these conditions, but also as a validation of the flow/venous volume coupling assumed for the CMR_{O_2} quantification via hypercapnic calibration employed in our and other labs [12,77,155,185,191,337]. Finally, flow/venous volume coupling should also be investigated in cases of known disturbances in the hemodynamic response, such as ischemia, where a decline in the perfusion reserve and a corresponding drop in CBF/CBV ratio has been reported [228,309]. The detailed understanding

of the flow/venous volume coupling under these conditions is particularly significant as it facilitates accurate interpretation of BOLD signal changes in stroke recovery studies [279].

Beyond the study of flow/venous volume coupling, important insight for the understanding of the brain hemodynamics will be reached through investigation of the compartmental contributions to blood volume increases. While arterial volume changes are commonly assumed to make but a small contribution to total BOLD signal relative to the passive venous dilatation [50], a combination of VERVE with one of the new MR methods sensitive to arterial blood volume changes, could be used to test this assumption. Of particular interest here would be the temporal evolution of arterial relative to venous volume changes, the latter thought to lag due to the delayed venous compliance [50, 233]. Methodologically, an investigation of the dynamics in the hemodynamic response calls for a higher signal-to-noise ratio and would thus require VERVE sequence to be implemented at 3 T. This will, in turn, necessitate the presently described relaxometry experiments to be carried out at the higher field strength, to enable the optimization of VERVE sequence parameters at the higher field strength. As an additional benefit, insight into the contributions of different transverse relaxation mechanisms will also be afforded through the study of the field dependence of the transverse relaxation time in blood. Moreover, higher signal-to-noise ratio at higher field strengths may be traded for increased resolution in the steady-state experiments so that the issue of the spatial localization of changes in respective physiological parameters may be addressed, though fields beyond 3 T are likely necessary for those experiments [381, 385]. These questions are central to establishing the functional specificity and ultimate spatial resolution of the BOLD fMRI response.

With respect to the sustained BOLD decreases, an important outstanding question is the relative energetic demand of neuronal excitation *vs.* inhibition [207]. While we have illustrated decreased BOLD signal in the regions of *net decreases* in neuronal activity, it would be particularly interesting to investigate a paradigm that concurrently elicits excitation, inhibition and deactivation (in the projection region of the upregulated inhibitory neurons), ideally in fairly homologous brain regions (thus presumably with very similar

vascular architecture). The relative costs in terms of oxygen consumption as well as the respective CBF and CBV_v changes could then be compared via fMRI methods presently described. Relating these to the degree of modulation in the neuronal activity would, however, necessitate the employment of a concomitant direct measurement of neuronal activity via *e.g.* electrophysiological recordings. Alternatively, a paradigm known to elicit equivalent amounts of up- and downregulation in distinct regions could be employed using fMRI methods alone. From the neurovascular point of view, the observed sustained decreases in CBF relative to baseline call for a study of the corresponding control mechanism. In particular, it is at present not known how a decrease in blood flow from baseline may be mediated in the context of the proposed systems for CBF control (involving a variety of vasodilatory agents [50, 207]).

Finally, negative BOLD responses have been observed under a variety of different conditions. Specifically, the BOLD fMRI signal often decreases in response to normal functional activation in neonates [6, 238, 251]. On the other hand, a decline in the magnitude of the BOLD response and/or activated area with age has been reported [245, 290, 291]. Moreover, sustained BOLD decreases are frequently observed in pathological conditions, *e.g.* epilepsy [2]. The employment of the presently described techniques for direct measurements of metabolic and hemodynamic changes accompanying these BOLD responses would help elucidate the underlying mechanism, critically probing the vascular *vs.* neuronal origins of differences in BOLD fMRI imprints of human brain activity under various conditions.

In vivo imaging of brain function has traditionally been performed using radioactive tracer techniques, such as positron emission tomography (PET), to measure changes in cerebral blood flow, blood volume and the metabolic rates of glucose (CMR_{glu}) or oxygen utilization. However, the detailed and repeated study of subjects using PET is complicated by radiation dose limits as well as limited temporal and spatial resolution. With the development of fMRI during the past decade, most of the *brain mapping* studies now employ this modality, and neuroscience research in this area has expanded prodigiously. As with

PET, fMRI methods do not image neuronal activity directly; instead, they are based on the detection of changes in its various physiological correlates. In the case of BOLD fMRI, the observed signal has a complex and incompletely understood dependence upon CBF, CBV, CMR_{O_2}, and vascular architecture. Although one might thus conjecture that fMRI techniques that measure CBF directly would be preferable, the increased sensitivity and relative technical simplicity of BOLD imaging have resulted in its unequivocal dominance. An important challenge, therefore, is to understand the BOLD signal fully in order to allow its accurate interpretation in normal and diseased brain.

Appendix A

Ethics approval for human studies

The human studies included in this thesis were approved by the Montreal Neurological Institute and Hospital Research Ethics Board. The following document is the confirmation of the approval.

Bibliography

[1] M. Abeles. *Corticonics: Neural Circuits of the Cerebral Cortex.* Cambridge University Press, New York, 1991.

[2] Y Aghakhani, A P Bagshaw, C G Benar, C Hawco, F Andermann, F Dubeau, and J Gotman. fMRI activation during spike and wave discharges in idiopathic generalized epilepsy. *Brain*, 127:1127–44, 2004.

[3] N. Akgoren and M. Lauritzen. Functional recruitment of red blood cells to rat brain microcirculation accompanying increased neuronal activity in cerebellar cortex. *Neuroreport*, 10(16):3257–63, 1999.

[4] J. D. Allison, K. J. Meador, D. W. Loring, R. E. Figueroa, and J. C. Wright. Functional MRI cerebral activation and deactivation during finger movement. *Neurology*, 54:135–142, 2000.

[5] H. An and W. Lin. Impact of intravascular signal on qunatitative measures of cerebral oxygen extraction and blood volume under normo and hypercapnic conditions using an asymmetric spin echo approach. *Magn. Reson. Med.*, 50:708–716, 2003.

[6] AW Anderson, R Marois, ER Colson, BS Peterson, CC Duncan, RA Ehrenkranz, KC Schneider, JC Gore, and LR Ment. Neonatal auditory activation detected by functional magnetic resonance imaging. *Magn Reson Imaging*, 19(1):1–5, 2001.

[7] Anonymous, 2000. www.usm.maine.edu/ psy/broida/101/.

[8] Anonymous. Oxyhemoglobin dissociation curve, 2001. www.rnceus.com/ abgs/ abgcurve.html.

[9] HJ Aronen, IE Gazit, DN Louis, BR Buchbinder, FS Pardo, RM Weisskoff, GR Harsh, GR Cosgrove, EF Halpern, and FH Hochberg et al. Cerebral blood volume maps of gliomas: comparison with tumor grade and histologic findings. *Radiology*, 191(1):41–51, 1994.

[10] HJ Aronen, J Glass, FS Pardo, JW Belliveau, ML Gruber, BR Buchbinder, IE Gazit, RM Linggood, AJ Fischman, and BR Rosen et al. Echo-planar MR cerebral blood volume mapping of gliomas. clinical utility. *Acta Radiol.*, 36(5):520–8, 1995.

[11] O.J. Arthurs and S.J. Boniface. What aspect of the fMRI BOLD signal best reflects the underlying electrophysiology in human somatosensory cortex? *Clinical Neurophysiology*, 114(7):1203–9, 2003.

[12] J D Atkinson, R D Hoge, B Gill, A F Sadikot, and G B Pike. BOLD, CBF, and CMR_{O_2} in the human primary motor cortex. In *Proceedings of the Sixth International Conference on Functional Mapping of the Human Brain*, page S803, San Antonio, 2000.

[13] D. Attwell and S.B. Laughlin. An energy budget for signaling in the grey matter of the brain. *Journal of Cerebral Blood Flow and Metabolism*, 21(10):1133–45, 2001.

[14] L. Axel. Cerebral blood flow determination by rapid-sequence computed tomography: a theoretical analysis. *Radiology*, 137:679–686, 1980.

[15] L. Axel. Tissue mean transit time from dynamic computed tomography by a simple deconvolution technique. *Invest Radiol*, 18:94–99., 1983.

[16] P.A. Bandettini and E.C. Wong. A hypercapnia-based normalization method for improved spatial localization of human brain activation with fMRI. *NMR in Biomedicine*, 10(4-5):197–203, 1997.

[17] J. C. Baron and G. Marchal. Functional imaging in vascular disorders. In J. C. Mazziotta, A. W. Toga, and R. S. J. Frackowiak, editors, *Brain Mapping: the Disorders*, pages 299–316. Academic Press: San Diego, CA, 2000.

[18] M. Barth and E. Moser. Proton NMR relaxation times of human blood samples at 1.5 T and implication for functional MRI. *Cellular and Molecular Biology*, 43(5):783–791, 1997.

[19] R. Bartha, S. Michaeli, H. Merkle, G. Adriany, P. Andersen, W. Chen, K. Ugurbil, and M. Garwood. In vivo H_2O T_2 measurement in the human occipital lobe at 4T and 7T by Carr-Purcell MRI: detection of microscopic susceptibility contrast. *Magn. Reson. Med.*, 47:742–750, 2002.

[20] J. W. Belliveau, D. N. Kennedy Jr., R. C. McKinstry, B. R. Buchbinder, R. M. Weisskoff, M. S. Cohen, J. M. Vevea, T. J. Brady, and B. R. Rosen. Functional mapping of the human visual cortex by magnetic resonance imaging. *Science*, 254(5032):716–9, Nov 1 1991.

[21] J. W. Belliveau, B. R. Rosen, H. Kantor, R. R. Rzedzian, D. N. Kennedy, R. C. McKinstry, J. M. Vevea, M. S. Cohen, I. L. Pykett, and T. J. Brady. Functional cerebral imaging by susceptibility-contrast NMR. *Magn. Reson. Med.*, 14:538–546, 1990.

[22] D. Bereczki, L. Wil, T. Otsuka, F.J. Hans, V. Acuff, C. Patlak, and J. Fenstermacher. Hypercapnia slightly raises blood volume and sizably elevates flow velocity in brain microvesels. *American Journal of Physiology*, 264:H1360–H1369, 1993.

[23] D.E. Bergles and C.E. Jahr. Clearance of glutamate inside the synapse and beyond. *Current Opinion in Neurobiology*, 9:293–8, 1999.

[24] G. Berlucci. Commisurotomy studies in animals. In F. Boller and J. Grafman, editors, *Handbook of Neuropsychology*, volume 4, pages 9–47. Elsevier, Amsterdam, 1990.

[25] J. C. Bezdek, L. O. Hall, and L. P. Clarke. Review of MR image segmentation techniques using pattern recognition. *Med Phys*, 20(4):1033–48, Jul-Aug 1993. Review.

[26] J.M. Bland and D.G. Altman. Statistical methods for assessing agreement between two methods of clinical measurement. *The Lancet*, 8476:307–310, 1986.

[27] M.P. Blaustein. Calcium transport and buffering in neurons. *Trends in Neuroscience*, 11:438–43, 1988.

[28] D.A. Boas, K. Chen, D. Grebert, and M.A. Franceschini. Improving the diffuse optical imaging spatial resolution of the cerebral hemodynamic response to brain activation in humans. *Opt Lett*, 29(13):1506–8, 2004.

[29] D.A. Boas, T. Gaudette, G. Strangman, X. Cheng, J.J. Marota, and J.B. Mandeville. The accuracy of near infrared spectroscopy and imaging during focal changes in cerebral hemodynamics. *Neuroimage*, 13(1):76–90, 2001.

[30] G Bohner, A Forschler, B Hamm, R Lehmann, and R Klingebiel. Quantitative perfusion imaging by multi-slice CT in stroke patients. *Rofo Fortschr Geb Rontgenstr Neuen Bildgeb Verfahr.*, 175(6):806–13, 2003.

[31] B. Boroojerdi, K. Diefenbach, and A. Ferbert. Transcallosal inhibition in cortical and subcortical cerebral vascular lesions. *Journal of Neurological Sciences*, 144:160–170, 1996.

[32] P. A. Bottomley, T. H. Foster, R. E. Argersinger, and L. M. Pfeifer. A review of normal tissue hydrogen NMR relaxation times and relaxation mechanisms from 1-100MHz: dependence on tissue type, NMR frequency, temperature, species, excision, and age. *Med. Phys.*, 11(4):425–448, 1984.

[33] H. L. Boxerman, J. L. Hamberg, B. R. Rosen, and R. M. Weisskoff. MR contrast due to intravascular magnetic susceptibility perturbations. *Magn. Reson. Med.*, 34(4):555–566, 1995.

[34] J. L. Boxerman, P. A. Bandettini, K. K. Kwong, J. R. Baker, T. L. Davis, B. R. Rosen, and R. M. Weisskoff. The intravascular contribution to fMRI signal change: Monte carlo modeling and diffusion-weighted studies in vivo. *Magn. Reson. Med.*, 34(1):4–10, Jul 1995.

[35] R. K. Breger, A. A. Rimm, M. E. Fischer, R. A. Papke, and V. M. Haughton. T_1 and T_2 measurements on a 1.5-T commercial MR imager. *Radiology*, 171:273–276, 1989.

[36] R. K. Breger, F. W. Wehrli, H. C. Charles, J. R. MacFall, and V. M. Haughton. Reproducibility of relaxation and spin-density parameters in phantoms and the human brain measured by MR imaging at 1.5T. *Magn. Reson. Med.*, 3(5):649–662, 1986.

[37] K. M. Brindle, F. F. Brown, I. D. Campbell, C. Grathwohl, and P. W. Kuchel. Application of spin-echo nuclear magnetic resonance to whole-cell systems: membrane transport. *Biochemical Journal*, 180:37–44, 1979.

[38] J. H. Brittain, B. S. Hu, G. A. Wright, C. H. Meyer, A. Macovski, and D. G. Nishamura. Coronary angiography with magnetization-prepared T_2 contrast. *Magn. Reson. Med.*, 33:689–696, 1995.

[39] T. C. Britton, B.-U. Meyer, and R. Benecke. Central motor pathways in patients with mirror movements. *Journal of Neurology and Neurosurgery*, 54:505–510, 1991.

[40] R. A. Brooks and G. DiChiro. Magnetic resonance imaging of stationary blood: a review. *Med. Phys.*, 14:903–913, 1987.

[41] R. A. Brooks, P. Luthert, D. Gadian, and C. D. Marsden. Does signal-attenuation on high-field T_2-weighted MRI of the brain reflect regional cerebral iron deposition? Observations on the relationship between regional cerebral water proton T_2 values and iron levels. *J. Neurol. Neurosurg. Psychiatry.*, 52:108–111, 1989.

[42] R. A. Brooks, J. Vymazal, J. W. M. Bulte, C. D. Baumgarner, and V. Tran. Comparison of T_2 relaxation in blood, brain and ferritin. *J. Magn. Reson. Imaging*, 4:446–450, 1995.

[43] R. A. Brooks, J. Vymazal, R. B. Goldfarb, J. W. M. Bulte, and P. Aisen. Relaxometry and magnetometry of ferritin. *Magn. Reson. Med.*, 40:227–235, 1998.

[44] R.A. Brooks, F. Moiny, and P. Gillis. On T_2 shortening by weakly magnetized particles: the chemical exchange model. *Magn. Reson. Med.*, 45:1014–1020, 2001.

[45] G.G. Brown, L.T. Eyler-Zorrilla, B. Georgy, S.S. Kindermann, E.C. Wong, and R.B. Buxton. BOLD and perfusion response to finger-thumb apposition after acetazolamide administration: differential relationship to global perfusion. *Journal of Cerebral Blood Flow and Metabolism*, 23(7):829–37, 2003.

[46] R. G. Bryant, K. Marill, C. Blackmore, and C. Francis. Magnetic relaxation in blood and blood clots. *Magn. Reson. Med.*, 13:133–144, 1990.

[47] R. B. Buxton. The elusive initial dip. *Neuroimage*, 13:975–987, 2001.

[48] R. B. Buxton and L. R. Frank. A model for the coupling between cerebral blood flow and oxygen metabolism during neural stimulation. *J. Cereb. Bl. Flow Metab.*, 1(17):64–72, Jan 1997.

[49] R B Buxton, E C Wong, and L R Frank. Dynamics of blood flow and oxygenation changes during brain activation: the balloon model. *Magn. Reson. Med.*, 39(6):855–64, 1998.

[50] R.B. Buxton. *Introduction to Functional Magnetic Resonance Imaging*, pages 34–36. Cambridge University Press, 2002.

[51] R.B. Buxton. A hypothesis for cerebral blood flow regulation and the origin of the BOLD effect. In *Proceedings of the Twelfth Annual Meeting of the ISMRM*, page 273, Kyoto, 2004.

[52] K. Caesar, L. Gold, and M. Lauritzen. Context sensitivity of activity-dependent increases in cerebral blood flow. *Proc. Natl. Acad. Sci. USA.*, 100(7):4239–44, 2003.

[53] M.B. Carpenter. *Core text of neuroanatomy*. Baltimore: Williams & Wilkins, 1991.

[54] J. C. Chen, P. A. Hardy, M. Clauberg, J. G. Joshi, J. Parravano, J. H. N. Deck, R. M. Henkelman, L. E. Becker, and W. Kucharczyk. T_2 values in the human brain: comparison with quantitative assays of iron and ferritin. *Radiology*, 173:521–526, 1989.

[55] J. C. Chen, P. A. Hardy, W. Kucharczyk, M. Clauberg, J. G. Joshi, A. Vourlas, M. Dhar, and R. M. Henkelman. MR of human postmortem brain tissue: correlative study between T_2 and assays of iron and ferritin in Parkinson and Huntington disease. *American Journal of Neuroradiological Research*, 14:275–281, 1993.

[56] R. Chen, C. Gerloff, M. Hallett, and L. G. Cohen. Involvement of the ipsilateral motor cortex in finger movements of different complexities. *Annals of Neurology*, 41(2):247–254, 1997.

[57] YC Chen, JB Mandeville, TV Nguyen, A Talele, F Cavagna, and BG Jenkins. Improved mapping of pharmacologically induced neuronal activation using the IRON technique with superparamagnetic blood pool agents. *J. Magn. Reson. Imaging*, 14(5):517–24, 2001.

[58] W.F. Cheong, S.C. Prahl, and A.J. Welch. A review of the optical properties of biological tissues. *IEEE J. Quant. Electron.*, 26:2166–2185, 1990.

[59] C.P. Chih and E.L. Roberts Jr. Energy substrates for neurons during neural activity: a critical review of the astrocyte-neuron lactate shuttle hypothes. *Journal of Cerebral Blood Flow and Metabolism*, 23(11):1263–81, 2003.

[60] Z. H. Cho, Y. M. Ro, and T. H. Lim. NMR venography using the susceptibility effect produced by deoxyhemoglobin. *Magn. Reson. Med.*, 28:25–38, 1992.

[61] I.Y. Choi and R. Gruetter. Effect of deep pentobarbital anesthesia on neurotransmitter metabolism in vivo: on the correlation of total glucose consumption with glutamatergic action. *Journal of Cerebral Blood Flow and Metabolism*, 22(11):1343–51, 2002.

[62] I.Y. Choi, S.P. Lee, S.G. Kim, and R. Gruetter. In vivo measurements of brain glucose transport using the reversible Michaelis-Menten model and simultaneous measurements of cerebral blood flow changes during hypoglycemia. *Journal of Cerebral Blood Flow and Metabolism*, 21(6):653–63, 2001.

[63] I.Y. Choi, E. R. Seaquist, and R. Gruetter. Effect of hypoglycemia on brain glycogen metabolism in vivo. *Journal of Neuroscience Research*, 72(1):25–32, 2003.

[64] N. Cholet, J. Seylaz, P. Lacombe, and G. Bonvento. Local uncoupling of the cerebrovascular and metabolic responses to somatosensory stimulation after neuronal nitric oxide synthase inhibition. *Journal of Cerebral Blood Flow and Metabolism*, 17(11):1191–201, 1997.

[65] M. Cohen. Neuronal anatomy and electrical activity. In *Syllabus of the Educational Courses of the Eleventh Annual Meeting of the ISMRM*, pages A241–A246, Toronto, ON, 2003.

[66] D. L. Collins, P. Neelin, T. M. Peters, and A. C. Evans. Automatic 3D intersubject registration of MR volumetric data in standardized talairach space. *J. Comput. Assist. Tomogr.*, 18(2):192–205, 1994.

[67] T. Conlon and R. Outhred. Water diffusion permeability of erythrocytes using an NMR technique. *Biochim. Biophys. Acta*, 288:354–361, 1972.

[68] D.R. Corfield, K. Murphy, O. Josephs, L. Adams, and R. Turner. Does hypercapnia-induced cerebral vasodilation modulate the hemodynamic response to neural activation? *Neuroimage*, 13(6):1207–11, 2001.

[69] N. Cotillon-Williams, A. L. Williams, K. D. Singh, and A. T. Smith. Negative BOLD reflects attentional modulation, not blood stealing. *Neuroimage Supplement 1*, 19(2):S383, 2003.

[70] R. J. Cox. AFNI: Software for analysis and visualization of functional magnetic resonance neuroimages. *Computers and Biomedical Research*, 29:162–173, 1996.

[71] R.W. Cox. Measuring brain function with MRI: The interaction of physics and physiology, 2001. afni.nimh.nih.gov/afni/doc/edu/mri/.

[72] S.B. Cox, T.A. Woolsey, and C.M. Rovainen. Localized dynamic changes in cortical blood flow with whisker stimulation corresponds to matched vascular and neuronal architecture of rat barrels. *Journal of Cerebral Blood Flow and Metabolism*, 13(6):899–913, 1993.

[73] M. Cuenod, K. Do, and G. Grima. Nitric oxide synthesis and arginine transfer from glia to neurons. In R. S. J. Frackowiak, P. J. Magistretti, R. G. Shulma, J. S. Altman, and M. Adams, editors, *Neuroenergetics: relevance for functional brain imaging*, pages 169–172. Human Frontier Science Program: Strasbourg, 2001.

[74] JP Culver, T Durduran, D Furuya, C Cheung, JH Greenberg, and AG Yodh. Diffuse optical tomography of cerebral blood flow, oxygenation, and metabolism in rat during focal ischemia. *J Cereb Blood Flow Metab*, 23(8):911–24, 2003.

[75] C. G. Cusick and J Kaas. Interhemispheric connections of cortical sensory and motor representations in primates. In F. Lepore, M. Ptito, and H. H. Jasper, editors, *Two hemispheres - one brain: functions of the corpus callosum*, pages 83–102. Liss, New York, 1986.

[76] Z. J. Daskalakis, B. K. Christensen, P. B. Fitzgerald, L. Roshan, and R. Chen. The mechanisms of interhemispheric inhibition in the human motor cortex. *Journal of Physiology*, 543(1):317–326, 2002.

[77] T.L. Davis, K.K. Kwong, R.M. Weisskoff, and B.R. Rosen. Calibrated functional MRI: Mapping the dynamics of oxidative metabolism. *Proceedings of the National Academy of Sciences of the United States of America*, 95:1834–1839, 1998.

[78] CP Derdeyn, TO Videen, KD Yundt, SM Fritsch, DA Carpenter, RL Grubb, and WJ Powers. Variability of cerebral blood volume and oxygen extraction: stages of cerebral haemodynamic impairment revisited. *Brain*, 125(3):595–607, 2002.

[79] C. Dettmers, G. R. Fink, R. N. Lemon, K. M. Stephan, R. E. Passingham, D. Silbersweig, A. Holmes, M. C. Ridding, D. J. Brooks, and S. J. Frackowiak. Relation between cerebral activity and force in the motor areas of the human brain. *Journal of Neurophysiology*, 74(2):802–815, 1995.

[80] A. Devor, A.K. Dunn, M.L. Andermann, I. Ulbert, D.A. Boas, and A.M. Dale. Coupling of total hemoglobin concentration, oxygenation, and neural activity in rat somatosensory cortex. *Neuron*, 39(2):353–359, 2003.

[81] U. Dirnagl, K. Niwa, U. Lindauer, and A. Villringer. Coupling of cerebral blood flow to neuronal activation: Role of adenosine and nitric oxide. *American Journal of Physiology*, 267:H296–301, 1994.

[82] M. Dojat, J. Warnking, and C. Segebarth. Detection at 1.5T of sustained negative BOLD signal in the human visual cortex during partial visual field stimulation. *Neuroimage Supplement 1*, 19(2):S282, 2003.

[83] B. Drayer, P. Burger, R. Darwin, S. Riederer, R. Herfkens, and G.A. Johnson. MRI of brain iron. *AJR Am. J. Roentgenol.*, 147:103–110, 1986.

[84] J.P. Dreier, K. Korner, A. Gorner, U. Lindauer, M. Weih, A. Villringer, and U. Dirnagl. Nitric oxide modulates the CBF response to increased extracellular potassium. *Journal of Cerebral Blood Flow and Metabolism*, 15(6):914–9, 1995.

[85] R. O. Duda and P. E. Hart. *Pattern Recognition And Scene Analysis*. Wiley, New York, 1973.

[86] R. Duelli and Kuschinsky W. Changes in brain capillary diameter during hypocapnia and hypercapnia. *Journal of Cerebral Blood Flow and Metabolism*, 13:1025–1028, 1993.

[87] F. H. Duffy and J. L. Burchfiel. Eye movement-related inhibition of primate visual neurons. *Brain Research*, 89:121–132, 1975.

[88] A.K. Dunn, A. Devor, H. Bolay, M.L. Andermann, M.A. Moskowitz, A.M. Dale, and D.A. Boas. Simultaneous imaging of total cerebral hemoglobin concentration, oxygenation, and blood flow during functional activation. *Opt Lett*, 28(1):28–30, 2003.

[89] J.F. Dunn, M.A. Roche, R. Springett, M. Abajian, J. Merlis, C.P. Daghlian, S.Y. Lu, and M. Makki. Monitoring angiogenesis in brain using steady-state quantification of $\delta r2$ with mion infusion. *mrm*, 51(1):55–61, 2004.

[90] T.Q. Duong, D.S. Kim, K. Ugurbil, and S.G. Kim. Localized cerebral blood flow response at submillimeter columnar resolution. *Proc. Natl. Acad. Sci. USA.*, 98(19):10904–9, 2001.

[91] T.Q. Duong and S.-G. Kim. In vivo MR measurements of regional arterial and venous blood volume fractions in intact rat brain. *Magn. Reson. Med.*, 43:393–402, 2000.

[92] L. Edvinsson, E.T. MacKenzie, and J. McCulloch. *Cerebral blood flow and metabolism*. Raven Press, New York, 1993.

[93] R. Ellinger, C. Kremser, M. F. Schocke, C. Kolbitsch, J. Griebel, S. R. Felber, and F. T. Aichner. The impact of peak saturation of the arterial input function on quantitative evaluation of dynamic susceptibility contrast-enhanced MR studies. *Journal of Computed Assisted Tomography*, 24(6):942–948, 2000.

[94] C.E. Elwell, M. Cope, A.D. Edwards, J.S. Wyatt, D.T. Delpy, and E.O.R. Reynolds. Quantification of adult cerebral hemodynamics by near-infrared spectroscopy. *J. Appl. Physiol.*, 77:2753–2760, 1994.

[95] M. Erecinska and I.A. Silver. Metabolism and role of glutamate in mammalian brain. *Progress in Neurobiology*, 35:245–96, 1990.

[96] A. C. Evans, D. L. Collins, S. R. Mills, E. D. Brown, R. L. Kelly, and T. M. Peters. 3D statistical neuroanatomical models from 305 MRI volumes. In *Proceedings of IEEE-Nuclear Science Symposium and Medical Imaging Conference*, pages 1813–1817, 1993.

[97] PF Fabene, P Marzola, A Sbarbati, and M Bentivoglio. Magnetic resonance imaging of changes elicited by status epilepticus in the rat brain: diffusion-weighted and T_2-weighted images, regional blood volume maps, and direct correlation with tissue and cell damage. *Neuroimage*, 18(2):375–89, 2003.

[98] R. Fahraeus. The suspension stability of the blood. *Physiol. Rev.*, 9:241–274, 1929.

[99] F. R. E. Fenrich, C. Beaulieu, and P. S. Allen. Relaxation times and microstructures. *NMR Biomed.*, 14:133–139, 2001.

[100] J. Fenstermacher, H. Nakata, A. Tajima, S.Z. Lin, T. Otsuka, V. Acuff, L. Wei, and D. Bereczki. Functional variations in parenchymal microvascular systems within the brain. *Magn. Reson. Med.*, 19(2):217–20, 1991.

[101] J.D. Fenstermacher. The flow of water in the blood-brain-cerebrospinal fluid system. In *Syllabus of SMRM FMRI Workshop*, pages 9–17, Arlington, VA, 1993.

[102] J.D. Fenstermacher and S.I. Rapoport. Blood-brain barrier. In E.M. Renkin and C.C. Michel, editors, *Handbook oh physiology*, chapter 21. American Physiological Society, Bethesda, MD, 1984.

[103] A. Ferbert, J. C. Rothwell, B. L. Day, J. G. Colebatch, and C. D. Marsden. Interhemispheric inhibition of the human motor cortex. *Journal of Physiology*, 453(1):525–546, 1992.

[104] J. C. Ferrie, L. Barantin, E. Saliba, S. Akoka, F. Tranquart, D. Sirinelli, and L. Pourcelot. MR assessment of the brain maturation during the perinatal period: quantitative T_2 MR study in premature newborns. *Magn. Reson. Imaging*, 17(9):1275–1288, 1999.

[105] D Fiorella, J Heiserman, E Prenger, and S Partovi. Assessment of the reproducibility of postprocessing dynamic CT perfusion data. *AJNR Am J Neuroradiol.*, 25(1):97–107, 2004.

[106] P. T. Fox and M. E. Raichle. Focal physiological uncoupling of cerebral blood flow and oxidative metabolism during somatosensory stimulation in human subjects. *Proceedings of the National Academy of Sciences of the United States of America*, 83(4):1140–4, Feb 1986.

[107] P. T. Fox, M. E. Raichle, M. A. Mintun, and C. Dence. Nonoxidative glucose consumption during focal physiologic neural activity. *Science*, 241(4864):462–4, Jul 22 1988.

[108] P.T. Fox, M.A. Mintun, M.E. Raichle, F.M. Miezin, J.M. Allman, and D.C. Van Essen. Mapping human visual cortex with positron emission tomography. *Science*, 323(6091):806–809, 1986.

[109] M.A. Franceschini, S. Fantini, J.H. Thompson, J.P. Culver, and D.A. Boas. Hemodynamic evoked response of the sensorimotor cortex measured noninvasively with near-infrared optical imaging. *Psychophysiology*, 40(4):548–60, 2003.

[110] S.T. Francis, J.A. Pears, S. Butterworth, R.W. Bowtell, and P.A. Gowland. Measuring the change in CBV upon cortical activation with high temporal resolution using Look Locker EPI and GdDTPA. *Magn. Reson. Med.*, 50:483–492, 2003.

[111] J.A. Frank, V.S. Massay, J. Duyn, G. Soberin, F.A. Barrios, J. Zigun, R. Sexton, P. Kwok, J. Woo, C. Moonen, and D.R. Weinberger. Measurement of relative cerebral blood volume changes with visual stimulation by double dose gadopentate dimeglumine enhanced dynamic magnetic resonance imaging. *Investigative Radiology*, 29:S157–S160, 1994.

[112] J.R. Fromm. Oxidation of glucose, 1997. www.3rd1000.com/ chem301/ chem302x.htm.

[113] R.D. Frostig, E.E. Lieke, D.Y. Tso, and A. Grinvald. Cortical functional architecture and local coupling between neuronal activity and the microcirculation revealed by in vivo high-resolution optical imaging. *Proceedings of the National Academy of Sciences of the United States of America*, 87(16):6082–6086, 1990.

[114] C. Gasparovic and N.A. Matwiyoff. The magnetic properties and water dynamics of the red blood cell: a study by proton NMR lineshape analysis. *Magn. Reson. Med.*, 26:274–299, 1992.

[115] G. M. Geffen, D. L. Jones, and L. B. Geffen. Interhemispheric control of manual motor activity. *Behavioural Brain Research*, 64:131–140, 1994.

[116] N. Gelman, J. M. Gorell, P. B. Barker, R. M. Savage, E. M. Spickler, J. P. Windham, and R. A. Knight. MR imaging of human brain at 3.0T: preliminary report on transverse relaxation rates and relation to estimated iron content. *Radiology*, 210:759–767, 1999.

[117] C. S. Georgiades, R. Itoh, X. Golay, P. C. M. van Zijl, and E. R. Melhem. MR imaging of the human brain at 1.5T: regional variations in transverse relaxation rates in the cerebral cortex. *AJNR Am. J. Neuroradiol.*, 22:1732–1737, 2001.

[118] C. Gerloff, L. G. Cohen, M. K. Floeter, R. Chen, B. Corwell, and M. Hallett. Inhibitory influence of the ipsilateral motor cortex on responses to stimulation of the human cortex and pyramidal tract. *Journal of Physiology*, 510(1):249–259, 1998.

[119] K. Gersonde, T. Tolxdorff, and L. Felserg. Identification and characterization of tissues by T_2-selective whole-body proton NMR imaging. *Magn. Reson. Med.*, 2(4):390–401, 1985.

[120] P. Gillis, S. Peto, F. Moiny, J. Mispelter, and C.-A. Cuenod. Proton transverse nuclear magnetic relaxation in oxidized blood: a numerical approach. *Magn. Reson. Med.*, 33:93–100, 1995.

[121] P. S. Gillis and H. Koenig. Transverse relaxation of solvent protons induced by magnetized spheres: application to ferritin, erythrocytes, and magnetite. *Magn. Reson. Med.*, 5:323–345, 1987.

[122] M.D. Ginsberg, J.Y. Chang, R.E. Kelley, F. Yoshii, W.W. Barker, G. Ingenito, and T.E. Boothe. Increases in both cerebral glucose utilization and blood flow during execution of a somatosensory task. *Annals of Neurology*, 23(2):152–60, 1988.

[123] A. Gjedde. High- and low-affinity transport of D-glucose from blood to brain. *Journal of Neurochemistry*, 36:1463–1471, 1981.

[124] A. Gjedde. Does deoxyglycose uptake in the brain reflect energy metabolism ? *Biochemical Pharmacology*, 36:1853–61, 1987.

[125] A. Gjedde. Coupling and compartmentalization of cerebral blood flow and metabolism. In R.S.J. Frackowiak, P.J. Magistretti, R.G. Shulman, J.S. Altman, and M. Adams, editors, *Neuroenergetics: relevance for functional brain imaging*, pages 160–169. HFSP, Strasbourg, 2001.

[126] A. Gjedde. Brain energy metabolism and the physiological basis of the hemodynamic response. In P. Jezzard, P.M. Matthews, and S. Smith, editors, *Functional magnetic resonance imaging - an introduction to methods*, pages 37–65. Oxford University Press, New York, 2003.

[127] A. Gjedde, S. Ohta, H. Kuwabara, and E. Meyer. Is oxygen diffusion limiting for blood-brain transfer of oxygen? In N.A. Lassen, D.H. Ingvar, M.E. Raichle, and L. Friberg, editors, *Brain Work and Energy Metabolism*, pages 177–184, Copenhagen, 1991. Munskgaard.

[128] U Gobel, B Klein, H Schrock, and W Kuschinsky. Lack of capillary recruitment in the brains of awake rats during hypercapnia. *J Cereb Blood Flow Metab.*, 9(4):491–9, 1989.

[129] U Gobel, H Theilen, and W Kuschinsky. Congruence of total and perfused capillary network in rat brains. *Circ Res.*, 66(2):271–81, 1990.

[130] X. Golay, M. J. Silvennoinen, J. Zhou, C. S. Clingman, R. A. Kauppinen, J. J. Pekar, and P. C. M. van Zijl. Measurement of tissue oxygen extraction ratios from venous blood T_2: increased precision and validation of principle. *Magn. Reson. Med.*, 46:282–291, 2001.

[131] J.M. Gomori, R.I. Grossman, C. Yu-Ip, and T. Asakura. NMR relaxation times of blood: dependence on field strength, oxidation state, and cell integrity. *Journal of Computed Assisted Tomography*, 11(4):684–690, 1987.

[132] J. Gotoh, T.Y. Kuang, Y. Nakao, D.M. Cohen, P. Melzer, Y. Itoh, H. Pak, K. Pettigrew, and L. Sokoloff. Regional differences in mechanisms of cerebral circulatory response to neuronal activation. *American Journal of Physiology. Heart and Circulatory Physiology*, 280(2):H821–9, 2001.

[133] H. J. Gould, C. G. Cusick, T. P. Pons, and J. H. Kaas. The relationship of corpus callosum connections to electrical stimulation maps of motor, supplementary motor, and the frontal eye fields in owl monkeys. *Journal of Comparative Neurology*, 247(3):297–325, 1986.

[134] R. Greenbaum, J.F. Nunn, C. Prys-Roberts, and G.R. Kelman. Metabolic changes in whole human blood (in vitro) at 37°C. *Respiration Physiology*, 2:274–282, 1967.

[135] R.L. Grubb, M.E. Phelps, and J.O. Eichling. The effects of vascular changes in Pa_{CO_2} on cerebral blood volume, blood flow and vascular mean transit time. *Stroke*, 5:630–639, 1974.

[136] RL Grubb, ME Raichle, CS Higgins, and JO Eichling. Measurement of regional cerebral blood volume by emission tomography. *Ann Neurol.*, 4(4):322–8, 1978.

[137] R. Gruetter, E.R. Seaquist, and K. Ugurbil. A mathematical model of compartmentalized neurotransmitter metabolism in the human brain. *American journal of physiology. Endocrinology and metabolism*, 281(1):E100–12, 2001.

[138] R. Gruetter, K. Ugurbil, and E.R. Seaquist. Steady-state cerebral glucose concentrations and transport in the human brain. *Journal of neurochemistry*, 70(1):397–408, 1998.

[139] A.C. Guyton and J.E. Hall. *Textbook of Medical Physiology*. W.B. Saunders Company, Philadelphia, 1996.

[140] B. Hallgren and P. Sourander. The efect of age on the non-haemin iron in the human brain. *J. Neurochem.*, 3:41–51, 1958.

[141] LM Hamberg, GJ Hunter, EF Halpern, B Hoop, GS Gazelle, and GL Wolf. Quantitative high-resolution measurement of cerebrovascular physiology with slip-ring ct. *AJNR*, 17:639–650, 1996.

[142] F. Hamzei, C. Dettmers, R. Rzanny, J. Liepert, C. Buechel, and C. Weiller. Reduction of excitability ("inhibition") in the ipsilateral primary motor cortex is mirrored by fMRI signal decreases. *Neuroimage*, 17:490–496, 2002.

[143] P. A. Hardy and R. M. Henkelman. Transverse relaxation rate enhancement caused by magnetic particulates. *Magn. Reson. Imaging*, 7:265–275, 1989.

[144] N. Harel, S.-L. Lee, T. Nagaoka, D.-S. Kim, and S.-G. Kim. Origin of negative blood oxygenation level-dependent fMRI signals. *Journal of Cerebral Blood Flow and Metabolism*, 22:908–917, 2002.

[145] RV Harrison, N Harel, J Panesar, and RJ Mount. Blood capillary distribution correlates with hemodynamic-based functional imaging in cerebral cortex. *Cereb Cortex*, 12(3):225–33, 2002.

[146] D.J. Heeger and D. Ress. What does fMRI BOLD tell us about neuronal activity. *Nature Reviews Neuroscience*, 3(2):142–51, 2002.

[147] D.D. Heistad and H.A. Kontos. Cerebral circulation. In J.T. Shepard and F.M. Abboud, editors, *Handbook of Physiology*, volume III, section 2. American Physiological Society, Bethesda, MD, 1983.

[148] M. D. Herbst and J. H. Goldstein. A review of water diffusion measurement by NMR in red blood cells. *American Journal of Physiology*, 256:C1097–C1104, 1989.

[149] T. Hirai, Y. Korogi, Y. Sakamoto, S. Hamatake, I. Ikushima, and M. Takahashi. T_2 shortening in the motor cortex: effect of aging and cerebrovascular diseases. *Radiology*, 199:799–803, 1996.

[150] C Hock, F Muller-Spahn, S Schuh-Hofer, M Hofmann, U Dirnagl, and A Villringer. Age dependency of changes in cerebral hemoglobin oxygenation during brain activation: a near-infrared spectroscopy study. *J Cereb Blood Flow Metab*, 15(6):1103–8, 1995.

[151] A. Hoeck, U. Demmel, H. Schicha, K. Kasperek, and L.E. Feinendegen. Trace element concentration in human brain. *Brain*, 98:49–64, 1975.

[152] EG Hoeffner, I Case, R Jain, SK Gujar, GV Shah, JP Deveikis, RC Carlos, BG Thompson, MR Harrigan, and SK Mukherji. Cerebral perfusion CT: technique and clinical applications. *Radiology*, 231(3):632–44, 2004.

[153] R D Hoge, J Atkinson, B Gill, G R Crelier, S Marrett, and G B Pike. Additive combination of perfusion responses to hypercapnia and visual stimulation. In *Proceedings of the International Society of Magnetic Resonance in Medicine*, page 1737, Philadelphia, 1999.

[154] R D Hoge, J Atkinson, B Gill, G R Crelier, S Marrett, and G B Pike. Additive combination of perfusion responses to hypercapnia and visual stimulation. In *Proceeding of the Fifth International Conference on Functional Mapping of the Human Brain*, pages NeuroImage, 9(6), s306, Dusseldorf, GDR, 1999.

[155] R. D. Hoge, J. Atkinson, B. Gill, G.R. Crelier, S. Marrett, and G.B. Pike. Investigation of BOLD signal dependence on CBF and CMR_{O_2}: the deoxyhemoglobin dilution model. *Magn. Reson. Med.*, 42(5):849–863, 1999.

[156] R.D. Hoge, M.A. Franceschini, C. Warmuth, K. Scott, R. Covolan, J. Mandeville, and D. Boas. Simultaneous recording of task-induced changes in blood oxygenation, volume and flow using diffuse optical imaging and arterial spin-labelling MRI. *Neuroimage S1*, 19(2):289, 2003.

[157] F. G. C. Hoogenraad, J. R. Reichenbach, E. M. Haacke, S. Lai, K. Kuppusamy, and M. Sprenger. In vivo measurement of changes in venous blood-oxygenation with high resolution functional MRI at 0.95 Tesla by measuring changes in susceptibility and velocity. *Magn. Reson. Med.*, 39:97–107, 1998.

[158] F.G. Hoogenraad, P.J. Pouwels, M.B. Hofman, J.R. Reichenbach, M. Sprenger, and E.M. Haacke. Quantitative differentiation between BOLD models in fMRI. *Magn. Reson. Med.*, 45(2):233–46, 2001.

[159] A. Hopt, F. Blankenburg, R. Wenzel, and A. Villringer. Negative BOLD-signal changes are associated with a decrease in perfusion measurable by an UNFAIR-sequence. In *Proceedings of the Eleventh Annual Meeting of the ISMRM*, page 1799, Toronto, 2003.

[160] P. Hopton, T.S. Walsh, and A. Lee. Measurement of cerebral blood volume using near-infrared spectroscopy and indocyanine green elimination. *J Appl Physiol.*, 87(5):1981–7, 1999.

[161] N. Horinaka, N. Artz, J. Jehle, S. Takahashi, C. Kennedy, and L. Sokoloff. Examination of potential mechanisms in the enhancement of cerebral blood flow by hypoglycemia and pharmacological doses of deoxyglucose. *Journal of Cerebral Blood Flow and Metabolism*, 17(1):54–63, 1997.

[162] F. Hyder, I. Kida, R.P. Kennan, and D.L. Rothman. CBV changes during functional and CO_2 challenges: implication for BOLD calibration. In *Proceedings of the Ninth Annual Meeting of the ISMRM*, page 281, Glasgow, 2001.

[163] F. Hyder, R.G. Shulman, and D.L. Rothman. A model for the regulation of cerebral oxygen delivery. *J. Appl. Phys.*, 85:554–564, 1998.

[164] C. Iadecola. Regulation of cerebral microciculation during neural activity: is nitric oxide the missing link. *Trends in Neurosciences*, 16:206–214, 1993.

[165] H. Iida. Quantitative assessment of CBF and $CMRO_2$ using PET. In R.S.J. Frackowiak, P.J. Magistretti, R.G. Sholman, J.S. Altman, and M. Adams, editors, *Neuroenergetics: relevance for functional brain imaging*, pages 71–81. HFSP, Strasbourg, 2001.

[166] H. Iida, T. Jones, and S. Miura. Modeling approach to eliminate the need to separate arterial plasma in oxygen-15 inhalation positron emission tomography. *Journal of Nuclear Medicine*, 34:1333–1340, 1993.

[167] H. Iida, I. Law, B. Pakkenberg, A. Krarup-Hansen, S. Eberl, S. Holm, A.K. Hansen, H.J. Gundersen, C. Thomsen, C. Svarer, P. Ring, L. Friberg, and O.B. Paulson. Quantitation of regional cerebral blood flow corrected for partial volume effect using O-15 water and PET: I. theory, error analysis, and stereologic comparison. *Journal of Cerebral Blood Flow and Metabolism*, 20(8):1237–51, 2000.

[168] D.H. Ingvar, B. Sjolund, and A. Ardo. Correlation between dominant EEG frequency, cerebral oxygen uptake and blood flow. *Electroencephalography and clinical neurophysiology*, 41(3):268–76, 1976.

[169] H. Ito, I. Kanno, M. Ibaraki, J. Hatazawa, and S. Miura. Changes in human cerebral blood flow and cerebral blood volume during hypercapnia and hypocapnia measured by positron emission tomography. *Journal of Cerebral Blood Flow and Metabolism*, 23:665–670, 2003.

[170] H Ito, I Kanno, H Iida, J Hatazawa, E Shimosegawa, H Tamura, and T Okudera. Arterial fraction of cerebral blood volume in humans measured by positron emission tomography. *Ann Nucl Med*, 15(2):111–6, 2001.

[171] H. Ito, K. Takahashi, J. Hatazawa, S.-G. Kim, and I. Kanno. Changes in human regional cerebral blood flow and cerebral blood volume during visual stimulation measured by positron emission tomography. *Journal of Cerebral Blood Flow and Metabolism*, 21:608–6128, 2001.

[172] J. H. Jensen and R. Chandra. NMR relaxation in tissues with weak magnetic inhomogeneities. *Magn. Reson. Med.*, 44:144–156, 2000.

[173] J. H. Jensen and R. Chandra. Strong filed behaviour of the NMR signal from magnetically heterogeneous tissues. *Magn. Reson. Med.*, 43:226–236, 2000.

[174] J. H. Jensen, R. Chandra, and H. Yu. Quantitative model for the interecho time dependence of the CPMG relaxation rate in iron-rich gray matter. *Magn. Reson. Med.*, 46:159–165, 2001.

[175] X. Jiao and R.G. Bryant. Noninvasive measurement of protein concentration. *Magn. Reson. Med.*, 35:159–161, 1996.

[176] G.B. Johnson. The synapse and drug addiction, 2003. www.txtwriter.com/Backgrounders/Drugaddiction/drugs1.html.

[177] P.C. Johnson. Principles of circulatory control. In P.C. Johnson, editor, *Peripheral Circulation*, pages 34–48. Wiley, New York, 1978.

[178] A.W. Jones, R.G. Hahn, and H.P. Stalberg. Distribution of ethanol and water between plasma and whole blood; inter- and intra-individual variations after administration of ethanol by intravenous infusion. *Scandinavian journal of clinical and laboratory investigation*, 50:775–780, 1990.

[179] M. Jones, J. Berwick, and J. Mayhew. Changes in blood flow, oxygenation, and volume following extended stimulation of rodent barrel cortex. *Neuroimage*, 15:474–487, 2002.

[180] M. Jones, N. Hewson-Stoate, J. Martindale, Redgrave P., and J. Mayhew. Nonlinear coupling of neural activity and CBF in rodent barrel cortex. *Neuroimage*, 22(2):956–65, 2004.

[181] K. Kacem, P. Lacombe, J. Seylaz, and G. Bonvento. Structural organization of the perivascular astrocyte endfeet and their relationship with the endothelial glucose transporter: a confocal microscopy study. *Glia*, 23(1):1–10, 1998.

[182] M. Kadekaro, A.M. Crane, and L. Sokoloff. Differential effects of electrical stimulation of sciatic nerve on metabolic activity in spinal cord and dosal root ganglion in the rat. *Proc. Natl. Acad. Sci. USA.*, 82:6010–13, 1985.

[183] K.A. Kasischke, H.D. Vishwasrao, P.J. Fisher, W.R. Zipfel, and W.W. Webb. Neural activity triggers neuronal oxidative metabolism followed by astrocytic glycolysis. *Science*, 305:99–103, 2004.

[184] I.G. Kassissia, C.A. Goresky, C.P. Rose, A.J. Schwab, A. Simard, P.M. Huet, and G.G. Bach. Tracer oxygen distribution is barrier-limited in the cerebral microcirculation. *Circulation Research*, 77(6):1201–11, 1995.

[185] A. Kastrup, G. Krueger, T. Neumann-Haefelin, G. Glover, and M. E. Moseley. Changes of cerebral blood flow, oxygenation and oxidative metabolism during graded motor activation. *Neuroimage*, 15:74–82, 2002.

[186] I. Kay and R.M. Henkelman. Practical implementation and optimization of one-shot T_1 imaging. *Magn. Reson. Med.*, 22:414–424, 1991.

[187] SM Kealey, VA Loving, DM Delong, and JD Eastwood. User-defined vascular input function curves: influence on mean perfusion parameter values and signal-to-noise ratio. *Radiology*, 231(2):587–93, 2004.

[188] C. Kennedy, M.H.D. Rosiers, O. Sakurada, M. Shinohara, M. Reivich, J.W. Jehle, and L. Sokoloff. Metabolic mapping of the primary visual system of the monkey by means of the autoradiographic [14C]deoxyhemoglobin technique. *Proc. Natl. Acad. Sci. USA.*, 73:4230–4, 1976.

[189] A. Keyeux, D. Ochrymowicz-Bemelmans, and A.A. Charlier. Induced response to hypercapnia in the two-compartment total cerebral blood volume: influence on brain vascular reserve and flow efficiency. *Journal of Cerebral Blood Flow and Metabolism*, 15:1121–1131, 1995.

[190] D.S. Kim, I. Ronen, C. Olman, S.-G. Kim, K. Ugurbil, and L.J. Toth. Spatial relationship between neuronal activity and BOLD functional MRI. *Neuroimage*, 21:876–885, 2004.

[191] S.-G. Kim, E. Rostrup, H. B. Larsson, S. Ogawa, and O. B. Paulson. Determination of relative CMR_{O2} from CBF and BOLD changes: significant increase of oxygen consumption rate during visual stimulation. *Magn. Reson. Med.*, 41(6):1152–1161, 1999.

[192] M.W. King and S. Marchesini. Myoglobin and hemoglobin, 2002. www.med.unibs.it/ marchesi/hemoglob.html.

[193] V.G. Kiselev and S. Posse. Analytical model of susceptibility-induced MR signal dephasing: effect of diffusion in a microvascular network. *Magn. Reson. Med.*, 41:499–509, 1999.

[194] V.G. Kiselev and S. Posse. Analytical theory of susceptibility induced NMR signal dephasing in a cerebrovascular network. *Physical Review Letters*, 81(25):5696–5699, 1999.

[195] B Klein, W Kuschinsky, H Schrock, and F Vetterlein. Interdependency of local capillary density, blood flow, and metabolism in rat brains. *Am J Physiol.*, 251(6):H1333–40, 1986.

[196] S. Kobayashi, A.G. Waltz, and A.L. Rhoton. Effects of stimulation of cervical sympathetic nerves on cortical blood flow and vascular reactivity. *Neurology*, 23:297–302, 1971.

[197] V. Kollokian. Performance analysis of automatic techniques for tissue classification in MRI of the human brain. Master's thesis, Concordia University, Montreal, Canada, November 1996.

[198] R. Kristeva, D. Cheyne, and L. Deecke. Neuromagnetic fields accompanying unilateral and bilateral voluntary movements: topography and analysis of cortical sources. *Electroencephalographical Clinical Neurophysiology*, 81:284–298, 1991.

[199] K. Krnjevic, M. Randic, and D. W. Straughan. Nature of a cortical inhibitory process. *Journal of Physiology*, 184:49–77, 1966.

[200] K. K. Kwong, J. W. Belliveau, D. A. Chesler, I. E. Goldberg, R. M. Weisskoff, B. P. Poncelet, D. N. Kennedy, B. E. Hoppel, M. S. Cohen, and R. Turner. Dynamic magnetic resonance imaging of human brain activity during primary sensory stimulation. *Proceedings of the National Academy of Sciences of the United States of America*, 89(12):5675–9, Jun 15 1992.

[201] C.S. Landis, X. Li, F. Telang, P.E. Molina, I. Palyka, G. Vetek, and C.S. Jr. Springer. Equilibrium transcytolemmal water exchange kinetics in skeletal muscle in vivo. *Magn. Reson. Med.*, 42:467–478, 1999.

[202] E. M. Larsson, E. Englund, Z. Gyorffy-Wagner, A. Brun, S. Cronqvist, and B. Persson. Regional differences in the proton magnetic resonance relaxation times T_1 and T_2 within the normal human brain. *Acta Radiol. Diagnosis*, 27:231–234, 1986.

[203] N. A. Lassen. Cations as mediators of functional hyperemia in the brain. In N. A. Lassen, D. H. Ingvar, M. E. Raichle, and L. Friberg, editors, *Brain work and mental activity: quantitative studies with radioactive tracers*, pages 68–77. Munksgsaard: Copenhagen, 1991.

[204] N.A. Lassen. Cerebral blood flow and oxygen consumption in man. *Physiological Reviews*, 39:183–238, 1959.

[205] N.A. Lassen. Brain. In P.C. Johnson, editor, *Peripheral Circulation*. Wiley, New York, 1978.

[206] M. Lauritzen. Heterogeneity of smooth muscle associated proteins in mammalian brain microvasculature. *Cell Tissue Research*, 279:393–403, 1995.

[207] M. Lauritzen. Relationship of spikes, synaptic activity, and local changes of cerebral blood flow. *Journal of Cerebral Blood Flow and Metabolism*, 21:1367–1383, 2001.

[208] S. Lee, T. Q. Duong, G. Yang, C. Iadecola, and Kim S.-G. Relative changes of cerebral arterial and venous blood volumes during increased cerebral blood flow: implications for BOLD fMRI. *Magn. Reson. Med.*, 45:791–800, 2001.

[209] T. Lee, J.A. Stainsby, J. Hong, E. Han, J. Brittain, and G.A. Wright. Blood relaxation properties at 3T - effects of blood oxygen saturation. In *Proceedings of the Eleventh Annual Meeting of the ISMRM*, page 131, 2003.

[210] K.L. Leenders, D. Perani, A.A. Lammartsma, J.D. Heather, P. Buckingham, M.J.R. Healy, J.M. Gibbs, R.J.S. Wise, J. Hatazawa, S. Herold, R.P. Beaney, D.J. Brooks, T. Spinks, C. Rhodes, R.S.J. Frac kowiak, and T. Jones. Cerebral blood flow, blood volume and oxygen utilization. *Brain*, 113:27–47, 1990.

[211] F.D. Leite, W. Vanduffel, L. Wald, A. Dale, K. Kwong, B. Rosen, R. Tootell, and J. Mandeville. Spatio-temporal analysis of BOLD and CBV fMRI in awake, behaving macaques at 3 Tesla. In *Proceedings of the Tenth Annual Meeting of the ISMRM*, page 645, Honolulu, 2002.

[212] E. Leniger-Follert and D.W. Lubbers. Behavior of microflow and local p_{O_2} of the brain cortex during and after direct electrical stimulation. A contribution to the problem of metabolic regulation of microcirculation in the brain. *Pflugers Archiv*, 366(1):39–44, 1976.

[213] L. Leocani, L. G. Cohen, E. M. Wassermann, K. Ikoma, and M. Hallett. Human corticospinal excitability evaluated with transcranial magnetic stimulation during different reaction time paradigms. *Brain*, 123:1161–1173, 2000.

[214] RL Levine, JA Dobkin, JM Rozental, MR Satter, and RJ Nickles. Blood flow reactivity to hypercapnia in strictly unilateral carotid disease: preliminary results. *J Neurol Neurosurg Psychiatry*, 54(3):204–9, 1991.

[215] M. H. Levitt, R. Freeman, and T. Frenkiel. Broadband decoupling in high-resolution nuclear magnetic resonance spectroscopy. *Advances in Magnetic Resonance*, 11:47–110, 1983.

[216] T.-Q. Li, T. N. Haefelin, B. Chan, A. Kastrup, T. Jonsson, G. H. Glover, and M.E. Moseley. Assessment of hemodynamic response during focal neural activity in human using bolus tracking, arterial spin labeling and BOLD techniques. *Neuroimage*, 12:442–451, 2000.

[217] J. Liepert, C. Dettmers, C. Terborg, and C. Weiller. Inhibition of ipsilateral motor cortex during phasic generation of low force. *Clinical Neurophysiology*, 112:114–121, 2001.

[218] M. L. Lipton, C. A. Branch, H. Hrabe, D. P. Lewis, and J. A. Helpern. Differences in spatial extent of activation: BOLD vs. CBF (FAIR). In *Proceedings of the Eighth Annual Meeting of the ISMRM*, page 981, 2000.

[219] EH Lo, J Rogowska, KF Batchelder, and GL Wolf. Hemodynamical alterations in focal cerebral ischemia: temporal correlation analysis for functional imaging. *Neurol Res*, 18:150–156, 1996.

[220] N.K. Logothetis, H. Merkle, M. Augath, T. Trinath, and K. Ugurbil. Ultra high-resolution fMRI in monkeys with implanted RF coils. *Neuron*, 35:227–242, 2002.

[221] N.K. Logothetis, J. Pauls, M. Augath, T. Trinath, and A. Oeltermann. Neurophysiological investigation of the basis of the fMRI signal. *Nature*, 412:150–157, 2001.

[222] H. Lu, X. Golay, J.J. Pekar, and P.C.M. van Zijl. Functional magnetic resonance imaging based on changes in vascular space occupancy. *Magn. Reson. Med.*, 50:263–274, 2003.

[223] H. Lu, X. Golay, and P.C.M. van Zijl. What is the longitudinal relaxation time (T_1) of blood at 3.0T. In *Proceedings of the Eleventh Annual Meeting of the ISMRM*, page 669, 2003.

[224] W.-M. Luh, E. C. Wong, P. A. Bandettini, B. D. Ward, and J. S. Hyde. Comparison of simultaneously measured perfusion and BOLD signal increases during brain activation with T1-based tissue identification. *Magn. Reson. Med.*, 44:137–143, 2000.

[225] Z. Luz and S. Meiboom. Nuclear magnetic resonance study of the protolysis of trimethylammonium ion in aqueous solution - order of the reaction with respect to the solvent. *Journal of Chemical Physics*, 39(2):366–370, 1963.

[226] K Machida, M Ootsu, and H Nakano. Investigation of cerebral blood volume measurement. *Nippon Hoshasen Gijutsu Gakkai Zasshi*, 59(12):1542–7, 2003.

[227] P.L. Madsen, N.F. Cruz, L. Sokoloff, and G.A. Dienel. Cerebral oxygen/glucose ratio is low during sensory stimulation and rises above normal during recovery: excess glucose consumption during stimulation is not accounted for by lactate efflux from or accumulation in brain tissue. *Journal of Cerebral Blood Flow and Metabolism*, 19:393–400, 1999.

[228] M Maeda, WT Yuh, T Ueda, JE Maley, DL Crosby, MW Zhu, and VA Magnotta. Severe occlusive carotid artery disease: hemodynamic assessment by MR perfusion imaging in symptomatic patients. *AJNR Am J Neuroradiol.*, 20(1):43–51, 1999.

[229] P.J. Magistretti. Coupling synaptic activity to glucose metabolism. In R.S.J. Frackowiak, P.J. Magistretti, R.G. Sholman, J.S. Altman, and M. Adams, editors, *Neuroenergetics: relevance for functional brain imaging*, pages 133–143. HFSP, Strasbourg, 2001.

[230] P.J. Magistretti and L. Pellerin. Cellular bases of brain energy metabolism and their relevance to functional brain imaging: evidence for a prominent role of astrocytes. *Cerebral Cortex*, 6(1):50–61, 1996.

[231] P.J. Magistretti, L. Pellerin, D.L. Rothman, and R.G. Shulman. Energy on demand. *Science*, 5401:496–7, 1999.

[232] D. Malonek and A. Grinvald. Interactions between electrical activity and cortical microcirculation revealed by imaging spectroscopy: implications for functional brain mapping. *Science*, 272:551–554, 1996.

[233] J. B. Mandeville, J. J. Marota, C. Ayata, G. Zaharchuk, M. A. Moskowitz, B. R. Rosen, and R. M. Weisskoff. Evidence of a cerebrovascular postarteriole windkessel with delayed compliance. *Journal of Cerebral Blood Flow Metabolism*, 19:679–689, 1999.

[234] J.B. Mandeville and J. J. A. Marota. Vascular filters of functional MRI: Spatial localization using BOLD and CBV contrast. *Magn. Reson. Med.*, 42:591–598, 1999.

[235] J.B. Mandeville, J.J.A. Marota, B.E. Kosofsky, J.R. Keltner, R. Weissleder, B.R. Rosen, and R.M. Weisskoff. Dynamic functional imaging of relative cerebral blood volume during rat forepaw stimulation. *Magn. Reson. Med.*, 39:615–624, 1998.

[236] G Marchal, K Benali, S Iglesias, F Viader, JM Derlon, and JC Baron. Voxel-based mapping of irreversible ischaemic damage with PET in acute stroke. *Brain*, 122(12):2387–400, 1999.

[237] S. Marrett and A. Gjedde. Changes of blood flow and oxygen consumption in visual cortex of living humans. *Adv. Exp. Med. Biol.*, 413:205–208, 1997.

[238] E Martin, P Joeri, T Loenneker, D Ekatodramis, D Vitacco, J Hennig, and VL Marcar. Visual processing in infants and children studied using functional MRI. *Pediatr Res.*, 46(2):135–40, 1999.

[239] WR Martin, RP Baker, RL Grubb, and ME Raichle. Cerebral blood volume, blood flow, and oxygen metabolism in cerebral ischaemia and subarachnoid haemorrhage: an in-vivo study using positron emission tomography. *Acta Neurochir (Wien)*, 70(1-2):3–9, 1984.

[240] K. Matsunami and I. Hamada. Effects of stimulation of corpus callosum on precentral neuron activity in the awake monkey. *Journal of Neurophysiology*, 52(4):676–691, 1984.

[241] N.A. Matwiyoff, C. Gasparovic, R. Mazurchuk, and G. Matwiyoff. The line shapes of the water proton resonances of red blood cells containing carbonyl hemoglobin, deoxyhemoglobin, and methemoglobin: implications for the interpretation of proton MRI at fields of 1.5 T and below. *Magn. Reson. Imaging*, 8:295–301, 1990.

[242] N.A. Matwiyoff, C. Gasparovic, R. Mazurchuk, and G. Matwiyoff. On the origin of paramagnetic inhomogeneity effects in whole blood. *Magn. Reson. Med.*, 20:144–150, 1991.

[243] TE Mayer, GF Hamann, J Baranczyk, B Rosengarten, E Klotz, M Wiesmann, U Missler, Schulte-G Altedorneburg, and HJ Brueckmann. Dynamic CT perfusion imaging of acute stroke. *AJNR Am J Neuroradiol.*, 21(8):1441–9, 2000.

[244] B. Mazoyer. Combining functional MRI with neurochemical mapping obtained with PET and SPECT. In C.T.W. Moonen and P.A. Bandettini, editors, *Functional MRI*, chapter 38, pages 465–471. Springer-Verlag, Berlin, 1999.

[245] DJ Mehagnoul-Schipper, BF van der Kallen, WN Colier, MC van der Sluijs, LJ van Erning, HO Thijssen, B Oeseburg, WH Hoefnagels, and RW Jansen. Simultaneous measurements of cerebral oxygenation changes during brain activation by near-infrared spectroscopy and functional magnetic resonance imaging in healthy young and elderly subjects. *Hum Brain Mapp.*, 16(1):14–23, 2002.

[246] B. U. Meyer, S. Roericht, H. Graefin von Einsiedel, f. Kruggel, and A. Weindl. Inhibitory and excitatory interhemispheric transfers between motor cortical areas in normal humans and patients with abnormalities of the corpus callosum. *Brain*, 118:429–440, 1995.

[247] M.W. Meyer and A.C. Klassen. Regional brain blood flow during sympathetic s-timulation. In T.W. Langfitt, L.C. McHenry, M. Reivich, and H. Wollman, editors, *Cerebral circulation and metabolism*, page 459. Springer-Verlag, New York, 1975.

[248] C. T. Moonen, F. A. Barrios, J. R. Zigun, J. Gillen, G. Liu, G. Sobering, R. Sexton, J. Woo, J. Frank, and D. R. Weinberger. Functional brain MR imaging based on bolus tracking with a fast T2*-sensitized gradient-echo method. *Magn. Reson. Imaging*, 12(3):379–85, 1994.

[249] JP Muizelaar, PP Fatouros, and ML Schroder. A new method for quantitative regional cerebral blood volume measurements using computed tomography. *Stroke*, 28(10):1998–2005, 1997.

[250] T.A. Mulderink, D.R. Gitelman, M.M. Mesulam, and T.B. Parrish. On the use of caffeine as a contrast booster for BOLD fMRI studies. *Neuroimage*, 15(1):37–44, 2002.

[251] S Muramoto, H Yamada, N Sadato, H Kimura, Y Konishi, K Kimura, M Tanaka, T Kochiyama, Y Yonekura, and H. Ito. Age-dependent change in metabolic response to photic stimulation of the primary visual cortex in infants: functional magnetic resonance imaging study. *J Comput Assist Tomogr.*, 26(6):894–901, 2002.

[252] DG Nabavi, A Cenic, RA Craen, AW Gelb, JD Bennett, R Kozak, and TY Lee. CT assessment of cerebral perfusion: experimental validation and initial clinical experience. *Radiology*, 213(1):141–9, 1999.

[253] K. Nagata and T. Asano. Functional image of dynamic computed tomography for the evaluation of cerebral hemodynamics. *Stroke*, 21:882–889, 1990.

[254] K Nagata, Y Kondoh, R Atchison, M Sato, Y Satoh, Y Watahiki, Y Hirata, and E Yokoyama. Vascular and metabolic reserve in Alzheimer's disease. *Neurobiol Aging*, 21(2):301–7, 2000.

[255] J. Netz, U. Ziemann, and V. Hoemberg. Hemispheric asymmetry of transcallosalinhibition in man. *Experimental Brain Research*, 104:527–533, 1995.

[256] G.C. Newman, E.D. Deranja, A. Tudorica, F.E. Hospod, and C.S. Patlak. Cerebral blood volume measurements by T_2^* weighted MRI and contrast infusion. *Magn. Reson. Med.*, 50:844–855, 2003.

[257] A. C. Nirkko, C. Ozdoba, S. M. Redmond, M. Buerki, G. Schroth, C. W. Hess, and M. Wiesendanger. Different ipsilateral representations for distal and proximal movements in the sensorimotor cortex: activation and deactivation patterns. *Neuroimage*, 13:825–835, 2001.

[258] D.G. Nishimura, A. Macovski, and J.M. Pauly. Considerations of magnetic resonance angiography by selective inversion recovery. *Magn. Reson. Med.*, 7:472–484, 1988.

[259] D Norman, L Axel, and WH Berninger et al. Dynamic computed tomography of the brain: techniques, data analysis, and applications. *AJNR*, 2:1–12, 1991.

[260] H. Obrig, M. Neufang, R. Wenzel, M. Kohl, J. Steinbrink, K. Einhaupl, and A. Villringer. Spontaneous low frequency oscillations of cerebral hemodynamics and metabolism in human adults. *Neuroimage*, 12(6):623–39, 2000.

[261] S. Ogawa, T. M. Lee, A. R. Kay, and D. W. Tank. Brain magnetic resonance imaging with contrast dependent on blood oxygenation. *Proceedings of the National Academy of Sciences of the United States of America*, 87(24):9868–72, Dec 1990.

[262] S. Ogawa, D. W. Tank, R. Menon, J. M. Ellermann, S. G. Kim, H. Merkle, and K. Ugurbil. Intrinsic signal changes accompanying sensory stimulation: functional brain mapping with magnetic resonance imaging. *Proceedings of the National Academy of Sciences of the United States of America*, 89(13):5951–5, Jul 1 1992.

[263] H Okazawa, H Yamauchi, K Sugimoto, M Takahashi, H Toyoda, Y Kishibe, and H Shio. Quantitative comparison of the bolus and steady-state methods for measurement of cerebral perfusion and oxygen metabolism: positron emission tomography study using ^{15}o-gas and water. *J Cereb Blood Flow Metab*, 21(7):793–803, 2001.

[264] H. Okazawa, H. Yamauchi, K. Sugimoto, H. Toyoda, Y. Kishibe, and M. Takahashi. Effects of acetazolamide on cerebral blood flow, blood volume, and oxygen metabolism: a positron emission tomography study with healthy volunteers. *Journal of Cerebral Blood Flow and Metabolism*, 21:1472–1479, 2001.

[265] W.H. Oldendorf. Brain uptake of radiolabeled amino acids, amines, and hexoses after arterial injection. *American Journal of Physiology*, 221:1629–39, 1971.

[266] R. C. Oldfield. The assessment and analysis of handedness: the Edinburgh inventory. *Neuropsychologia*, 9:97–113, 1971.

[267] R. J. Ordidge, M. Wylezinska, J. W. Hugg, E. Butterworth, and F. Franconi. Frequency offset corrected inversion (FOCI) pulses for use in localized spectroscopy. *Magn. Reson. Med.*, 36(4):562–6, 1996.

[268] K. Packer. The effects of diffusion through locally inhomogeneous magnetic fields on transverse nuclear spin relaxation in heterogeneous systems. proton transverse relaxation in striated muscle tissue. *Journal of Magnetic Resonance*, 9:438–443, 1973.

[269] FS Pardo, HJ Aronen, D Kennedy, G Moulton, K Paiva, P Okunieff, EV Schmidt, FH Hochberg, GR Harsh, and AJ Fischman et al. Functional cerebral imaging in the evaluation and radiotherapeutic treatment planning of patients with malignant glioma. *Int J Radiat Oncol Biol Phys.*, 30(3):663–9, 1994.

[270] L. Pauling and C. D. Coryell. The magnetic properties and structure of hemoglobin, oxyhemoglobin, and carbonmonoxyhemoglobin. *Proceedings of the National Academy of Sciences of the United States of America*, 22:210–216, 1936.

[271] O. Paulson and E.A. Newman. Does the relase of potassium from astrocyte endfeet regulate cerebral blood flow? *Science*, 237:896–898, 1987.

[272] O.B. Paulson and F.W. Sharbrough. Physiologic and pathophysiologic relationship between the electroencephalogram and the regional cerebral blood flow. *Acta Neurologica Scandinavica*, 50(2):194–220, 1974.

[273] G. Pawlik, A. Rackl, and R. J. Bing. Quantitative capillary topography and blood flow in the cerebral cortex of cats: an in vivo microscopic study. *Brain Research*, 208:35–58, 1981.

[274] J.A Pears, S.T. Francis, S.E. Butterworth, R.W. Bowtell, and P.A. Gowland. Investigating the BOLD effect during infusion of Gd DTPA using rapid T_2^* imaging. *Magn. Reson. Med.*, 49:61–70, 2003.

[275] L. Pellerin and P.J. Magistretti. Food for thought: challenging the dogmas. *Journal of Cerebral Blood Flow and Metabolism*, 23(11):1282–6, 2003.

[276] L. Pellerin and P.J. Magistretti. Neuroenergetics: calling upon astrocytes to satisfy hungry neurons. *Neuroscientist*, 10(1):53–62, 2004.

[277] JS Perlmutter, WJ Powers, P Herscovitch, PT Fox, and ME Raichle. Regional asymmetries of cerebral blood flow, blood volume, and oxygen utilization and extraction in normal subjects. *J Cereb Blood Flow Metab.*, 7(1):64–7, 1987.

[278] M.E. Phelps and J.C. Mazziotta. Positron emission tomography: human brain function and biochemistry. *Science*, 228:799–809, 1985.

[279] R Pineiro, S Pendlebury, H Johansen-Berg, and PM Matthews. Altered hemodynamic responses in patients after subcortical stroke measured by functional MRI. *Stroke*, 33(1):103–9, 2002.

[280] F Placidi, R Floris, A Bozzao, A Romigi, M Tombini, ME Baviera, F Sperli, F Izzi, D Mattia, and MG Marciani. Dynamic susceptibility contrast (DSC) MRI and interictal epileptiform activity in cryptogenic partial epilepsy. *Epilepsia*, 43(12):1515–21, 2002.

[281] Ter-MM Pogossian and P Herscovitch. Radioactive oxygen-15 in the study of cerebral blood flow, blood volume, and oxygen metabolism. *Semin Nucl Med.*, 15(4):377–94, 1985.

[282] C. S. Poon and R. M. Henkelman. Practical T_2 quantitation for clinical applications. *J. Magn. Reson. Imaging*, 2(5):541–53, Sep-Oct 1992.

[283] WJ Powers, IB Hirsch, and PE Cryer. Effect of stepped hypoglycemia on regional cerebral blood flow response to physiological brain activation. *American Journal of Physiology*, 270(2):H554–9, 1996.

[284] W. H. Press, S. A. Teukolsky, W. T. Vetterling, and B. P. Flannery. *Numerical Recipes in C: The art of scientific computing*, chapter 15, pages 666–670. Cambridge University Press, New York, 2nd edition, 1992.

[285] J. Prichard, D. Rothman, and E. Novotny. Lactate rise detected by ^{1}H NMR in human visual cortex during physiologic stimulation. *Proc. Natl. Acad. Sci. USA*, 88:5829–5831, 1991.

[286] A.R. Pries, K. Lee, and P. Gaehtgens. Generalization of the fahraeus principle for microvessel networks. *Am. J. Physiol.*, 251:H1324–H1332, 1986.

[287] M.J. Purves. *The physiology of the cerebral circulation.* Cambridge University Press, New York, 1972.

[288] H. Qian and J.B. Bassingthwaighte. A class of flow bifurcation models with lognormal distribution and fractal dispersion. *Journal of theoretical biology*, 205(2):261–8, 2000.

[289] M. Rausch, K. Scheffler, M. Rudin, and E. W. Radu. Analysis of input functions from different arterial branches with gamma variate functions and cluster analysis for quantitative blood volume measurements. *Magn. Reson. Imaging*, 18(10):1235–1243, 2000.

[290] W Richter and M Richter. The shape of the fMRI BOLD response in children and adults changes systematically with age. *Neuroimage*, 20(2):1122–31, 2003.

[291] A Riecker, W Grodd, U Klose, JB Schulz, K Groschel, M Erb, H Ackermann, and A Kastrup. Relation between regional functional MRI activation and vascular reactivity to carbon dioxide during normal aging. *J Cereb Blood Flow Metab.*, 23(5):565–73, 2003.

[292] F. Robert, 2004. www.univ-orleans.fr/ SCIENCES/ neurobiologie/ images_recherche.htm.

[293] P. Robinson and S.I. Rapoport. Glucose transport and metabolism in the brain. *American Journal of Physiology*, 250:R127–36, 1986.

[294] P.E. Roland. *Brain Activation*. Wiley-Liss, New York, NY, 1993.

[295] P.E. Roland, L. Eriksson, S. Stone-Elander, and L. Widen. Does mental activity change the oxidative metabolism of the brain? *Journal of Neuroscience*, 7(8):2373–2389, 1987.

[296] P.E. Roland, L. Eriksson, L. Widen, and S. Stone-Elander. Changes in regional cerebral oxidative matabolism induced by tactile learning and recognition in man. *European Journal of Neuroscience*, 1:3–18, 1989.

[297] B. R. Rosen, J. W. Belliveau, Buchbinder B. R., R. C. McKinstry, L. M. Porkka, D. N. Kennedy, M. S. Neuder, C. R. Fisel, H. J. Aronen, K. K. Kwong, R. M. Weisskoff, M. S. Cohen, and T. J. Brady. Contrast agents and cerebral hemodynamics. *Magn. Reson. Med.*, 19:285–292, 1991.

[298] B. R. Rosen, J. W. Belliveau, J. M. Vevea, and T. J. Brady. Perfusion imaging with NMR contrast agents. *Magn. Reson. Med.*, 14(2):249–65, May 1990.

[299] BR Rosen, JW Belliveau, HJ Aronen, D Kennedy, BR Buchbinder, A Fischman, M Gruber, J Glas, RM Weisskoff, and MS Cohen et al. Susceptibility contrast imaging of cerebral blood volume: human experience. *Magn Reson Med.*, 22(2):293–9, 1991.

[300] R. M. Rossini, F. Zarola, E. Stalberg, and M. Caramina. Pre-movement facilitation of motor evoked potentials in man during transcranial stimulation of the central motor pathways. *Brain Research*, 458:20–30, 1988.

[301] E Rostrup, I Law, F Pott, K Ide, and GM Knudsen. Cerebral hemodynamics measured with simultaneous PET and near-infrared spectroscopy in humans. *Brain Res.*, 954(2):183–93, 2002.

[302] C.S. Roy and C.S. Sherrington. On the regulation of the blood supply of the brain. *J Physiol*, 11:85–105, 1890.

[303] R. Rubio, R.M. Berne, E.L. Bockman, and R.R. Curnish. Relationship between adenosine concentration and oxygen supply in rat brain. *American Journal of Physiology*, 228(6):1896–1902, 1975.

[304] U Sabatini, P Celsis, G Viallard, A Rascol, and JP Marc-Vergnes. Quantitative assessment of cerebral blood volume by single-photon emission computed tomography. *Stroke*, 22(3):324–30, 1991.

[305] F Sakai, K Nakazawa, Y Tazaki, K Ishii, H Hino, H Igarashi, and T Kanda. Regional cerebral blood volume and hematocrit measured in normal human volunteers by single-photon emission computed tomography. *J Cereb Blood Flow Metab*, 5(2):207–13, 1985.

[306] J. A. Sanders and W. W. Orrison. Functional magnetic resonance imaging. In W. W. Orrison, J. D. Lewine, J. A. Sanders, and M. F. Hartshorne, editors, *Functional Brain Imaging*, pages 239–326. Mosby-Year Book, Inc.: St. Louis, MO, 1995.

[307] D Sappey-Marinier, G Calabrese, G Fein, JW Hugg, C Biggins, and MW Weiner. Effect of photic stimulation on human visual cortex lactate and phosphates using 1h and 31p magnetic resonance spectroscopy. *J Cereb Blood Flow Metab.*, 12(4):584–92, 1992.

[308] K Scheffler, E Seifritz, R Haselhorst, and D Bilecen. Titration of the BOLD effect: Separation and quantitation of blood volume and oxygenation changes in the human cerebral cortex during neuronal activation and ferumoxide infusion. *Magn. Reson. Med.*, 42:829–836, 1999.

[309] P Schumann, O Touzani, AR Young, R Morello, JC Baron, and ET MacKenzie. Evaluation of the ratio of cerebral blood flow to cerebral blood volume as an index of local cerebral perfusion pressure. *Brain*, 121(7):1369–1379, 1998.

[310] W.J. Schwartz, C.B. Smith, L. Davidsen, H. Savaki, L. Sokoloff, M. Mata, D.J. Fink, and H. Gainer. Metabolic mapping of functional activity in the hypothalamo-neurohypophysial system of the rat. *Science*, 205:723–5, 1979.

[311] E. Seifritz, D. Bilecen, D. Haenggi, R. Haselhorst, E.W. Radue, S. Wetzel, J. Seelig, and K. Scheffler. Effect of ethanol on BOLD response to acoustic stimulation: implications for neuropharmacological fMRI. *Psychiatry Research*, 99:1–13, 2000.

[312] R.J. Seitz and P.E. Roland. Vibratory stimulation increases and decreases the regional cerebral blood flow and oxidative metabolism: a positron emission tomography (PET) study. *Acta neurologica Scandinavica*, 86:60–7, 1992.

[313] M Shimoda, S Oda, M Yamamoto, F Kawamata, and O Sato. Functional imaging of cerebral blood volume using simultaneous measurements of dynamic and xenon computerized tomography (ct). *Tokai J Exp Clin Med.*, 16(1):77–81, 1991.

[314] L. Shinn-Zong, C. Tsorng-Lanng, C. Yung-Hsiao, and S. Wen-Shen. Hemodilution accelerates the passage of plasma (not red cells) through cerebral microvessels in rats. *Stroke*, 26:2166–2171, 1995.

[315] A. Shmuel, M. Augath, a. Oeltermann, J. Pauls, Y. Murayama, and N. K. Logothetis. The negative BOLD response in monkey V1 is associated with decreases in neuronal activity. *Neuroimage Supplement 1*, 19(2):S308, 2003.

[316] A. Shmuel, M. Augath, E. Rounis, N. K. Logothetis, and S. Smirnakis. Negative BOLD response ipsi-lateral to the visual stimulation: origin is not blood stealing. *Neuroimage Supplement 1*, 19(2):S309, 2003.

[317] A. Shmuel, E. Yacoub, J. Pfeuffer, P.-F. Van de Moortele, G. Adriany, X. Hu, and K. Ugurbil. Sustained negative BOLD, blood flow and oxygen consumption response and its coupling to the positive response in the human brain. *Neuron*, 36:1195–1210, 2002.

[318] N. Sibson. Energy metabolism in neural tissues in vivo at rest and in functionally altered states. In R.G. Shulman and D.L. Rothman, editors, *Cerebral energetics and neurotransmitter fluxes*, pages 75–98. John Wiley & Sons Ltd., West Sussex,England, 2004.

[319] N.R. Sibson, A. Dhankhar, G.F. Mason, D.L. Rothman, K.L. Behar, and R.G. Shulman. Stoichiometric coupling of brain glucose metabolism and glutamatergic neuronal activity. *Proc. Natl. Acad. Sci. USA.*, 95(1):316–21, 1998.

[320] N.R. Sibson, J. Shen, G.F. Mason, D.L. Rothman, K.L. Behar, and R.G. Shulman. Functional energy metabolism: in vivo ^{13}C-NMR spectroscopy evidence for coupling of cerebral glucose consumption and glutamatergic neuronalactivity. *Developmental Neuroscience*, 20(4-5):321–30, 1998.

[321] K.M. Sicard, Q. Shen, Z.M. Liu, and T.Q. Duong. Forepaw-stimulation CBF and BOLD response under hypoxia, hyperoxia and hypercapnia. In *Proceedings of the Twelfth Annual Meeting of the ISMRM*, page 274, Kyoto, 2004.

[322] B. Siesjo. *Brain Energy Metabolism.* Wiley, New York, 1978.

[323] M.J. Silvennoinen, C.S. Clingman, X. Golay, R.A. Kauppinen, and P.C.M. van Zijl. Comparison of the dependence of blood R_2 and R_2^* on oxygen saturation at 1.5 and 4.7 Tesla. *Magn. Reson. Med.*, 49:47–60, 2003.

[324] M.J. Silvennoinen, M.I. Kettunen, and R.A. Kauppinen. Effect of hematocrit and oxygen saturation level on blood spin-lattice relaxation. *Magn. Reson. Med.*, 49:568–571, 2003.

[325] D.U. Silverthorn. *Human Physiology An Integrated Approach.* Prentice Hall, New Jersey, 1998.

[326] A.J. Smith, H. Blumenfeld, K.L. Behar, D.L. Rothman, R.G. Shulman, and F. Hyder. High-resolution CMR_{O_2} mapping in rat cortex: A multiparametric approach to calibration of BOLD image contrast at 7 Tesla. *Journal of Cerebral Blood Flow and Metabolism*, 20(5):847–860, 2000.

[327] A.J. Smith, H. Blumenfeld, K.L. Behar, D.L. Rothman, R.G. Shulman, and F. Hyder. Cerebral energetics and spiking frequency: the neurophysiological basis of fMRI. *Proc. Natl. Acad. Sci. USA.*, 99:10237–9, 2002.

[328] AT Smith, AL Williams, and KD Singh. Negative BOLD in the visual cortex: evidence against blood stealing. *Hum Brain Mapp.*, 21(4):213–20, 2004.

[329] J.J. Smith. *Circulatory physiology: the essentals.* Baltimore: Williams & Wilkins, 1990.

[330] L. Sokoloff. The relation between function and energy metabolism: its use in the localization of functional activity in the nervous system. *Neurosciences Research Progress bulletin*, 19:159–210, 1981.

[331] L. Sokoloff. Energetics of functional activation in neural tissues. In R.S.J. Frackowiak, P.J. Magistretti, R.G. Shulman, J.S. Altman, and M. Adams, editors, *Neuroenergetics: relevance for functional brain imaging*, pages 45–54. HFSP, Strasbourg, 2001.

[332] L. Sokoloff. Energy metabolism in neural tissues in vivo at rest and in functionally altered states. In R.G. Shulman and D.L. Rothman, editors, *Brain energetics & neuronal activity applications to fMRI and medicine*, pages 11–30. John Wiley & Sons Ltd., West Sussex,England, 2004.

[333] L. Sokoloff, M. Reivich, C. Kennedy, M.H. Des Rosiers, C.S. Patlak, K.D. Pettigrew, O. Sakurada, and M. Shinohara. The [^{14}C]deoxyglucose method for the measurement of local cerebral glucose utilization: theory, procedure, and normal values in the conscious and anesthetized albino rat. *Journal of Neurochemistry*, 28(5):897–916, 1977.

[334] AG Sorensen, WA Copen, L Ostergaard, FS Buonanno, RG Gonzalez, G Rordorf, BR Rosen, LH Schwamm, RM Weisskoff, and WJ Koroshetz. Hyperacute stroke: simultaneous measurement of relative cerebral blood volume, relative cerebral blood flow, and mean tissue transit time. *Radiology*, 210(2):519–27, 1999.

[335] W. M. Spees, D. A. Yablonskiy, M. C. Oswood, and J. J. H. Ackerman. Water proton MR properties of human blood at 1.5 T: magnetic susceptibility, T_1, T_2, T_2^* and non-Lorentzian signal behaviour. *Magn. Reson. Med.*, 45:533–542, 2001.

[336] C.S. Springer. The molecular sources of the BOLD-based fMRI response. In *Syllabus of the Educational Courses of the Eleventh Annual Meeting of the ISMRM*, pages 263–268, Toronto, ON, 2003.

[337] K.S. St. Lawrence, F.Q. Ye, B.K. Lewis, J.A. Frank, and A.C. McLaughlin. Measuring the effects of indomethacin on changes in cerebral oxidative metabolism and cerebral blood flow during sensorimotor activation. *Magn. Reson. Med.*, 50:99–106, 2003.

[338] H. Stadelmann, E. Mueller, and K. Geibel. Relaxationszeiten von venoesem Blut in Abhaengigkeit von der Feldstaerke. *Electromedica*, 59:82–88, 1991.

[339] B. Stefanovic and G. B. Pike. Quantitative dynamic measurement of cerebral blood volume changes via fMRI. In *Proceedings of the Tenth Annual Meeting of the ISMRM*, page 119, Honolulu, 2002.

[340] B Stefanovic and GB Pike. Human whole-blood relaxometry at 1.5t: Asessment of diffusion and exchange models. *Magn. Reson. Med.*, 52(4):716–723, 2004.

[341] B Stefanovic, JG Sled, and GB Pike. Quantitative T_2 in the occipital lobe: the role of the CPMG refocusing rate. *J. Magn. Reson. Imaging*, 18(3):302–309, 2003.

[342] B. Stefanovic, J. M. Warnking, and G. B. Pike. Simultaneous fMRI-based measurements of cerebral blood volume, flow and BOLD. *Neuroimage S1*, 19(2):312, 2003.

[343] HJ Steiger, R Aaslid, and R Stooss. Dynamic computed tomography imaging of regional cerebral blood flow and blood volume: a clinical pilot study. *Stroke*, 24:591–597, 1993.

[344] G.N. Stewart. Researches on the circulation time in organs and on the influences which affect it. *J. Physiol. (London)*, 15:Parts I–III, 1894.

[345] G. Strangman, D.A. Boas, and J.P. Sutton. Non-invasive neuroimaging using near-infrared light. *Biol Psychiatry*, 52(7):679–93, 2002.

[346] K. R. Thulborn, J. C. Waterton, P. M. Matthews, and G. K. Radda. Oxygenation dependence of the transverse relaxation time of water protons in whole blood at high field. *Biochim. Biophys. Acta*, 714(2):265–70, Feb 2 1982.

[347] K.R. Thulborn, J.C. Waterton, P.M. Matthews, and G.K. Radda. Oxygenation dependence of the transverse relaxation time of water protons in the whole blood at high field. *Biochim. Biophys. Acta*, 714:265–270, 1982.

[348] R. B. Tootell, N. Hadjikhani, E. K. Hall, S. Marrett, W. Vanduffel, J. T. Vaughan, and A. M. Dale. The retinotopy of visual spatial attention. *Neuron*, 21:1409–1422, 1998.

[349] M. Tsacopoulos and P.J. Magistretti. Metabolic coupling between glia and neurons. *Journal of Neuroscience*, 16(3):877–85, 1996.

[350] R. Turner. How much cortex can a vein drain? Downstream dilution of activation-related cerebral blood oxygenation changes. *Neuroimage*, 16(4):1062–7, 2002.

[351] M.S. Vafaee, S. Marrett, E. Meyer, A.C. Evans, and A. Gjedde. Increased oxygen consumption in human visual cortex: response to visual stimulation. *Acta neurologica Scandinavica*, 98:85–9, 1998.

[352] M.S. Vafaee, E. Meyer, S. Marrett, T. Paus, A.C. Evans, and A. Gjedde. Frequency-dependent changes in cerebral metabolic rate of oxygen during activation of human visual cortex. *Journal of Cerebral Blood Flow and Metabolism*, 19:272–7, 1999.

[353] P. C. M. van Zijl, S. M. Eleef, J. A. Ulatowski, J. M. E. Oja, A. Z. M. Ulug, R. J. Traystman, and R. A. Kauppinen. Quantitative assessment of blood flow, blood volume and blood oxygenation effects in functional magnetic resonance imaging. *Nat. Med.*, 4(2):159–167, 1998.

[354] A. Vander, J. Sherman, and D. Luciano. *Human Physiology The Mechanism of Body Function*. McGraw-Hill, Boston, MA, 1998.

[355] F Vetterlein, B Demmerle, A Bardosi, U Gobel, and G Schmidt. Determination of capillary perfusion pattern in rat brain by timed plasma labeling. *Am J Physiol.*, 258(1-2):H80–4, 1990.

[356] A Villringer, A Them, U Lindauer, K Einhaupl, and U Dirnagl. Capillary perfusion of the rat brain cortex. an in vivo confocal microscopy study. *Circ. Res.*, 75(1):55–62, 1994.

[357] A Vlasenko, MC Petit-Taboue, G Bouvard, R Morello, and JM Derlon. Comparative quantitation of cerebral blood volume: SPECT versus PET. *J Nucl Med.*, 38(6):919–24, 1997.

[358] S Vorstrup, B Brun, and NA Lassen. Evaluation of the cerebral vasodilatory capacity by the acetazolamide test before EC-IC bypass surgery in patients with occlusion of the internal carotid artery. *Stroke*, 17(6):1291–8, 1986.

[359] J. Vymazal, R. A. Brooks, C. Baumgarner, V. Tran, D. Katz, J. W. M. Bulte, E. R. Rivka Bauminger, and G. Di Chiro. The relation between brain iron and NMR relaxation times: an in vitro study. *Magn. Reson. Med.*, 35:56–61, 1996.

[360] M. Wahl and W. Kuschinsky. The dilatatory action of adenosine on pial arteries of cats and its inhibition by theophylline. *Pflugers Archiv*, 362(1):55–9, 1976.

[361] J. P. Wansapura, S. K. Holland, R. S. Dunn, and W. S. Ball. NMR relaxation times in the human brain at 3.0 Tesla. *J. Magn. Reson. Imaging*, 9(4):531–538, 1999.

[362] E Watanabe, Y Nagahori, and Y Mayanagi. Focus diagnosis of epilepsy using near-infrared spectroscopy. *Epilepsia*, 43(S9):50–5, 2002.

[363] L.D. Watkins. Nitric oxide and cerebral blood flow: An update. *Cerebrovascular and Brain Metabolism Reviews*, 7:324–337, 1995.

[364] A. Wechsler. Blood. In *Physiology 552-201A: Lecture Notes*, pages "23–42", 1999.

[365] R.M. Weisskoff. Basic theoretical models of BOLD signal change. In C.T.W. Moonen and P.A. Bandettini, editors, *Functional MRI*, chapter 11, pages 115–123. Springer-Verlag, Berlin, 1999.

[366] R.M. Weisskoff and S. Kiihne. MRI susceptometry: image-based measurement of absolute susceptibility of MR contrast agents and human blood. *Magn. Reson. Med.*, 24:375–383, 1992.

[367] R. Wenzel, P. Wobst, H. H. Heekeren, K. K. Kwong, S. A. Brandt, M. Kohl, H. O-brig, U. Dirnagl, and A. Villringer. Saccadic suppression induces focal hypooxygenation in the occipital cortex. *Journal of Cerebral Blood Flow and Metabolism*, 20:1103–1110, 2000.

[368] G.B. West, J.H. Brown, and B.J. Enquist. The fourth dimension of life: fractal geometry and allometric scaling of organisms. *Science*, 284(5420):1677–9, 1999.

[369] K. P. Whittall, A. L. MacKay, D. A. Graeb, R. A. Nugent, D. K. B. Li, and D. W. Paty. In vivo measurement of T_2 distributions and water contents in normal human brain. *Magn. Reson. Med.*, 37(1):34–43, Jan 1997.

[370] K. P. Whittall, A. L. MacKay, and D. K. B. Li. Are mono-exponential fits to a few echoes sufficient to determine T_2 relaxation for in vivo human brain. *Magn. Reson. Med.*, 41(1):1255–1257, Jun 1999.

[371] H. R. Winn, A. C. Ngai, and K. R. Ko. Role of adenosine in regulating microvascular CBF in activated sensory cortex. In N. A. Lassen, D. H. Ingvar, M. E. Raichle, and L. Friberg, editors, *Brain work and mental activity: quantitative studies with radioactive tracers*. Munksgsaard: Copenhagen, 1991.

[372] M Wolf, O Weber, M Keel, X Golay, M Scheidegger, HU Bucher, S Kollias, P Boesiger, and O Banziger. Comparison of cerebral blood volume measured by near infrared spectroscopy and contrast enhanced magnetic resonance imaging. *Adv Exp Med Biol*, 471:767–73, 1999.

[373] T. Wolf, U. Lindauer, A. Villringer, and Dirnagl U. Excessive oxygen or glucose supply does not alter the blood flow response to somatosensory stimulation or spreading depression in rats. *Brain Research*, 761(2):290–9, 1997.

[374] E. C. Wong, T. T. Liu, W. M. Luh, L. R. Grank, and R. B. Buxton. T_1 and T_2 selective method for improved SNR in CSF-attenuated imaging: T2-FLAIR. *Magn. Reson. Med.*, 45:529–532, 2001.

[375] E.C. Wong, R.B. Buxton, and L.R. Frank. Implementation of quantitative perfusion imaging techniques for functional brain mapping using pulsed arterial spin labeling. *NMR Biomed.*, 10:237–249, 1997.

[376] K.J. Worsley, C. Liao, J. Aston, V. Petre, G.H. Duncan, F. Morales, and A.C. Evans. A general statistical analysis for fMRI data. *Neuroimage*, 15:1–15, 2002.

[377] Martin WR, Powers WJ, and Raichle ME. Cerebral blood volume measured with inhaled $c^{15}o$ and positron emission tomography. *J Cereb Blood Flow Metab.*, 7(4):421–6, 1987.

[378] G. A. Wright. *Magnetic Resonance Relaxation Behaviour of Blood: Study and Applications*. PhD thesis, Stanford University, 1991.

[379] G. A. Wright, D. G. Nishamura, and A. Macovski. Flow-independent magnetic resonance projection angiography. *Magn. Reson. Med.*, 16:126–140, 1991.

[380] RH Wu, R Bruening, S Noachtar, S Arnold, C Berchtenbreiter, P Bartenstein, A Drzezga, K Tatsch, and M Reiser. MR measurement of regional relative cerebral blood volume in epilepsy. *J Magn Reson Imaging*, 9(3):435–40, 1999.

[381] E. Yacoub, T.Q. Duong, P.F. Van De Moortele, M. Lindquist, G. Adriany, S.G. Kim, K. Ugurbil, and X. Hu. Spin-echo fMRI in humans using high spatial resolutions and high magnetic fields. *Magn. Reson. Med.*, 49(4):655–64, 2003.

[382] F. Q. Ye, W. R. Wayne Martin, and P. S. Allen. Estimation of the iron concentration in excised gray matter by means of proton relaxation measurements. *Magn. Reson. Med.*, 35:285–289, 1996.

[383] T. Yoshiura, S. Higano, A. Rubio, D. A. Shrier, W. E. Kwok, S. Iwanaga, and Y. Numaguchi. Heschl and superior temporal gyri: low signal intensity of the cortex on T_2-weighted MR images of the normal brain. *Radiology*, 214:217–221, 2000.

[384] P Zaramella, F Freato, A Amigoni Salvadori, S, P Marangoni, A Suppjei, B Schiavo, and Chiandetti L. Brain auditory activation measured by near-infrared spectroscopy (nirs) in neonates. *Pediatr Res.*, 49(2):213–9, 2001.

[385] F. Zhao, P. Wang, and S.G. Kim. Cortical depth-dependent gradient-echo and spin-echo BOLD fMRI at 9.4T. *Magn. Reson. Med.*, 51(3):518–24, 2004.

[386] J. Zhou, X. Golay, P. C. M. van Zijl, M. J. Silvennoinen, R. A. Kauppinen, J. J. Pekar, and M. Kraut. Inverse T_2 contrast at 1.5 Tesla between gray matter and white matter in the occipital lobe of normal adult human brain. *Magn. Reson. Med.*, 46:401–406, 2001.

[387] U. Ziemann and M. Hallett. Hemispheric asymmetry of ipsilateral motor cortex activation during unimanual motor tasks: Further evidence for motor dominance. *Clinical Neurophysiology*, 112:107–113, 2001.